PB84-217421

NBS (National Bureau of Standards) Materials Measurements (Annual Report for the Period 1 April 1983-31 March 1984)

(U.S.) National Bureau of Standards
Washington, DC

Prepared for

National Aeronautics and Space Administration
Washington, DC

Jun 84

NBS-114A (REV. 2-8C)

U.S. DEPT. OF COMM. BIBLIOGRAPHIC DATA SHEET (See instructions)	1. PUBLICATION OR REPORT NO. NBSIR 84-2882	2. Performing Organ. Report No. PB84 217421	3. Publication Date June 1984

4. TITLE AND SUBTITLE

NBS: Materials Measurement

5. AUTHOR(S)

J. R. Manning

6. PERFORMING ORGANIZATION (If joint or other than NBS, see instructions)

NATIONAL BUREAU OF STANDARDS
DEPARTMENT OF COMMERCE
WASHINGTON, D.C. 20234

7. Contract/Grant No.
NASA Govt. Order H-27954B

8. Type of Report & Period Covered
Annual Report
Apr. 1, 1983-Mar. 31, 1984

9. SPONSORING ORGANIZATION NAME AND COMPLETE ADDRESS (Street, City, State, ZIP)

Microgravity Science and Applications Program
National Aeronautics and Space Administration
Washington, D.C. 20546

NBS Category No.
NBS-340

10. SUPPLEMENTARY NOTES

☐ Document describes a computer program; SF-185, FIPS Software Summary, is attached.

11. ABSTRACT (A 200-word or less factual summary of most significant information. If document includes a significant bibliography or literature survey, mention it here)

This report describes NBS work for NASA in support of NASA's Microgravity Science and Applications Program under NASA Government Order H-27954B (Properties of Electronic Materials) covering the period April 1, 1983 to March 31, 1984. This work is being carried out in three independent tasks:

Task 1. Surface Tensions and Their Variations with Temperature and Impurities

Task 2. Convection During Unidirectional Solidification

Task 3. Measurement of High Temperature Thermophysical Properties.

The results for each task are given in detail in the body of the report. Tasks 1 and 2 are directed toward determining how the reduced gravity obtained in space flight can affect convection and solidification processes. Emphasis in Task 3 is on development of levitation and containerless processing techniques which can be applied in space flight to provide thermodynamic measurements of reactive materials.

12. KEY WORDS (Six to twelve entries; alphabetical order; capitalize only proper names; and separate key words by semicolons)

binary alloy; convection; directional solidification; silicon; surface tension; thermodynamic properties; tungsten

13. AVAILABILITY

☒ Unlimited
☐ For Official Distribution. Do Not Release to NTIS
☐ Order From Superintendent of Documents, U.S. Government Printing Office, Washington, D.C. 20402.
☒ Order From National Technical Information Service (NTIS), Springfield, VA. 22161

14. NO. OF PRINTED PAGES
155

15. Price
$16.00

USCOMM-DC 6043-P80

NBSIR 84-2882

NBS: MATERIALS MEASUREMENTS

J. R. Manning

U.S. DEPARTMENT OF COMMERCE
National Bureau of Standards
Washington, DC 20234

June 1984

Annual Report
For the Period 1 April 1983 - 31 March 1984
NASA Government Order H-27954B
Properties of Electronic Materials

U.S. DEPARTMENT OF COMMERCE, Malcolm Baldrige, *Secretary*
NATIONAL BUREAU OF STANDARDS, Ernest Ambler, *Director*

1.02

TABLE OF CONTENTS

NATIONAL BUREAU OF STANDARDS
MATERIALS MEASUREMENTS

Summary

This report describes NBS work for NASA in support of NASA's Microgravity Science and Applications Program under NASA Government Order H-27954B (Properties of Electronic Materials) covering the period April 1, 1983 to March 31, 1984. This work is being carried out in three independent tasks:

Task 1. Surface Tensions and Their Variations with Temperature and Impurities

Task 2. Convection During Unidirectional Solidification

Task 3. Measurement of High Temperature Thermodynamic Properties

The results for each task are given separately in the body of the report.

With the advent of the Space Shuttle and the accompanying availability of space flight opportunities, it may become feasible to exploit the unique microgravity environment of space flight to produce improved materials and improved measurements of important materials properties. Reduction of convection and enhanced capabilities for containerless processing are two advantages frequently cited for materials processing in space. Both of these topics are considered in the current work. Tasks 1 and 2 are directed toward determining how the reduced gravity obtained in space flight can affect convection and solidification processes. Emphasis in Task 3 is on development of levitation and containerless processing techniques which can be applied in space flight to provide thermodynamic measurements of reactive materials.

In materials processing on earth, gravity frequently produces density-driven convection, thereby causing liquids to be stirred as they solidify. This stirring disturbs the quiescent boundary layer at the solidifying

interface and can be very undesirable if nearly perfect crystals are required. For example, it creates interface instabilities, introduces segregation of components, and produces crystal defects in the resulting solid material. These defects and inhomogeneities, which are particularly troublesome in electronic technology and other advanced technical applications, might be avoided in materials produced under microgravity conditions. Different aspects of these convection processes are being considered in the first two tasks. Surface tension gradients which may be the main source of convection in space flight experiments are the measurement focus in Task 1; whereas interactions between solidification processes, convection effects, and interface stability, as influenced by gravity and the lack thereof, are under investigation in Task 2.

In Task 1, measurements are being made of the surface tension of liquid silicon. Silicon is one of the most important materials used in electronic technology. Because of the need for a fully defect-free silicon, not readily obtainable under earth-bound conditions where gravity driven convection can be important, silicon is a major candidate material for processing in space. In planning such space processing, it is important to know the dependence of silicon surface tension on temperature and impurities, particularly oxygen. Surface tension gradients produce Marangoni convection and may be the main source of fluid flows which affect solidification processes in space. Despite the technological importance of silicon, the variations of its surface tension with temperatures and impurities were not known prior to initiation of the current work. Since silicon is very reactive, previous measurements had been for the most part non-systematic and unreliable. The current sessile drop experiments have established

that the temperature (T) dependence of the surface tension (γ) is given by $d\gamma/dT = -0.28$ mJ/m^{2}K for liquid silicon in an atmosphere of purified argon in the 200 degree temperature range above the silicon melting point. Experiments are now underway to determine what appears to be an appreciable dependence of γ and $d\gamma/dT$ on oxygen impurities.

In Task 2, convective phenomena which arise during directional solidification are being investigated by both theoretical calculations and experiments. Direct measurements of convection and associated solidification effects are being made during directional solidification of transparent materials, particularly succinonitrile containing small amounts of ethanol; and calculations are being made of convection, interface stability and impurity segregation that should be expected during directional solidification. The experimental observations in ground-based measurements at NBS of unidirectional upwards solidification of succinonitrile containing ethanol have demonstrated that convective flow plays an important role in determining the site at which interfacial stabilities develop. It was also determined that the presence of a vapor bubble at the interface resulted in vigorous convective flow, induced by surface tension gradients. Directional solidification techniques are the leading methods proposed for obtaining more nearly defect-free materials in space. It is important in planning such processing techniques to consider the role convection effects, including previously unexpected effects found in the present work, could play under reduced gravity conditions. The theoretical calculations thus specifically include determinations of the effects a reduction in gravitational force will have on convection, as will be important, for example, in space flight experiments in the MEPHISTO project. Calculations have been made of the

solute, temperature, and flow fields at constant solidification velocity taking into account solute rejection at the solidification interface. This solute rejection can strongly influence convection effects. Linear stability calculations for a flow parallel to a crystal-melt interface also have been performed. These calculations demonstrated a coupling between hydrodynamic and morphological instabilities and are in general agreement with experiments carried out by Glicksman and colleagues.

In Task 3, assistance is being provided to a joint project involving investigators from Rice University (Professor J. Margrave) and General Electric Co. (Dr. R. T. Frost) in which a General Electric electromagnetic levitation device is being used to develop levitation/drop calorimetry techniques having space flight applications. The critical advantage of such containerless processing experiments is the avoidance of specimen contamination that would occur upon contact of a reactive material with container walls during heating and melting. Measurements of the specific heat of tungsten in earth-bound experiments have yielded some promising results and also have allowed evaluation of certain limitations imposed by gravity in such measurements. A number of automated techniques being developed in this work should also be useful for space flight experiments.

Task 1
Surface Tensions and Their Variations with Temperature and Impurities

S. C. Hardy
Metallurgy Division
Center for Materials Science

and

J. Fine
Surface Science Division
Center for Chemical Physics

SUMMARY

The surface tension of liquid silicon has been measured as a function of temperature in purified argon atmospheres using the sessile drop technique. The measurements show the surface tension is sensitive to low levels of an impurity which is probably oxygen. The highest surface tension values obtained under conditions which minimized the oxygen levels in the apparatus are in good agreement with an isolated previous measurement in pure hydrogen. The surface tension decreases linearly with increasing temperature and has a temperature coefficient of -0.28 mJ/m^2K.

Introduction

The surface tension of silicon and its variation with temperature are not known accurately. These data are of interest because it is now thought that surface tension driving forces contribute significantly to fluid flow in the Czochralski and float zone crystal growth of silicon. Fluid flows arising from surface tensions are referred to as Marangoni or thermocapillary flows. They are important in normal gravity and are the dominant type of fluid flow in low gravity space experiments with silicon for which buoyancy convection is negligibly small. Experiments involving free liquid silicon surfaces are presently being developed for future space shuttle flights. These surface tension measurements are essential for proper experimental design and eventual quantitative interpretation of the low gravity observations.

The driving force for Marangoni flow is the surface tension gradient rather than the surface tension itself. Thus the flow depends sensitively on the value of the surface tension temperature coefficient $K = d\gamma/$ For silicon estimates of K range from approximately -0.1 mJ/m^2K to -0.4 mJ/m^2K. Recent modelling of the Czochralski process for silicon found that this variation in K gave significantly different flow patterns[1]. Thus a quantitative understanding of silicon processing is to some extent dependent on accurate measurements of the temperature variation of the surface tension.

Although its high melting point, vapor pressure and reactivity complicate the experiments, the uncertainty in K for silicon may be attributed largely to the lack of systematic measurements of surface tension over a temperature range. In general it is not possible to calculate K accurately from isolated measurements of surface tension by different techniques or even by the same technique in different laboratories. The small systematic errors in the

measurements are usually large enough to obscure the variation of surface tension due to temperature. The only previous measurement of the silicon surface tension over a temperature range is that of Lukin et al[2]. They found K to be near -0.1 mJ/m^2K. Although this is a reasonable value, the density variation with temperature used in their work is significantly different from the generally accepted dependence. Their results are discussed in more detail below.

Experimental

The surface tensions in this work were determined using the sessile drop technique. This method is based on a comparison of the profile of a liquid drop with the profile calculated by solving the Young-Laplace equation. The comparison can be made in several ways; the traditional Bashforth-Adams[3] procedure has been used here in conjunction with recently calculated drop shape tables which virtually eliminate interpolation errors.

The high temperatures required to melt silicon are generated in an inductively heated furnace. The silicon is contained in a shallow cup which stabilizes the drop and imposes a circular cross section on the drop base. The outside diameter of the cup provides the length standard required in the data analysis. The cup and drop are at the center of a cylindrical susceptor which lies along the axis of a quartz tube. This tube connects through an O-ring coupling to a vacuum system consisting of a water cooled baffle and diffusion pump, trap, forepump, gauges, and valves for admitting gases. Quartz windows at either end of the tube allow simultaneous photography and temperature measurement of the drop with an automatic optical pyrometer. After window corrections, the temperature read by the optical pyrometer on slowly melting the sample was within a few degrees of the silicon melting point.

The susceptor is constructed of three concentric cylinders of molybdenum with an inner cylinder of tantalum. The tantalum liner has a much lower vapor pressure than molybdenum and has been inserted to reduce the evaporation of metal onto the sample during preliminary vacuum degassing. Several layers of zirconia insulation surround but do not touch the susceptor. There is no indication of any decomposition of the insulation at the temperatures used in this work when the insulation does not touch the susceptor.

The induction heater has a power rating of 2.5 kW and operates at 450 kHz. The skin depth at this frequency is about 0.06 cm and calculation indicates that about 10% of the field penetrates the four layer susceptor. However, no difference was found in measured surface tension values when the four layer susceptor was reduced to three layers. This suggests that field penetration is not affecting the measurements significantly.

The choice of a cup material is critical because of the high reactivity of liquid silicon and the sensitivity of the surface tension to even low bulk concentrations of surface active impurities. Studies of the compatibility of liquid silicon with various substances indicated that boron nitride was a suitable container because of its insolubility in liquid silicon[4]. Although the silicon may acquire some free boron when in contact with boron nitride, this should not introduce serious errors in surface tension measurements because boron has a higher surface tension than silicon and does not surface segregate. The development of a bulk boron concentration in the silicon can measurably increase the surface tension, but only at high concentrations[2]. We have found no change in surface tension with prolonged high temperature contact with the BN cups. We conclude, therefore, that boron contamination is not appreciably affecting these measurements. The

solid silicon does not bond to the cups, possibly because of the high contact angle (≈130°) when liquid. Consequently the cup is not destroyed by differences in thermal contraction on cooling and may be used for many experiments.

The measurements are made in flowing argon purified by passage through a titanium gettering furnace. The purity of the argon has not been measured but the manufacturer claims that oxygen is reduced to the 10^{-6} ppm level by the titanium getter. Additional purification of the argon is provided by the molybdenum susceptor which is an efficient oxygen getter[5]. The silicon used in these measurements is of six nines purity. The samples are cut from a large boule using a carbide wheel and then ground to fit the cup. The maximum diameter of the drops formed on melting is approximately 1.5 cm. Large drops are desirable to improve the precision of the measurement.[6]

The sessile drop technique is capable of highly accurate surface tension measurements[7]. The potential of the technique can be realized, however, only if the dimensions of the drop profile are measured to an accuracy of a few parts in 10^4. This requires a lens of large numerical aperture to obtain sufficient resolution. We use an f/5.6 enlarging lens with a 190 mm focal length in conjunction with a 4" x 5" camera body. The image of the drop is formed on a ground glass plate which is observed with a low power telescope for precise focussing. The drop is photographed using its own radiation on a high contrast, fine grained film designed for graphic arts work. The negatives are examined at 100x on a measuring microscope for analysis. The stage of the microscope can be rotated for the precise orientation of the negative required in the analysis[8].

In the normal experimental procedure the system is evacuated and degassed at just below the silicon melting point. After cooling and starting

the argon flow, the temperature is slowly raised to the maximum (≈1600°C) and the sessile drop photographed. The power is then reduced and the drop photographed again when temperature stability is achieved. This procedure is repeated until the drop freezes.

After cooling, the silicon drop is removed from the apparatus and subjected to Auger electron spectroscopic analysis. The only measurable impurities are carbon and oxygen which is typical of samples exposed to atmosphere. This layer is easily removed by argon ion sputtering. Although it is possible that the solidification process redistributes impurities to areas not accessible to the Auger analysis, we find no indication of any specimen contamination by the cup or susceptor.

Results and Discussion

Although previous study has found little difference in measurements with pure and oxygen doped silicon[9], there is other evidence suggesting that oxygen in dilute concentrations severely depresses the surface tension of silicon. Kingery and Humenik[10] observed the surface tension of liquid silicon to increase dramatically when the atmosphere was changed from argon to hydrogen. This increase in surface tension was attributed to a reduction of oxygen activity. Our measurements also show a strong sensitivity to what we believe to be a variation in oxygen pressure. In Figure 1 we show the surface tension calculated from a number of sessile drops in three different series of experiments. Although the atmosphere in all the experiments was nominally ultra pure argon, somewhat different conditions in each group of measurements produced different concentrations of impurities. Curve 1, the lowest data, reflects the effects of some atmospheric contamination of the flowing argon introduced through a small leak in the gas feed line

between the gettering furnace and the tube containing the silicon. In these experiments the development of a yellow deposit on the quartz tube near the molybdenum susceptor and downstream from the argon flow indicated oxygen in the system. This deposit is most likely MoO_3 formed by reaction with the susceptor and then sublimated[5]. The intermediate surface tension data (curve II) was obtained in early experiments in which the zirconia insulation was in contact with the molybdenum and may have been reduced somewhat. Furthermore, the system was not heated during the preliminary outgassing procedure. A much lighter deposit than in the previously described experiments was formed on the tube under these conditions.

The highest data shown in Figure 1 we believe to be free of any significant depression due to oxygen in the system. The measurements were preceded by a rigorous vacuum degassing at nearly 1400°C. There was no detectable deposit formation during the measurement and the solidified silicon samples had bright, smooth mirror like surfaces. A linear regression analysis of these data yields a K value of -0.279 mJ/m^2K. The probable error in K is .004 mJ/m^2K. The K values found for the other groups of data are shown on Figure 1.

Previous measurements of the surface tension of liquid silicon are listed in Table 1. These results scatter over the range of surface tensions observed in our work, probably because of variations in oxygen levels. Our high data lie slightly above that of Kingery and Humenik[10] obtained in pure hydrogen which supports our belief that the concentration of oxygen is very low in our measurements. We suggest, therefore, the following expression for the surface tension of clean silicon as a function of temperature:

$$\gamma = 885 - 0.28(T - 1410)$$

As mentioned earlier, there has been one previous measurement of the surface tension of silicon over a temperature range[2]. Lukin et al found the surface tension could be represented as

$$\gamma = 727 - .1044(T - 1410).$$

Their measurements were made using the sessile drop technique in purified helium atmospheres. Some of the difference between their K value and ours can be attributed to the use of different density data in the calculation of the surface tension. Lukin et al determined the density from the volume of the sessile drops. These measurements found a much smaller decrease in density with increasing temperature than the generally accepted dependence of Lucas[11] which we have used. If their surface tension values are adjusted to this latter density scale the surface tension temperature coefficient is decreased to -0.15 mJ/m^2K. Thus they find both a surface tension and $|K|$ significantly lower than the results of this work even after the density correction.

The lowering of the surface tension by adsorption of a surface active component is often accompanied by a reduction in the magnitude of K. This is the case with silicon over the range of impurity concentrations encountered in these measurements. In Figure 2 we plot $|K|$ as a function of γ at the melting point for the data of Figure 1 and the adjusted result of Lukin. The four points indicate an approximately linear variation of K with γ for the conditions of these experiments. Although the adjustment of the Lukin data into accord with our results may be fortuitous, their low surface tensions are very likely due to surface active impurities.

In conclusion, we have measured the surface tension of liquid silicon in purified argon atmospheres as a function of temperature. We find a

temperature coefficient near -0.28 mJ/m^2K. Our experiments show a high sensitivity of the surface tension to what we believe are low concentrations of oxygen. Thus we cannot rule out some effect of low levels of oxygen in our results. However, the highest surface tension values obtained in conditions which minimized the residual oxygen pressure are in good agreement with a previous measurement in pure hydrogen. We therefore believe that depression of the surface tension by oxygen is insignificant in these measurements.

References

1. W. E. Langlois, J. Crystal Growth 56 (1982) 15.

2. S. V. Lukin, V. I. Zhuchkov and N. A. Vatolin, J. of the Less-Common Metals 67 (1979) 399.

3. F. Bashforth and J. C. Adams, Capillary Action, University Press, Cambridge, 1883.

4. T. O'Donnell, M. Leipold and M. Hagan, Compatibility Studies of Various Refractory Materials in Contact with Molten Silicon, DOE/JPL-1012-7716, 1978.

5. S. Dushman, Scientific Foundations of Vacuum Technology (John Wiley & Sons, Inc., New York, 1962) 646.

6. J. V. Najdich and V. N. Eremenko, Fiz. Metal. i Metalloved II (1961) 883.

7. D. W. G. White, Trans. ASM 55 (1962) 757.

8. C. A. Smolders and E. M. Duyvis, Recueil 80 (1961) 635.

9. Yu. M. Shashkov and T. P. Kolesnikova, Russ, J. of Phys. Chem. 37 (1963) 747.

10. W. D. Kingery and M. Humenik, J. Phys. Chem. 57 (1953) 359.

11. L. D. Lucas, Mem. Sci. Rev. Met., 61 (1964) 1.

12. P. H. Keck and W. Van Horn, Phys. Rev. 91 (1953) 512.

13. V. P. Eljutin, V. I. Kostikov and V. Ya. Levin, Izv. Vys. Uch. Sav., Tsvetn Met. 2 (1970) 131.

14. N. K. Dshemilev, S. I. Popel and B. V. Zarevski, Fiz. Met. i Met. 18 (1964) 83.

15. P. V. Geld and M. S. Petrushevski, Izv. A. N., OTN, 3 (1961) 160.

Table 1

T (°C)	γ (mJ/m^2)	atm.	Ref.
1410	712	Vac.	9
1410	720	Argon	12
1500	825	Argon	13
1550	750	Vac.	14
1550	720	Vac.	15
1450	740	He.	10
1450	860	H_2	10
1450	874	Argon	This Work

Table 1. Summary of previous silicon surface tension measurements.

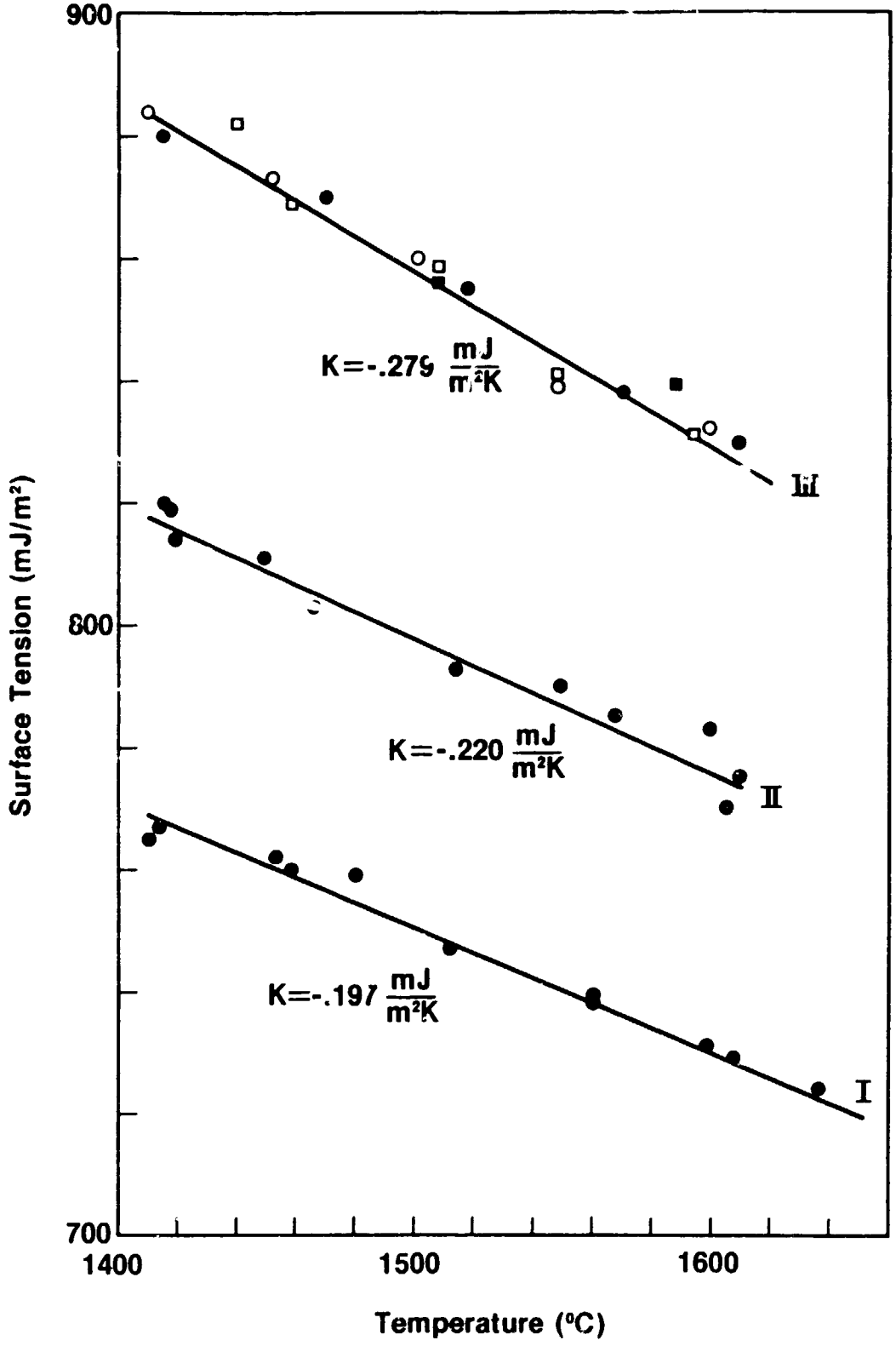

Figure 1. The surface tension of silicon as a function of temperature. The surface tension and K variations in the three groups of data are attributed to different concentrations of impurities. See text.

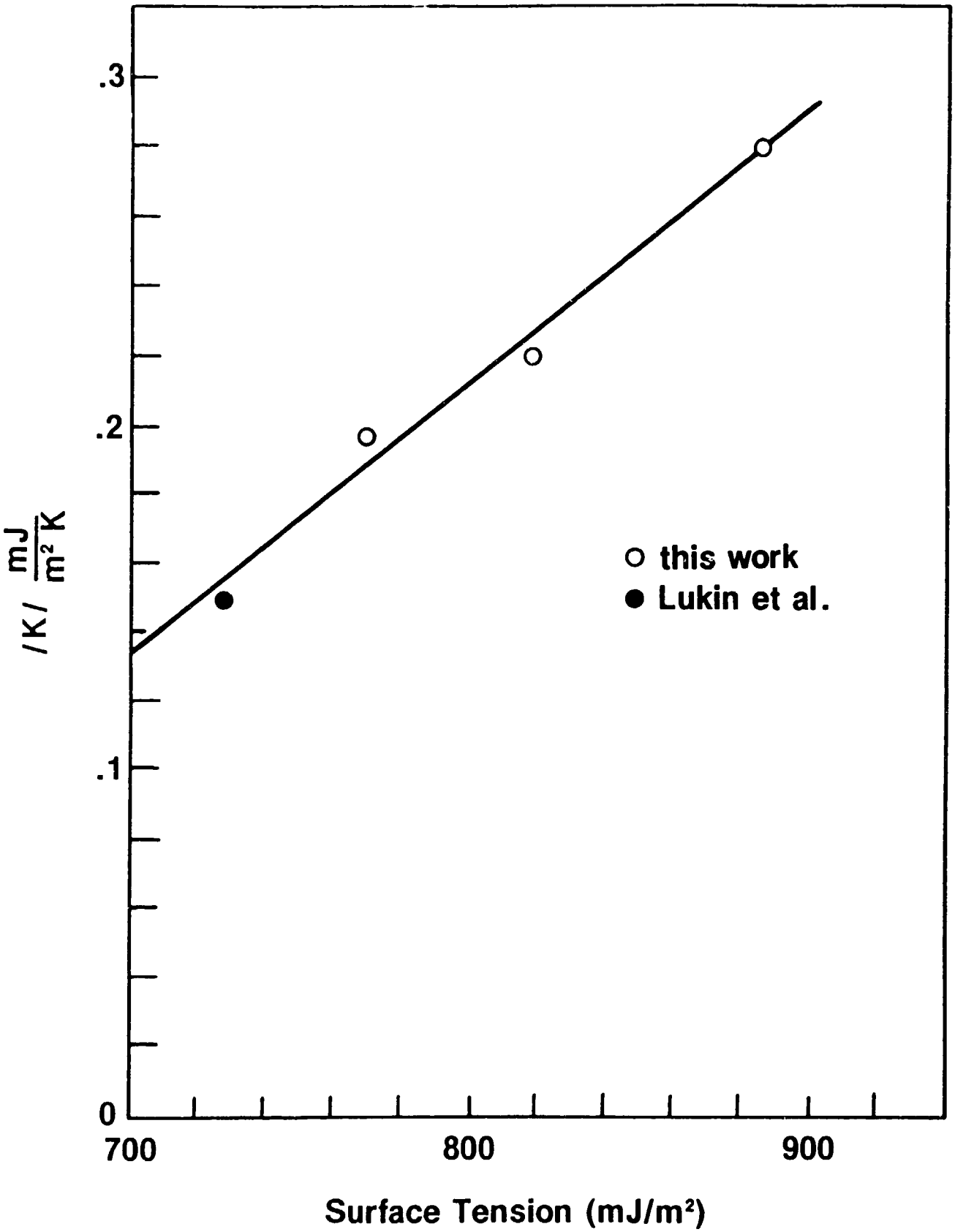

Figure 2. The absolute value of K as a function of the surface tension at the melting temperature.

Task 2
Convection During Unidirectional Solidification

S. R. Coriell and R. J. Schaefer
Metallurgy Division
Center for Materials Science

and

G. B. McFadden
Mathematical Analysis Division
Center for Applied Mathematics

SUMMARY

During solidification of a binary alloy at constant velocity vertically upwards, thermosolutal convection can occur if the solute rejection or preferential incorporation at the crystal-melt interface decreases the density of the melt. This convection can occur even in a microgravity environment, though, since it is basically a gravity driven flow it will be much more pronounced in earth-bound experiments than in space flight. A number of numerical calculations of the solute, temperature, and flow fields have been carried out using previously developed algorithms for Schmidt numbers Sc = 1, 10, 81. The time periodic flow, which occurs over a narrow range of parameters, has been further investigated.

Experimental observations of the interaction of flow fields with the crystal-melt interface during the unidirectional upward solidification of succinonitrile containing ethanol have shown how the interface shape correlates to different fluid flow patterns. Asymmetries in the thermal environment are found to play an important role, which is dependent upon the crystal growth velocity. In addition, the presence of a vapor bubble at the solid-liquid interface is sometimes found to induce vigorous convection.

The general problem of the interaction of flow fields with crystal-melt interfaces has been investigated by linear stability calculations for

the case of a flow parallel to a crystal-melt interface. This research, in collaboration with R. F. Sekerka of Carnegie-Mellon University and M. E. Glicksman and colleagues at Rensselaer Polytechnic Institute, has demonstrated a coupling between hydrodynamic and morphological instabilities. The calculations are in general agreement with experiments carried out by Glicksman and colleagues on succinonitrile.

Introduction

The general aim of this task is the theoretical and experimental study of the fluid flow and solute segregation which occur during solidification. The nature of the fluid flow, its effect on the shape of the crystal-melt interface and on the resulting distribution of solutes is examined. In particular, the role of solutal convection (gravity driven flow due to solute gradients) during the vertical directional solidification of a binary alloy is considered both theoretically and experimentally.

We present a discussion of the numerical calculations first and then a description of the experiments: each section can be read independently. The results of a number of new calculations of thermosolutal convection are presented. In particular it appears that the time periodic behavior previously found is related to the second eigenmode in linear theory. A few results for the lead-tin system are also given.

A number of manuscripts have been submitted for publication during the year, viz., (1) Thermosolutal Convection During Directional Solidification, G. B. McFadden, R. G. Rehm, S. R. Coriell, W. Chuck, and K. A. Morrison, Met. Trans.; (2) Asymmetric Instabilities in Buoyancy-Driven Flow in a Tall Vertical Annulus, G. B. McFadden, S. R. Coriell, R. F. Boisvert, and M. E. Glicksman, Phys. Fluids; (3) Morphological Stability in the Presence of Fluid Flow in the Melt, G. B. McFadden, S. R. Coriell, R. F. Boisvert, M. E. Glicksman, and Q. T. Fang, Met. Trans.; (4) Effect of a Forced Couette Flow on Coupled Convective and Morphological Instabilities During Unidirectional Solidification, S. R. Coriell, G. B. McFadden, R. F. Boisvert, and R. F. Sekerka, J. Crystal Growth; (5) Convection and

Interface Instability During Alloy Solidification, S. R. Coriell, G. B. McFadden, R. G. Rehm, and M. E. Glicksman, Proceedings of Workshop on Solidification and Fluid Dynamics in the Earth's and Space Laboratory, Aachen; (6) Convection-Induced Distortion of a Solid-Liquid Interface, R. J. Schaefer and S. R. Coriell, Met. Trans. The results in (1) and (5) are based on previous NBS reports; the results in (2), (3), (4), and (6) are new and these manuscripts are attached in Appendices (A-D).

The manuscript Coupled Convective Instabilities at Crystal-Melt Interfaces, S. R. Coriell, G. B. McFadden, R. F. Boisvert, M. E. Glicksman, and Q. T. Fang (Appendix in a previous report[2]) has been accepted for publication in the Journal of Crystal Growth.

Numerical Results

The basic equations and methods for calculating the fluid velocity, solute, and temperature fields during directional solidification of a binary alloy have been previously reported[1,2]. The notation used is defined in Tables I and II.

Since it appears that the oscillations in time previously[2] reported are correlated with the second eigenmode of linear theory, we have carried out linear stability calculations for Schmidt numbers Sc = 1, 10, and 81. Typically semiconductors have Sc = 10 and metals Sc = 100. The results are shown in Figs. 1-3. For Sc = 1, the first three eigenmodes are shown; the dashed curve indicates how the wavelength of the fastest growing mode varies with the degree of instability. Figures 2-3 are similar although only the first two eigenmodes are shown. Previous nonlinear calculations for Sc = 10 showed time periodic behavior for a narrow range of wavelengths and values of Rs/Rs*. Comparison of Fig. 2 with Fig. 4 of reference 2 indicates that the non-linear time periodic behavior occurs in the vicinity

of the second eigenmode of linear theory.

We have carried out a number of calculations for the lead-tin system for a growth velocity of $2(10^{-4})$ cm/s and a temperature gradient in the liquid of 200 K/cm. The dimensionless parameters are then $k_L/k_S = \kappa/\kappa_S = 0.535$, $k = 0.3$, $Sc = 81$, $Pr = 0.0225$, $Ra = 43.48$, $Rs^* = 82.79$. We report the results of four computations:

(Pb 1) $Rs/Rs^* = 1.51$, $U = 0.0741$, $H/\lambda = 1.303$, MESH (12, 54),

(Pb 2) $Rs/Rs^* = 2.13$, $U = 0.0741$, $H/\lambda = 1.600$, MESH(12, 54),

(Pb 3) $Rs/Rs^* = 3.86$, $U = 0.123$, $H/\lambda = 3.223$, MESH(12, 90),

(Pb 4) $Rs/Rs^* = 4.28$, $U = 0.123$, $H/\lambda = 1.790$, MESH(12, 90).

The values given as MESH(N, M) indicate the number of intervals (N, M) in the λ and y direction, respectively; the calculation is carried out over half a wavelength in the x-direction. In the first three calculations, the relationship between wavelength λ and degree of instability Rs/Rs^* was chosen to approximate the fastest growing mode of instability from linear theory (see Fig. 3), and steady state behavior was found. For calculations Pb 1, Pb 2, and Pb 3, the relative solute segregation at the crystal melt-interface (the ratio of maximum minus minimum to average concentration) is 0.378, 0.319, and 0.264 while the ratio of the maximum flow velocity and the crystal growth velocity is 3.3, 4.7, and 8.5, respectively.

The wavelength and degree of instability Rs/Rs^* for calculation Pb 4 were chosen in the region where time periodic flow might occur based on our previous results for $Sc = 10$ and the location of the second eigenmode. Oscillatory behavior did occur and the stream function and concentration field at four different times during one period of oscillation is shown

in Figs. 4-5, respectively. The period of oscillation corresponds to about 880 s; in this time the crystal has grown 0.18 cm or 1.2 (D/V). Because of the large Schmidt number, calculations for the lead-tin system require very large computation times, e.g., about 3 hours of CPU time (Univac 1100/82) per dimensionless time unit for the oscillatory behavior shown in Figs. 4-5, where the dimensionless time exceeds 35.

We have also initiated some calculations for Sc = 1, where the behavior appears qualitatively similar to the larger Schmidt number cases (compare Figs. 1-3). The shorter computer times allow a more detailed study of the variation of the flow fields with wavelength and solutal Rayleigh number. One of the most interesting results is the dependence of the steady state on the initial state (non-uniqueness of the steady state). Figs. 6 and 7 show two different steady states with identical values of the dimensionless variables, but with different initial conditions. The relationship between non-uniqueness and oscillatory behavior will be further investigated.

Several calculations have been carried out for reduced but constant gravitational accelerations. We plan to modify the algorithm to permit calculations for variation of the direction and magnitude of the gravitational acceleration with time. In some circumstances it appears that growth vertically downward would be preferable. Linear and non-linear computations for this case will be undertaken.

Experimental Results

Previously reported experiments[2] demonstrated that convective flow patterns present during the unidirectional growth of succinonitrile containing ethanol could result in the formation of a macroscopic pit in

the solid-liquid interface, with a cellular microstructure then developing within the pit. The convective flow in these experiments was attributed to the effect of radial temperature gradients in the vicinity of the solid-liquid interface. These gradients were due to heat loss to the environment and to the generation of latent heat of fusion at the solid-liquid interface when solidification occurred. It was demonstrated that the activation of an auxiliary heater surrounding the solid-liquid interface could be effective in supressing the formation of the interface pit.

Additional measurements of the fluid flow above the solid-liquid interface have indicated the importance of the asymmetry of the temperature field. When heat losses are symmetrical, the fluid flow shows a toroidal pattern; downward along the walls of the sample, radially inward above the interface, and upward along the sample axis (Fig. 8a). When the sample is held stationary in this condition, marker particles tend to accumulate at the interface just above the point where the radial inward flow converges, and to flow upward in a concentrated stream along the axis of the torus (Fig. 9). Asymmetry of the thermal field causes the interface to become tilted and the axis of the torus to be shifted to the downhill side (Fig. 8b). Additional asymmetry causes the torus to pinch off on one side and the flow then forms a single transverse roll (Fig. 8c).

The asymmetric part of the heat losses becomes relatively less important when crystal growth is initiated, as a result of the large symmetric generation of heat of fusion. In response to this effect, the axis of the toroidal flow moves toward the center of the tube. Activation of the auxiliary heater surrounding the interface generally resulted in

a more asymmetric flow field either because the auxiliary heater itself was not symmetric or because the auxiliary heater cancelled the symmetric part of the heat losses but left the asymmetric part. Thus the elimination of the central interface depression when the auxiliary heater was activated can be attributed in part to the decrease in radial gradients but also in part to the change in the form of the flow field. Complete elimination of horizontal gradients (and subsequent elimination of thermal convection) by the use of auxiliary heaters is unlikely to be successful because of the difficulty of producing perfectly uniform transfer of heat to the specimen tube.

A very strong convective flow has been observed in the vicinity of a vapor bubble which was trapped at the solid-liquid interface. This bubble was formed when the sample was melted back into a region where the solid contained a shrinkage void. The flow pattern above this bubble was sometimes similar to that in samples containing no bubble but at other times it showed a localized counterrotating toroidal pattern directly above the bubble (Fig. 10). The velocities in this counterrotating flow were at least an order of magnitude faster than those normally present, and were fastest directly adjacent to the bubble surface. The counterrotating flow appeared to be most vigorous shortly after the bubble shifted its position. These observations indicate that the flow is driven by surface energy gradients along the liquid-vapor interface; bubble motions would cause sudden transient melting or solidification, thus increasing local temperature and concentration gradients and inducing more rapid flow. The effect would be especially significant under low gravity conditions, where the location of vapor bubbles is difficult to control. More

observations of this effect are planned, to clarify the relative roles of temperature and solute gradients.

References

1. R. J. Schaefer, S. R. Coriell, R. G. Rehm, and G. B. McFadden, NBSIR 82-2560 (ed. by J. R. Manning) p. 25 (1982).

2. R. J. Schaefer, S. R. Coriell, G. B. McFadden, and R. G. Rehm, NBSIR 83-2772 (ed. by J. R. Manning) p. 19 (1983).

Table I

Definition of Symbols Used for Physical Quantities

ν (kinematic viscosity)

κ (thermal diffusivity of melt)

κ_S (thermal diffusivity of crystal)

D (diffusion coefficient of melt)

g (acceleration of gravity)

α (thermal coefficient of expansion of melt)

α_C (solutal coefficient of expansion of melt)

k_L (thermal conductivity of melt)

k_S (thermal conductivity of crystal)

k (distribution coefficient)

C_∞ (bulk concentration of solute)

C_∞^* (bulk concentration corresponding to onset of convection)

G_L (temperature gradient in melt)

H (melt height)

V (crystal growth velocity)

λ (horizontal wavelength)

t (time)

Table II

Dimensionless Quantities Used in Calculations

Ratio of Thermal Conductivities k_L/k_S

Ratio of Thermal Diffusivities κ/κ_S

Distribution Coefficient $k = 0.3$

Schmidt number $Sc = \nu/D$

Prandtl number $Pr = \nu/\kappa$; $Pr_S = \nu/\kappa_S$

Thermal Rayleigh number $Ra = (g\alpha G_L/\nu\kappa)\ (D/V)^4$

Critical solutal Rayleigh number $Rs^* = (g\alpha_C C^*_\infty/\nu D)\ (D/V)^3$

Dimensionless crystal growth velocity $U = VH/\nu$

Solutal Rayleigh number $Rs = (g\alpha_C C_\infty/\nu D)\ (D/V)^3$

Ratio of melt height to horizontal wavelength H/λ

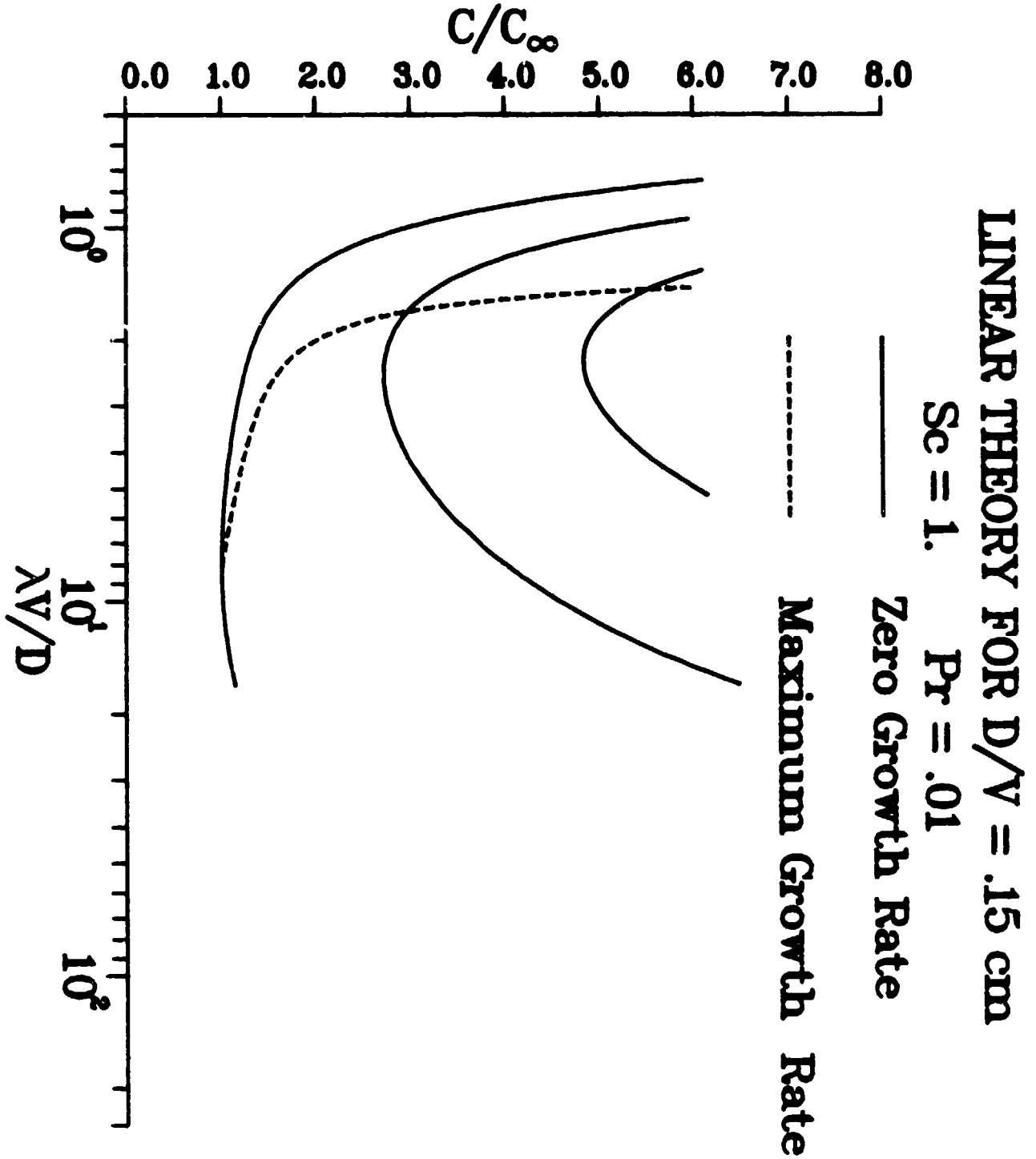

Fig. 1. The normalized concentration at the onset of instability during directional solidification as a function of the dimensionless wavelength of a sinusoidal perturbation. Three eigenmodes and the maximum growth rate are shown. For these curves $(k_L/k_S) = (\kappa/\kappa_S) = 1$, k = 0.3, Sc = 1, Pr = 0.01, Ra = 1268, Rs* = 961.

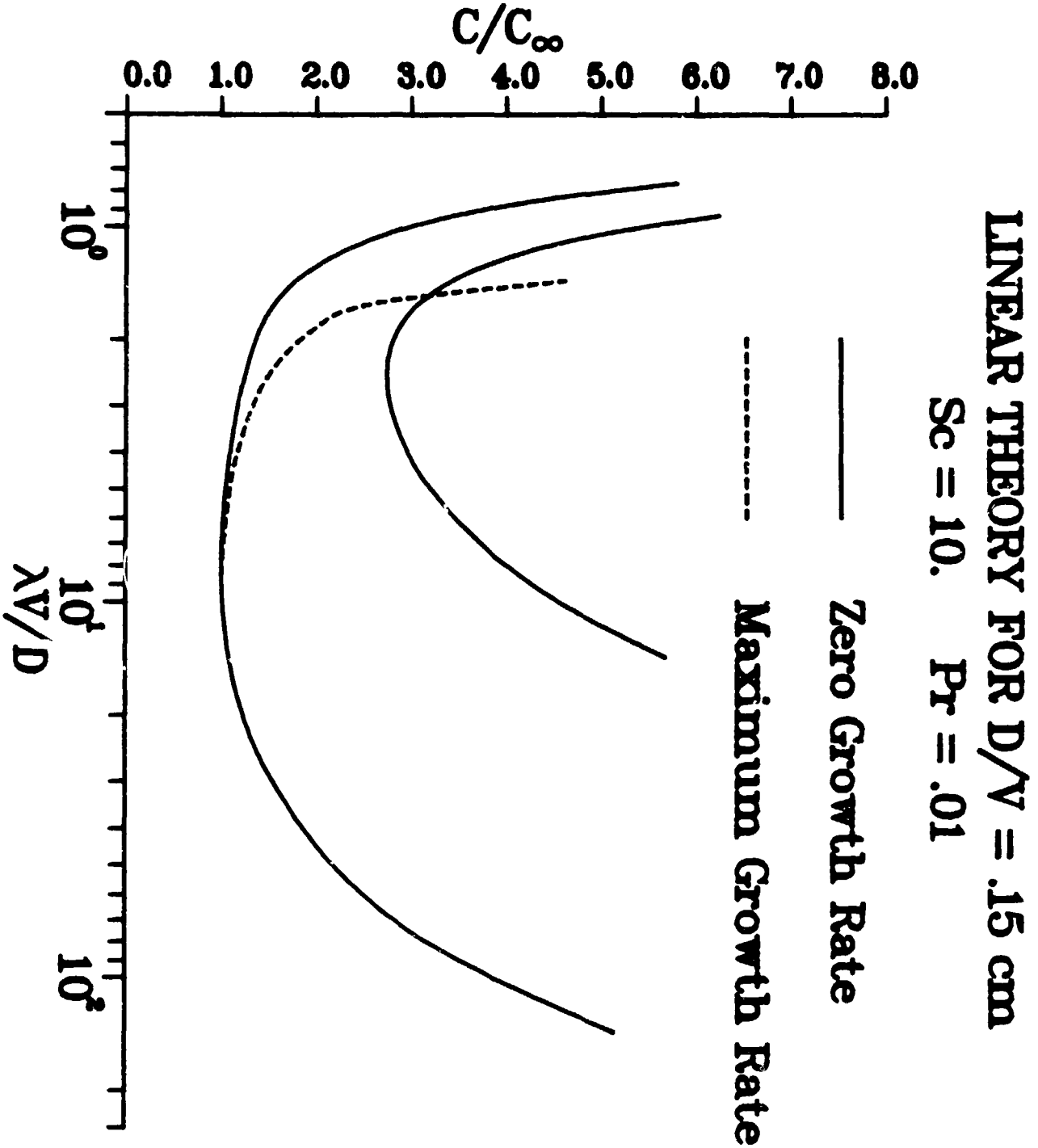

Fig. 2. The normalized concentration at the onset of instability during directional solidification as a function of the dimensionless wavelength of a sinusoidal perturbation. Two eigenmodes and the maximum growth rate are shown. For these curves $(k_L/k_S) = (\kappa/\kappa_S) = 1$, k = 0.3, Sc = 10, Pr = 0.01, Ra = 1268, Rs* = 963.

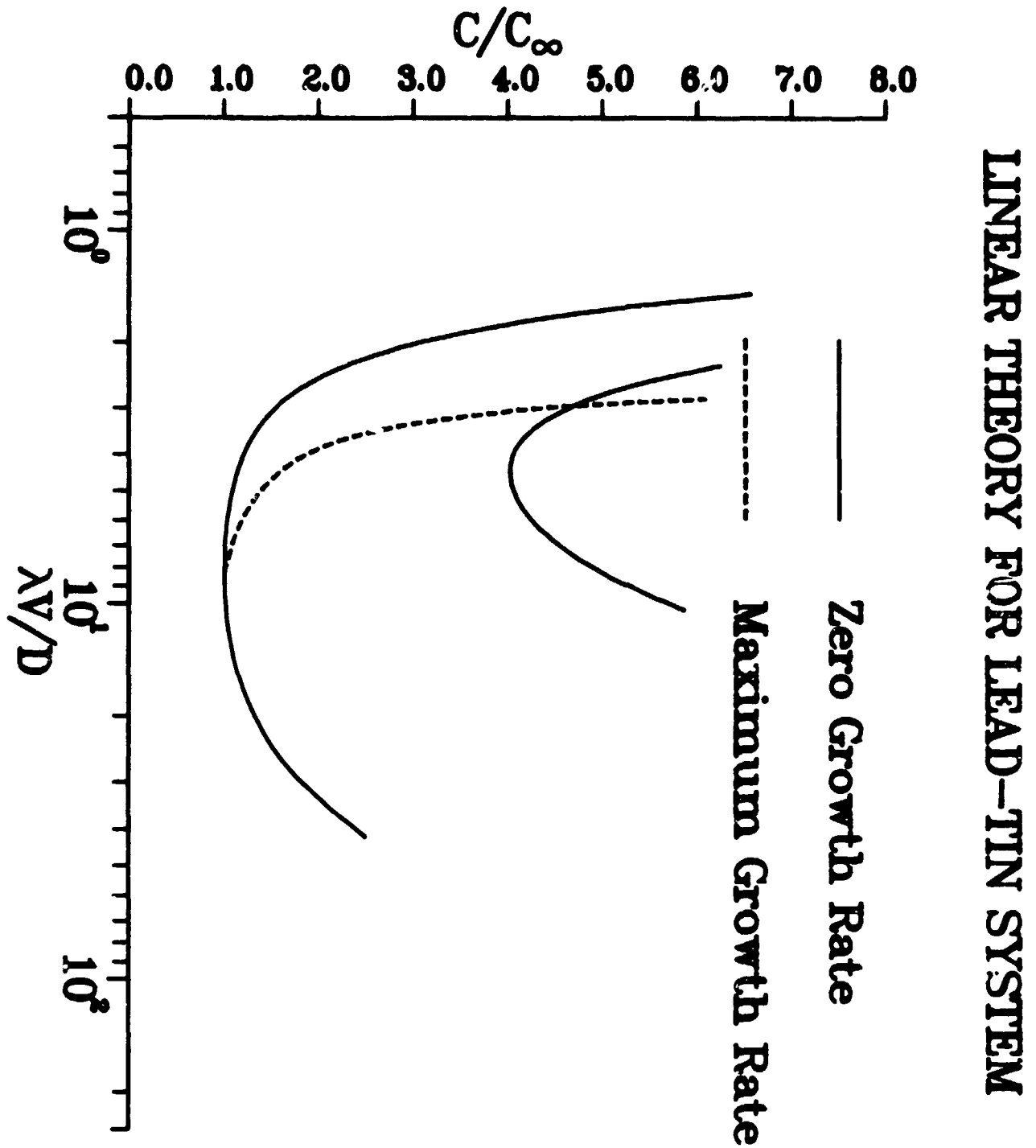

Fig. 3. The normalized concentration at the onset of instability during directional solidification of lead containing tin as a function of the dimensionless wavelength of a sinusoidal perturbation. Two eigenmodes and the maximum growth rate are shown. For these curves $(k_L/k_S) = (\kappa/\kappa_S) = 0.535$, k = 0.3, Sc = 81, Pr = 0.0225, Ra = 43.48, Rs* = 82.79.

RS= .35390+003 kA= .43430+002 SC= 81.0000 P= .0225 LV/D= 5.5866

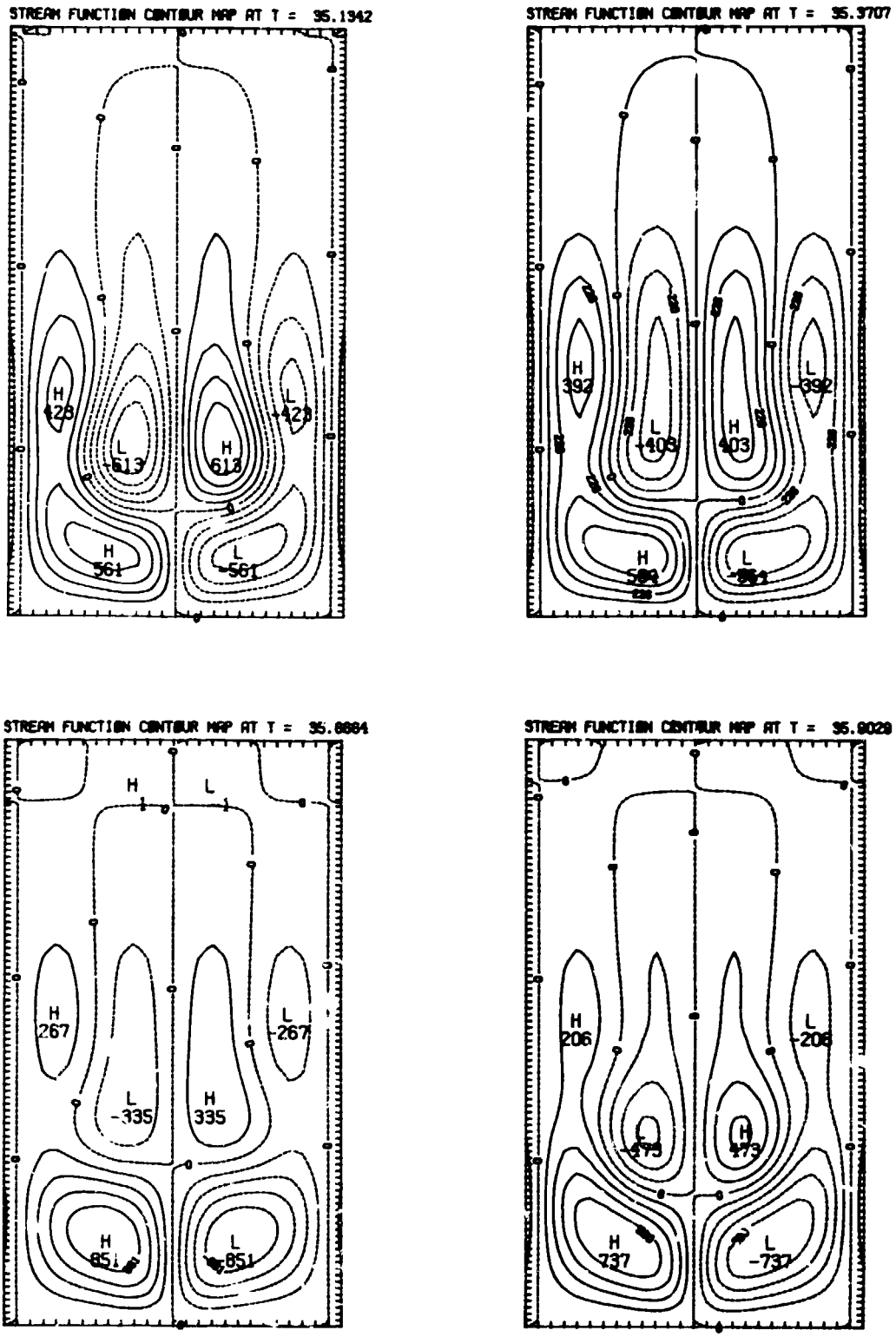

Fig. 4. The stream function as a function of position at four dimensionless times for the directional solidification of lead containing 0.0015 wt% tin at a growth velocity of $2(10^{-4})$ cm/s and a temperature gradient in the liquid of 200 K/cm. The streamfuncton is periodic in time; one dimensionless time unit corresponds to 926 s.

RS= .35390+003 RA= .43480+002 SC= 81.0000 P= .0225 LV/D= 5.5866

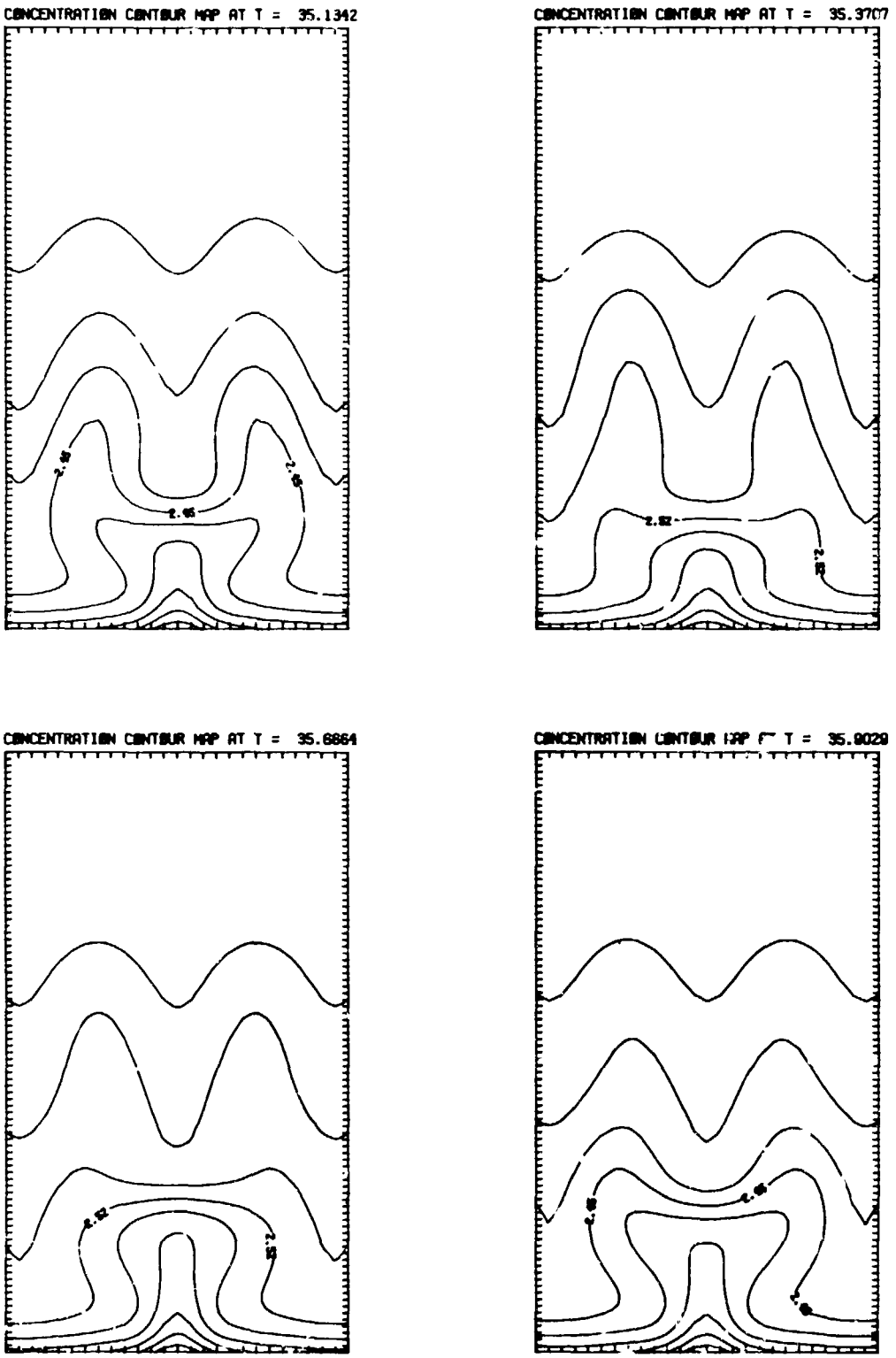

Fig. 5. The concentration field as a function of position for the same conditions as Fig. 4.

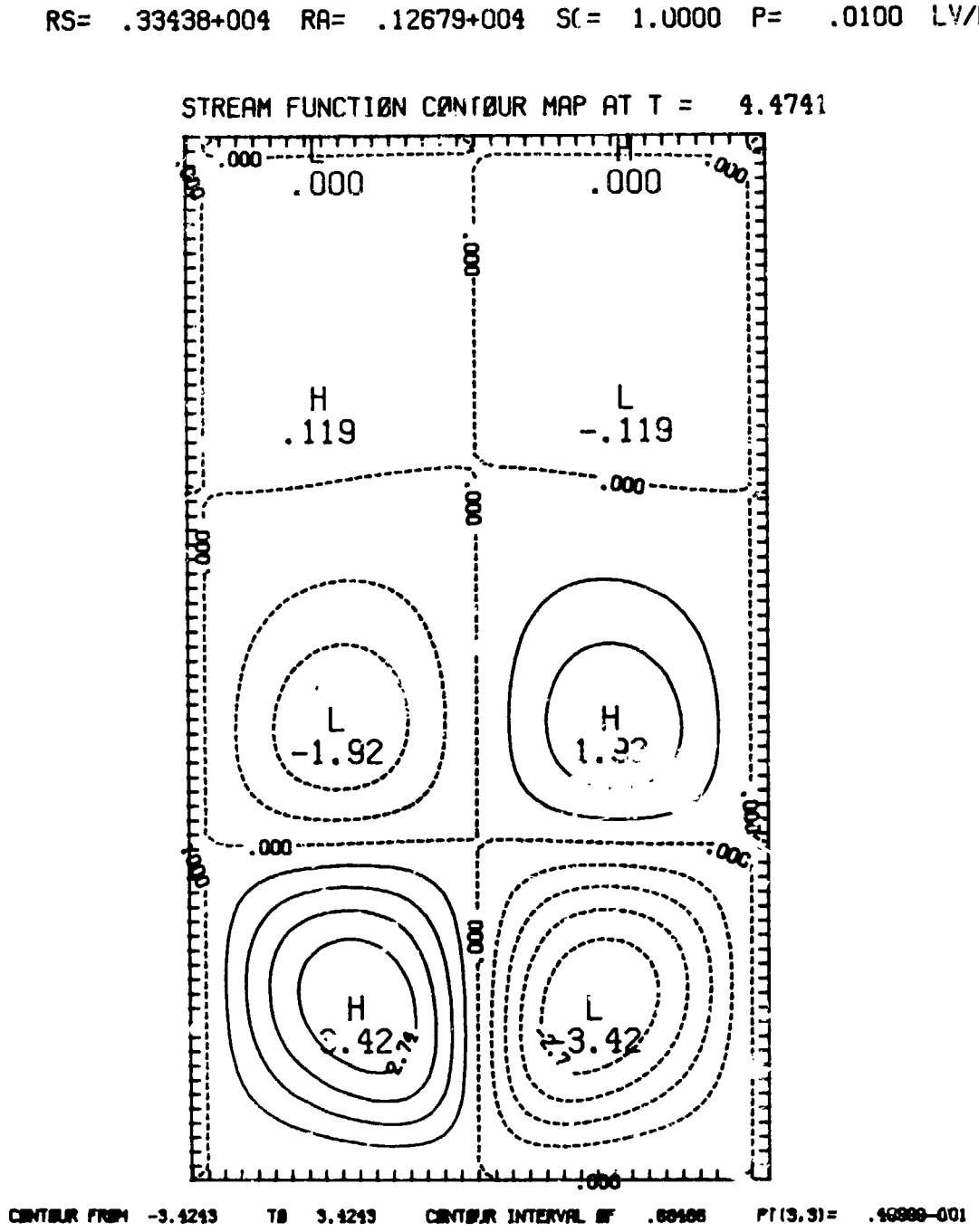

Fig. 6. The steady state stream function as a function of position; see Fig. 1 caption for values of the dimensionless parameters not given above (here L = λ).

RS= .33438+004 RA= .12679+004 SC= 1.0000 P= .0100 LV/D= 2.4644

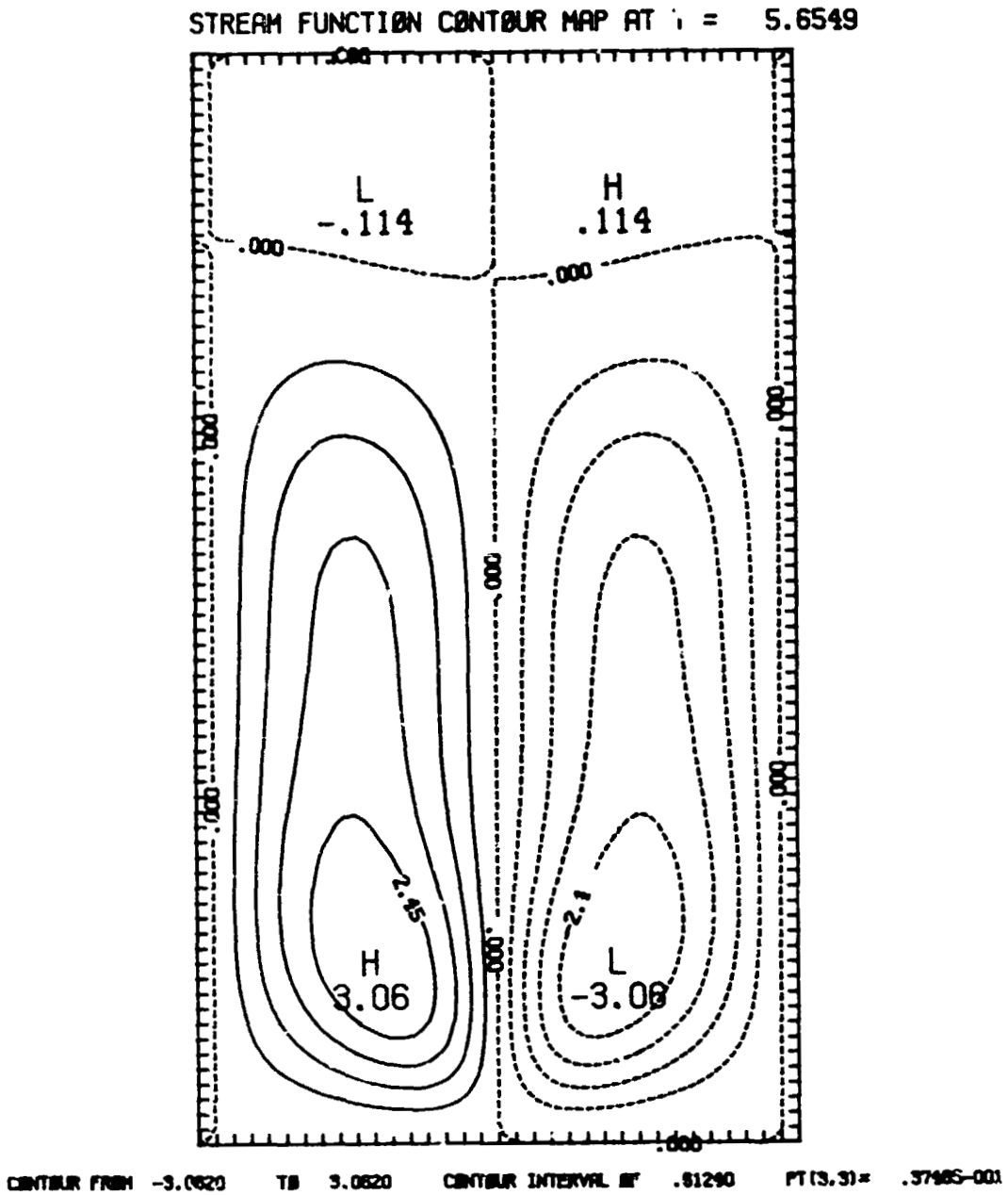

Fig. 7. The steady state stream function as a function of position for the same parameters as Fig. 6. There are two different steady state stream functions (non-uniqueness) depending on the initial conditions.

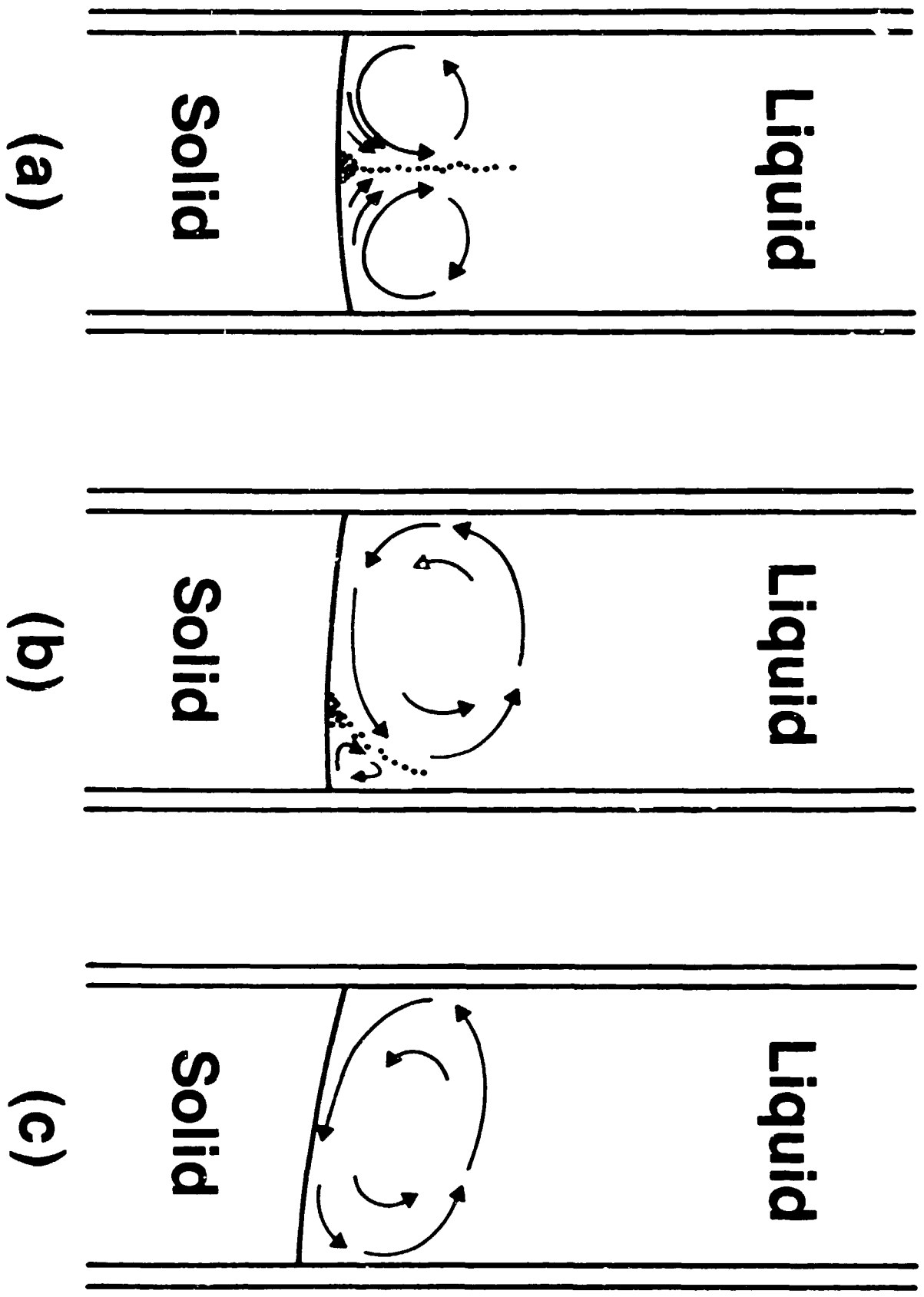

Fig. 8. Convective flow patterns above the solid-liquid interface with (a) symmetric, (b) slightly asymmetric, and (c) highly asymmetric heat losses.

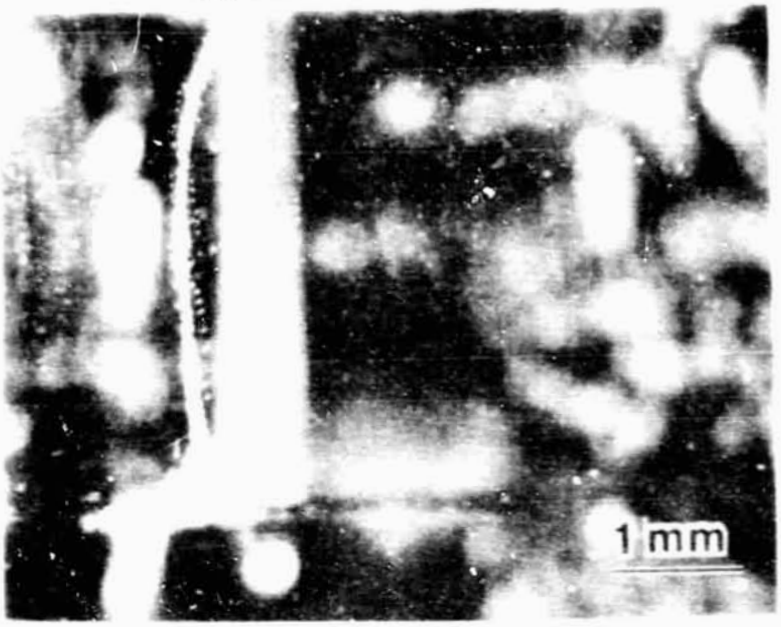

Fig. 9. Stream of particles along the axis of the toroidal flow field.

Fig. 10. Vapor bubble at the solid-liquid interface, with associated rapid counterrotating convective flow.

ASYMMETRIC INSTABILITIES IN BUOYANCY-DRIVEN FLOW IN A TALL VERTICAL ANNULUS

G.B. McFadden, S.R. Coriell, and R.F. Boisvert
National Bureau of Standards, Washington, D.C. 20234

and

M.E. Glicksman
Materials Engineering Department, Rensselaer Polytechnic Institute, Troy, New York 12181

ABSTRACT

Linear stability of the one-dimensional flow between infinite vertical coaxial cylinders induced by heating the inner cylinder is considered for various ratios κ of the inner radius to the outer radius, and for Prandtl numbers P appropriate to air and water. For air with P=0.71 the least stable disturbance is non-axisymmetric for $\kappa<0.44$ and is axisymmetric for $\kappa>0.44$, and in either case the instability is due to the action of the shear forces. For P=3.5, the situation is similar, except that the asymmetric shear mode is superceded by an axisymmetric instability driven by buoyancy forces for $0.03<\kappa<0.16$. Wave speeds, wave numbers, and critical Grashof numbers for these cases and for the case of zero Prandtl number are given.

INTRODUCTION

A basic problem in the study of heat transfer concerns the stability of the flow of a liquid placed between two vertical surfaces that are held at different temperatures[1]. Due to the variation of the fluid density with temperature, buoyancy forces typically cause the fluid to rise near the hotter surface and sink near the colder surface. The geometry considered in this note is a pair of infinite vertical coaxial cylinders with the inner cylinder maintained at a higher temperature than that of the outer cylinder. If the temperature difference is sufficiently small, the resulting flow is purely vertical and the lateral heat transport is due solely to conduction. If the temperature difference is large enough, however, the parallel flow becomes unstable and a more complex flow develops; heat is then convected laterally.

Several authors[2,3] have considered the linear stability of the basic parallel flow to disturbances that are axially symmetric. The purpose of this note is to extend these results to include asymmetric perturbations. The results indicate that for small ratios κ of the inner radius to the outer radius, and for small Prandtl numbers, the parallel flow first becomes unstable to asymmetric disturbances.

Asymmetric (helical) instabilities of a different type have also been observed experimentally and predicted by linear theory[4] for the situation in which the outer cylinder is crystalline succinonitrile and the fluid is molten succinonitrile with a Prandtl number of 23. In that case the feature of interest is the interaction between the non-rigid crystal-melt interface and the buoyancy-driven flow.

FORMULATION AND SOLUTION

The governing equations are taken to be the Navier-Stokes equations in the Oberbeck-Boussinesq approximation[5]. The equations are made dimensionless by scaling length by the radial gap L (outer radius minus inner radius), time by L^2/ν, where ν is the kinematic viscosity, temperature by the temperature difference ΔT between the cylinders, fluid velocity by $U = g\,\alpha\,L^2\,\Delta T/\nu$, where g is the magnitude of the gravitational acceleration which acts in the negative z direction and α is the coefficient of thermal expansion, and pressure by ρU^2, where ρ is the density. The unperturbed temperature field $T_0(r)$ and the vertical base flow velocity $W_0(r)$ depend only on the radial coordinate and are given by Choi and Korpela[2]. The perturbed quantities are assumed to have the form $f(r)\exp(i\omega z + in\phi + \sigma t)$, and linear instability is predicted when $Re(\sigma)>0$ for any wavenumbers ω and n. If the r-dependent part of the perturbed radial, azimuthal, and axial velocity components, the pressure, and the temperature are denoted by the complex quantities u,v,w,p, and T, respectively, the linearized governing equations reduce to the following set of ordinary differential equations:

$$Du + u/r + (inv)/r + i\omega w = 0,$$

$$(\sigma + i\omega GW_0)u + GDp = D^2u + Du/r - (\omega^2 + (1+n^2)/r^2)u - 2inv/r^2,$$

$$(\sigma + i\omega GW_0)v + inGp/r = D^2v + Dv/r - (\omega^2 + (1+n^2)/r^2)v + 2inu/r^2,$$

$$(\sigma + i\omega GW_0)w + G(DW_0)u + i\omega Gp = T + D^2w + Dw/r - (\omega^2 + n^2/r^2)w,$$

$$P(\sigma + i\omega GW_0)T + PG(DT_0)u = D^2T + DT/r - (\omega^2 + n^2/r^2)T\ .$$

Here the Grashof number $G=g\,\alpha\,\Delta T\,L^3/\nu^2$; the Prandtl number $P=\nu/k$; $D\equiv d/dr$; and k is the thermal diffusivity. The perturbed velocity components and temperature field all vanish at the inner cylinder $r=\kappa/(1-\kappa)$ and at the outer cylinder $r=1/(1-\kappa)$.

The equations can be recast as a set of 16 real first order ordinary differential equations. They are solved using the linear boundary value problem software SUPORT[6] in combination with the nonlinear equation solver SNSQE[7,8]. Following a method described by Keller[9], the complex boundary condition $u(1/(1-\kappa))=0$ is replaced by $Du(1/(1-\kappa))=1$ in order to obtain a nonsingular boundary value problem. The nonlinear solver then varies G and $Im(\sigma)$ for fixed values of $Re(\sigma)$, ω, n, κ, and P until the computed value of $u(1/(1-\kappa))$ is driven to zero. Values of G corresponding to marginal stability are obtained by setting $Re(\sigma)=0$ for fixed ω, n, κ, and P. For given values of P and κ, the critical Grashof number corresponds to the smallest marginal value of G taken over all values of ω and n. For $n=0$ this method reproduces to within 1% the critical Grashof numbers obtained by Choi and Korpela[2] using a different method.

RESULTS

As discussed by Hart[10], energy can be transferred from the main flow to the disturbance by the action of either the buoyancy forces or the shear forces (Reynolds stress). Eigenmodes corresponding to each mechanism can be identified. The Grashof number for marginal stability of the buoyant mode increases markedly as the Prandtl number is decreased, whereas the shear mode is relatively insensitive to the Prandtl number. The mechanism for instability in effect at the critical Grashof number depends on the specific value of P as well as κ.

Figure 1 shows marginal Grashof numbers vs κ for air with Prandtl number P=0.71. Two modes are shown: the dashed curve corresponds to azimuthal wavenumber n=0 and the solid curve corresponds to n=±1. Each point on the curves represents the minimum value of G with respect to ω with the other parameters fixed. The parallel flow is stable for Grashof numbers below both curves, and the critical Grashof number for any κ is given by the smaller value of the two curves.

The dashed curve is the symmetric shear mode discussed by Choi and Korpela[2] and Shaaban and Ozisik[3]. The solid curve is also a shear mode, and the geometry requires that the two modes become indistinguishable in the limit as κ approaches 1, which represents a planar vertical slot. The asymmetric mode lies slightly above the symmetric mode for $0.44<\kappa<1$ and the critical Grashof number in this range corresponds to a symmetric disturbance, as was observed experimentally for $\kappa=0.68$ by Choi and Korpela[2]. For $\kappa<0.44$ the critical Grashof number corresponds to an asymmetric distortion of the flow. The symmetric buoyant mode lies well above these curves at this Prandtl number and is not shown.

Selected values of the critical Grashof number, axial wave speed, and axial wavenumber are given in Table I. Positive wave speeds correspond to upward-moving waves. The disturbance is stationary for $\kappa=1$. Results for P=0 are also included in Table I. In this limit the temperature field has no effect on the flow and the problem reduces to the classical Orr-Sommerfeld equations.

Figure 2 shows results for P=3.5. (The Prandtl number of water has a value of 3.5 at about 50C but the thermophysical properties vary considerably with

temperature; the validity of the Boussinesq approximation for water therefore restricts the magnitude of the temperature difference ΔT). For this value the symmetric buoyant mode (dotted curve) has dropped sufficiently to become dominant. The two shear modes bear roughly the same relation to each other as before, but now the buoyant mode is the least stable mode over the range $0.03<\kappa<0.16$. Results for this case are also included in Table I. The buoyant mode is increasingly destabilized as the Prandtl number increases, so that for much higher values of P the critical Grashof numbers correspond to symmetric disturbances.

In summary, for low Prandtl numbers and for low ratios of the inner cylinder radius to the outer cylinder radius, the parallel flow first becomes unstable to asymmetric perturbations. This effect should be observable in experiments with air for radius ratios $\kappa<0.4$.

ACKNOWLEDGEMENT

This work was conducted under the support of the Microgravity Sciences Program, National Aeronautics and Space Administration.

REFERENCES

[1]G.Z. Gershuni, and E.M. Zhukhovitskii, Convective Stability of Incompressible Fluids (Keter, Jerusalem, 1976).

[2]I.G. Choi, and S.A. Korpela, J. Fluid Mech. 99, 725 (1980).

[3]A.H. Shaaban, and M.N. Ozisik, 7th Intl. Conf. of Heat Transfer, 1982, Munich, Germany.

[4]S.R. Coriell, R.F. Boisvert, J.I. Mickalonis, and M.E. Glicksman, Advances in Space Research (Proc. of 24th COSPAR Meeting) 3,95 (1983).

[5]S. Chandrasekhar, Hydrodynamic and Hydromagnetic Stability (Oxford University Press, London, 1961).

[6]M.R. Scott and H.A. Watts, SIAM J. Numerical Anal. 14, 40 (1977).

[7]SLATEC Common Math Library, National Energy Software Center, Argonne National Lab., Argonne, IL, written by K. L. Hiebert, based on Powell[8].

[8]M.J.D. Powell, in: Numerical Methods for Nonlinear Algebraic Equations, ed. P. Rabinowitz, Gordon and Breach, NY (1970).

[9]H.B. Keller, Numerical Solution of Two Point Boundary Value Problems, Regional Conference Series in Applied Mathematics 24, SIAM, Philadelphia (1976).

[10]J. Hart, J. Fluid Mech. 35, 547 (1971).

TABLE I

	κ=.99	κ=.60	κ=.20	κ=.10	κ=.01
P=0.0	n=0 (Sh)	n=0 (Sh)	n=1 (Sh)	n=1 (Sh)	n=1 (Sh)
G	7930.2	8319.4	10258.	10856.	14384.
ω	2.69	2.65	2.25	2.13	1.98
c	.24088	12.568	29.529	30.712	33.113
P=.71	n=0 (Sh)	n=0 (Sh)	n=1 (Sh)	n=1 (Sh)	n=1 (Sh)
G	8038.0	8512.4	10435.	10438.	10026.
ω	2.80	2.75	2.24	2.11	2.09
c	.25432	13.400	32.316	32.320	24.770
P=3.5	n=0 (Sh)	n=0 (Sh)	n=1 (Sh)	n=0 (B)	n=1 (Sh)
G	7857.1	8347.5	10582.	9712.6	14767.
ω	2.75	2.75	2.25	1.21	1.90
c	.24677	12.977	32.006	87.554	36.433

Table I. The critical Grashof number G, dimensionless axial wavenumber ω, and dimensionless axial wave speed $c=|\mathrm{Im}(\sigma)|/\omega$ (in units of ν/L) as functions of the radius ratio κ. '(Sh)' denotes a shear instablity and '(B)' denotes a buoyant instability.

FIGURE CAPTIONS

Figure 1. Marginal Grashof numbers vs radius ratio κ for Prandtl number P=.71. The dashed curve is the symmetric shear mode and the solid curve is the asymmetric shear mode. The symmetric mode lies slightly below the asymmetric mode for $\kappa>0.44$.

Figure 2. Marginal Grashof numbers vs radius ratio κ (logarithmic scale) for Prandtl number P=3.5. The dashed curve is the symmetric shear mode and the solid curve is the asymmetric shear mode. The dotted curve is the symmetric buoyant mode. The symmetric shear mode lies slightly below the asymmetric mode for large κ.

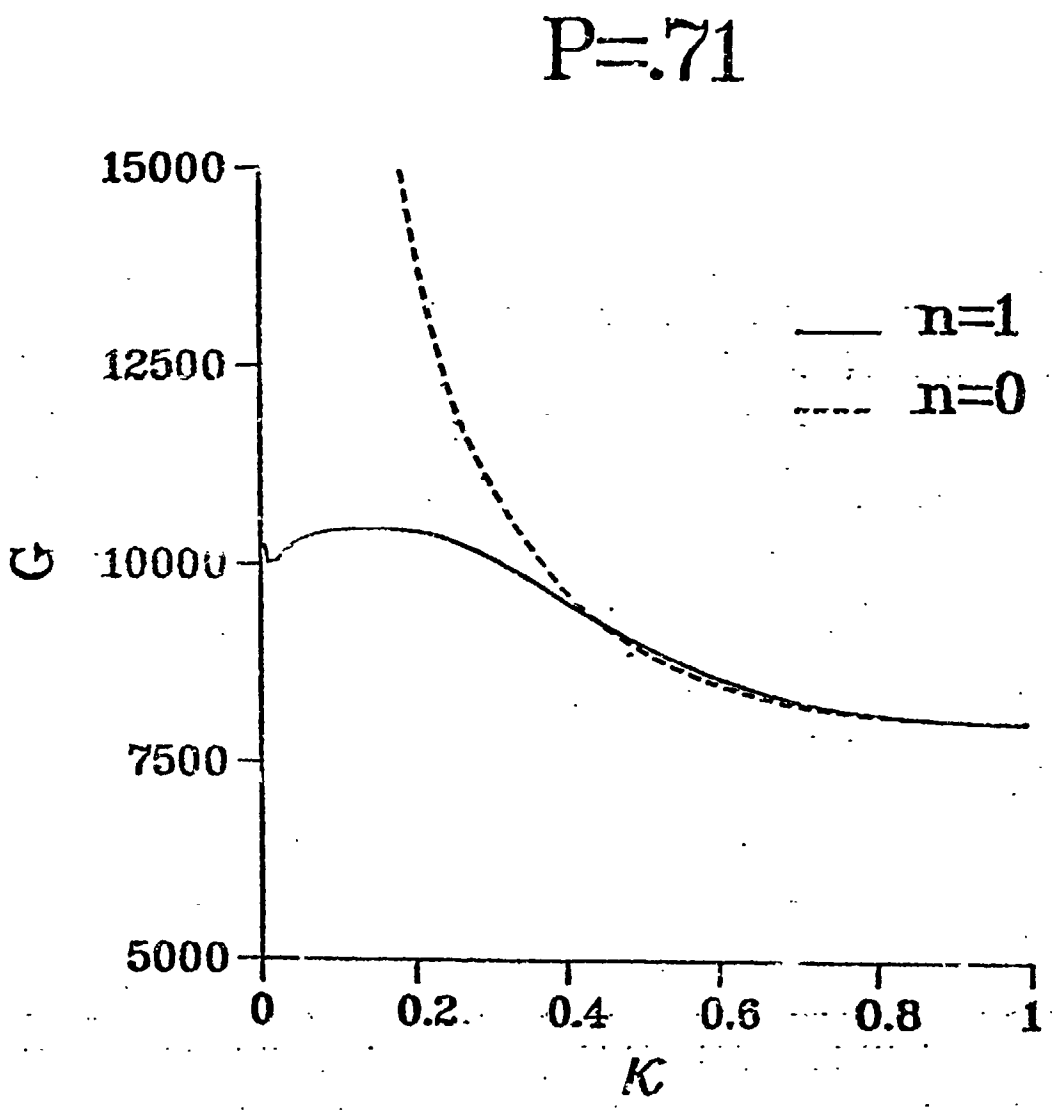

Figure 1

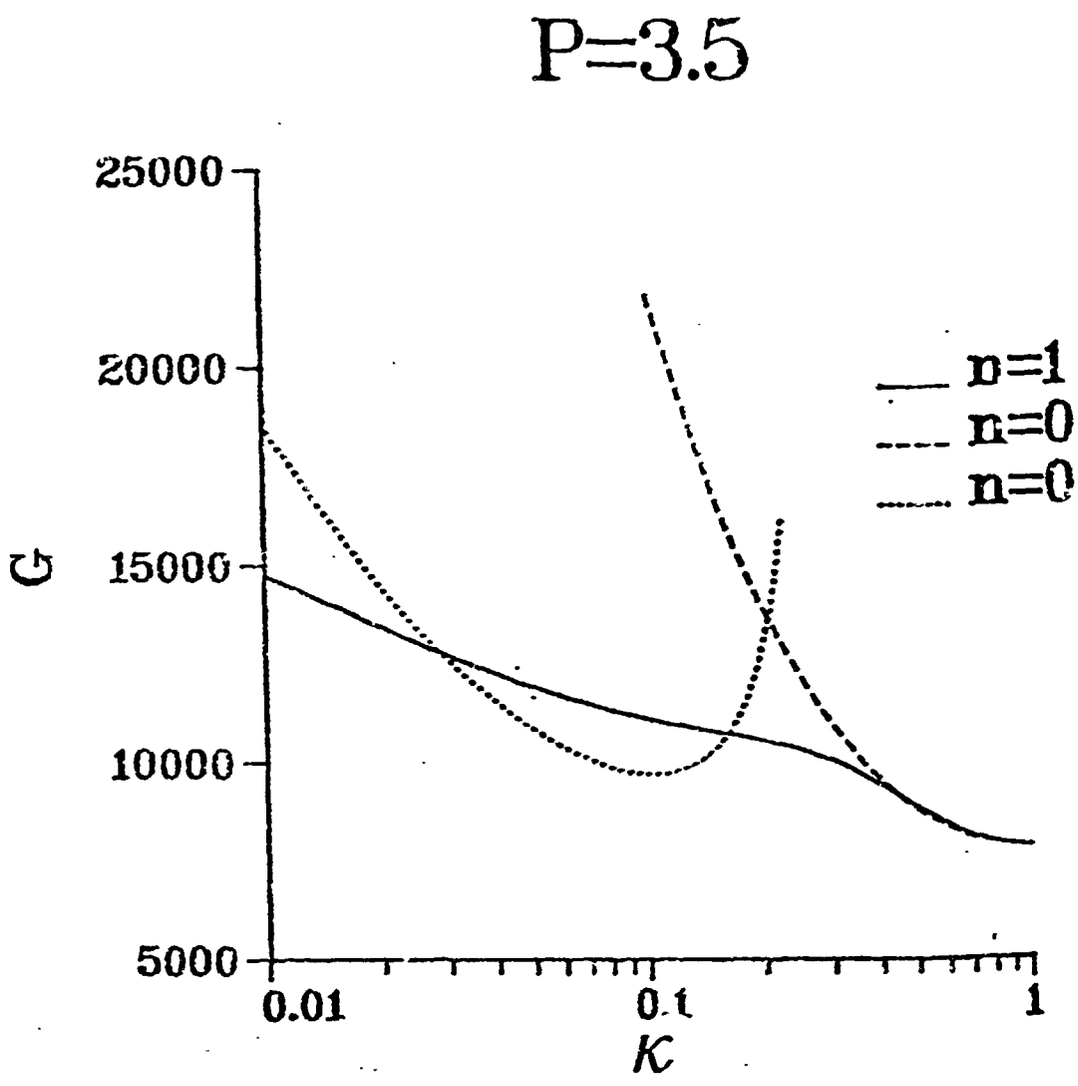

Figure 2

MORPHOLOGICAL STABILITY IN THE PRESENCE OF FLUID FLOW IN THE MELT

G.B. McFadden, S.R. Coriell, and R.F. Boisvert
National Bureau of Standards, Washington, DC 20234

and

M.E. Glicksman and Q.T. Fang
Materials Engineering Department
Rensselaer Polytechnic Institute
Troy, New York 12181

ABSTRACT

Recent experiments have shown that the presence of a vertical buoyancy-driven flow adjacent to an initially cylindrical crystal-melt interface may produce a time-dependent helical deformation of the interface, with a rotation period ranging from several minutes to many hours, depending upon the width of the melt. The temperature distribution is such that the interface is expected to be morphologically stable in the absence of fluid flow. A linear stability analysis reveals that the instability is due to a coupling between a basic hydrodynamic instability in the buoyant flow and the deformable boundary separating the two phases. The crystal-melt interface lowers the critical Grashof number of an analogous rigid-walled system by an order of magnitude for succinonitrile with a Prandtl number P=22.8; furthermore, the hydrodynamic mode that is actually destabilized by the interface is not the least stable mode in the rigid-walled system for P=22.8. The results show that the instability may be regarded either as a rather large alteration of a basic hydrodynamic instability by the crystal-melt interface, or as a significant modification of the morphological stability of the interface by the presence of the buoyant flow.

INTRODUCTION

The occurrence of fluid flow in the melt during solidification has received considerable attention, see e.g. the reviews by Hurle[1], Carruthers[2], and Pimputkar and Ostrach[3]. It is well known that convection can have a significant effect on the structure and properties of the resulting solid. In particular, the morphological stability[4-6] of the crystal-melt interface may be altered considerably by the presence of fluid flow. For example, Delves has shown[5] that a forced flow parallel to the interface helps stabilize the interface against a Mullins-Sekerka instability[6], while Coriell, et al.[7] show that thermosolutal instabilities in the melt may interact with the morphological instability in a complicated fashion and may in fact result in segregation at solute levels much lower than those predicted on the basis of morphological stability theory alone.

A surprising effect of convection on an otherwise stable solid-liquid interface has recenly been investigated experimentally by Fang, Glicksman and Mickalonis[8,9,10]. They studied a pure sample of succinonitrile (SCN) with a vertical, stationary cylindrical crystal-melt interface in a radial symmetric temperature field that increases into the liquid. Although according to morphological stability theory the cylindrical interface should be stable in the absence of convection, they found that the buoyancy-driven flow induced by the temperature gradient in the melt will under certain conditions produce a slowly rotating helical interface, accompanied by a more complex time-dependent flow. The critical Grashof number for the onset of this instability[11] is an order of magnitude lower than the critical Grashof numbers associated with hydrodynamic instabilities in rigid-walled containers[12,13].

Reference 14 contains a detailed description of the experiment and a comparison of experimental results with theoretical predictions of a linear stability analysis. A more detailed theoretical study for the related case of a planar geometry has also been performed[15], showing the dependence of the critical Grashof number on the Prandtl number of the melt. In this paper the experimental results are reviewed briefly, and some new theoretical results concerning the nature of the crystal-melt instability are presented. It is shown that the instability may be viewed either as a large alteration of a hydrodynamic instability by the solidification process, or as a significant modification to morphological stability theory due to the buoyancy-induced flow.

EXPERIMENT

The experiment consists of observing the flow state and internal configuration of a long glass cylinder containing solid succinonitrile with a platinum heating wire running along the axis of the cylinder. By passing a current through the wire while cooling the outside of the container in a isothermal bath of the proper temperature, a steady state cylindrical crystal-melt interface may be produced which separates the outer annulus of crystal from the core of melt near the wire, c.f. Figure 1a. The hotter fluid near the wire is less dense than the fluid near the interface, and a steady vertical flow is established such that the fluid flows upward near the wire and downward near the interface. If the wire temperature is slowly increased, the magnitude of the flow velocity increases until a critical melt gap and a critical temperature difference ΔT between the wire and the crystal-melt interface are reached for which the cylindrical interface is no longer stable. The crystal-melt interface is then observed to assume a

helical shape, c.f. Figure 1b.

The experimental results are summarized as follows:

1) A non-axisymmetric mode was observed when the Grashof number exceeds a critical value. The critical values range from 140 to 180, depending on the average radial gap width L of the melt at the onset of instability. (The width L at the onset may be varied by adjusting the bath temperature and the wire temperature properly.)

2) The longitudinal wave speed associated with the crystal-melt interface instability is about two orders of magnitude smaller than the maximum base flow velocity, and was found to scale as L^{-4}. The wave length, on the other hand, was found to be proportional to L.

3) The helical interfacial waves were observed to rotate with periods ranging from a few minutes to about ten hours, depending on the melt gap. These rotation periods were found to scale as $L^{4.82}$.

4) The helical wave associated with the interface instability can rotate with either a right-or a left-handed sense. It was found that there is a definite preference for left-handed helices for smaller value of L, whereas right-handed helices are preferred for large values of L. In addition, the helical waves were always found to travel upwards against gravity independent of their sense of rotation. Experiments also showed that the sense of rotation may be influenced by rotating the specimen tube. For further details of the experiment, see reference 10 and 14.

The remainder of this paper consists of a collection of new theoretical results obtained by linear stability analysis. A brief description of the governing equations and the method of numerical solution is also provided.

NUMERICAL METHOD

The experiment is modelled theoretically by assuming that the aspect ratio of the container is infinite. The governing equations are taken to be the Boussinesq approximation[16] to the Navier-Stokes equations for the velocity field, a convection-diffusion equation for the temperature in the melt, and a diffusion equation for the temperature in the crystal. The unperturbed problem then has a simple solution depending only on the radius, with the temperature field and vertical velocity field as given by Choi and Korpela[12]. The equations are made dimensionless by choosing the length scale to be the radial distance L between the unperturbed interface and the wire, the time scale to be L^2/ν, where ν is the kinematic viscosity of the melt, and the temperature scale to be ΔT, the temperature difference between the wire and the unperturbed crystal-melt interface. The velocity scale is taken to be ν/L, which differs from the scaling used in earlier papers[11,14,15]. For the purposes of a linear stability analysis the equations and boundary conditions are linearized about the unperturbed velocity and temperature fields and about the cylindrical interface. The z, ϕ, and t dependence in cylindrical coordinates of the perturbed quantities is assumed to have the form $\exp(\sigma t + i\omega z + in\phi)$, where ω is the axial wavenumber, n is the azimuthal wavenumber, and the complex time constant σ determines the temporal stability of the system; instability is predicted when $\sigma_r \equiv \mathrm{Re}(\sigma) > 0$. The resulting equations are

$$Du + u/r + (inv)/r + i\omega w = 0$$

$$(\sigma + i\omega W_0)u + Dp = D^2u + Du/r - (\omega^2 + (1+n^2)/r^2)u - 2inv/r^2$$

$$(\sigma + i\omega W_0)v + inp/r = D^2v + Dv/r - (\omega^2 + (1+n^2)/r^2)v + 2inu/r^2$$

$$(\sigma + i\omega W_0)w + (DW_0)u + iwp = D^2w + Dw/r - (\omega^2 + n^2/r^2)w + GT$$

$$P(\sigma + i\omega W_0)T + P(DT_0)u = D^2T + DT/r - (\omega^2 + n^2/r^2)T$$

in the melt, and

$$P_S\sigma T_S = D^2T_S + DT_S/r - (\omega^2 + n^2/r^2)T_S$$

in the crystal, where $D=d/dr$, $W_0(r)$ is the unperturbed vertical velocity, and $T_0(r)$ is the unperturbed temperature in the liquid. The r-dependent part of the perturbed radial, azimuthal, and axial velocity components, the pressure field, and the liquid and solid temperature fields are denoted by $u(r)$, $v(r)$, $w(r)$, $p(r)$, $T(r)$, and $T_S(r)$, respectively. The Prandtl number $P=\nu/K$, where K is the thermal diffusivity in the liquid, $P_S=\nu/K_S$, where K_S is the thermal diffusivity in the solid, and the Grashof number $G=g\alpha\Delta TL^3/\nu^2$, where α is the coefficient of volume expansion. With this choice of units, $W_0(r)$ is proportional to G.

The ratio of the wire radius to the unperturbed interface radius is denoted by κ. The boundary conditions at the wire radius $r=\kappa/(1-\kappa)$ are $u=v=w=T=0$. The solidification boundary conditions at the interface $r=1/(1-\kappa)$ are[7]

$$u = 0$$

$$v = 0$$

$$W = -\delta DW_0$$

$$T = -\delta DT_0$$

$$T_S = -\delta(k_L/k_S)DT_0$$

$$-\sigma\delta H = (k_L/k_S)DT - DT_S$$

where k_L and k_S are the liquid and solid thermal conductivities, and $H=\nu L_V/(k_S\Delta T)$, where L_V is the latent heat released per unit volume upon solidification. The perturbation of the interface has the form $\delta\exp(\sigma t + i\omega z + in\phi)$. It is also convenient to define $\Lambda=GH$. These boundary conditions have been simplified by assuming that the dimensionless capillarity constant $\gamma=GT_m\Gamma/(\Delta TL)=0$, where T_m is the melting point of SCN and Γ is the ratio of the solid-liquid surface tension to L_V, and the dimensionless density change upon solidification $\varepsilon=(\rho_S/\rho_L)-1=0$, where ρ_S and ρ_L are the densities of the solid and liquid, respectively. This is an excellent approximation for the experiment with SCN. The crystal extends to $r=L_S$, where the perturbed temperature vanishes.

The equations can be rewritten as a system of sixteen real first-order ordinary differential equations in the liquid. The solution procedure is similar to that employed in previous linear stability analyses[7]. Briefly, the eigenvalue problem is solved using the linear boundary value problem software SUPORT[17] in conjunction with the nonlinear equation solver SNSQE[18,19] following a method outlined by Keller[20].

It is also of interest to consider the case of a planar geometry[15]. This can be described by the above equations with r formally taken to be infinitely large and with the azimuthal velocity set to zero. The crystal is assumed to

extend to infinity. The unperturbed vertical flow field induced by buoyancy has a simple cubic profile and the unperturbed temperature field in the liquid is linear. Two methods were used for the planar case: the procedure outlined above and another method based on discretizing the equations using second-order accurate finite differences on a uniformly-spaced mesh to obtain a matrix eigenvalue problem. The latter method is useful for obtaining initial guesses for the nonlinear root finder in the first procedure as well as for performing quick scans in parameter space to identify various eigenmodes. The eigenvalues were computed using the subroutine F02GJF from the NAG library[21], which is based on the QZ algorithm[22].

NUMERICAL RESULTS

A comparison of theory and experiment[14] shows that the critical Grashof number, wavelength, and phase velocity of the instability are predicted rather well by linear stability theory. (However, the theory is unable to account for the observed tendency for left-handed helices to be favored for small liquid gaps, even when Coriolis force terms are included in the differential equations[14]). In this section the nature of the interfacial instability and its relationship to other unstable modes in the system are considered.

Marginal stability curves for a radius ratio of $\kappa=0.02$ are shown in Figure 2. The parameters used in computing these curves are $P=P_S=22.8$, $\Lambda=10170.0$, $k_L/k_S=1.0$, $\varepsilon=0.0283$, $\gamma=4.53(10^{-4})$, and $L_S=1.0$. The numerical results indicate that setting $\varepsilon=\gamma=0$ has a negligible effect on the marginal stability curves, and the rest of the results will all correspond to the case $\varepsilon=\gamma=0$. The cylindrical interface is stable for Grashof numbers less than 176, and is

first unstable to an asymmetric, helical disturbance (n=1). For sufficiently large Grashof numbers, the system is actually unstable to several different types of disturbance, and five of these modes are indicated in Figure 2. The curves labelled "n=0" represent axisymmetric disturbances, and those labelled "n=1" represent asymmetric disturbances. For each of the curves labelled "n=1" there is also an identical curve with n=-1 which corresponds to an eigenmode that differs only in its symmetry; that is, n=1 represents a left-handed helical disturbance and n=-1 represents a right-handed disturbance. Linear combinations of n=1 and n=-1 modes which are not helical are also possible.

The upper three curves correspond to instabilities that would also occur if the crystal-melt interface were replaced by a rigid isothermal wall[12,13,23]. The top two curves correspond to hydrodynamic instabilities driven by energy transferred from the main flow to the disturbance by the action of Reynolds stress[24] ("shear modes"), which represents momentum flux due to convection. The third curve (n=0) corresponds to instabilities due to energy transfer by the buoyancy forces ("buoyant modes"). For large κ there are both n=0 and n=1 buoyant modes, but for the n=1 case as κ is decreased the unstable region inside the closed marginal stability curves $\sigma_r=0$ (cf. Figure 3) becomes smaller and smaller. Eventually σ_r becomes negative everywhere and the marginal stability curves vanish altogether.

The lower two curves in Figure 2 represent the new modes that appear when a crystal-melt interface that can change shape is present rather than a rigid isothermal wall. The critical Grashof number G=176 occurs at a wavenumber ω=1.35. The disturbance takes the form of a travelling wave that moves in the upward direction, with $\sigma_i=\mathrm{Im}(\sigma)=-0.977(10^{-2})$. (Note that the unperturbed

flow is directed downward near the interface). This value of σ_i corresponds to a phase velocity that is two orders of magnitude lower than the maximum flow velocity. By contrast, the wavespeed for the buoyant mode is comparable to the base flow velocity. Values of G, ω, and σ_i at the minimum of each of the five curves are given in Table I.

The value of κ=0.02 used in Figure 2 is representative of the values studied by Fang, et al.[14]. A detailed numerical examination of the dependence of the crystal-melt instability on κ shows that for κ>0.8 the least stable mode is axisymmetric; that is, the relative positions of the lowest n=1 and n=0 modes shown in Figure 2 are reversed. A qualitatively similar dependence on κ is also obtained for the top two shear modes in the case of rigid boundaries[23].

The marginal stablity curves in Figure 2 give values of G and ω for which σ_r=0. More generally, a growth rate is determined by each value of G and ω, with different growth rates $\sigma_r(G,\omega)$ associated with each distinct mode of instability. Surprisingly, the crystal-melt instability and the shear instability with the same value of n share the same growth rate $\sigma_r(G,\omega)$; that is, the growth rate σ_r varies continuously along a path connecting the marginal stability curves for the crystal-melt mode and the shear mode. This result implies that the crystal-melt mode is in fact a branch of the ordinary hydrodynamic shear mode. The five marginal stability curves in Figure 2 arise from just three distinct relationships $\sigma_r(G,\omega)$ corresponding to the n=0 and n=1 shear modes and the n=0 buoyant mode. The crystal-melt interface apparently destabilizes the shear modes and allows instabilities to occur at significantly lower Grashof numbers.

This relationship can be observed more easily if the Prandtl number is decreased, which apparently stabilizes the crystal-melt mode while leaving the shear mode relatively unchanged[15]. Figure 4 shows marginal stability curves for P=0.148, κ=0.02, and n=1 for both a crystal-melt interface (solid curve) and a rigid isothermal wall (dashed curve). The other parameters have the same values as for Figure 2, except that ε and γ have been set to zero. The curves are similar for $\omega>1$, while for $\omega<1$ the development of the crystal-melt mode is clear. Values of σ_i for both cases are also included in the bottom half of the plot. Note the large variation in σ_i near ω=1, indicating the relatively slow wave speed of the crystal-melt mode. As the Prandtl number increases from P=0.148 to P=22.8 the marginal stability curve of the crystal-melt mode drops down and to the right while the interior maximum near ω=1 rises sharply.

In this context the crystal-melt mode may be viewed as a modification of a hydrodynamic instablity by the effect of a phase transition at one boundary. On the other hand, an equally valid interpretation is that the gravity-induced flow in the melt alters the morphological stabilty of the solid-liquid interface. With the temperature increasing from the interface into the liquid, morphological stability theory predicts that the cylindrical solid-liquid interface is stable to small disturbances in the absence of fluid flow. The theory also predicts that in other circumstances a solid-liquid interface may become unstable if the liquid is supercooled[25] or if enough solute is added to the liquid[6] (constitutional supercooling). The crystal-melt mode described here is yet another instance of interfacial instability, in this case due to a buoyancy-driven flow.

The curve labelled G=0 in Figure 5 shows the growth rate $\sigma_r<0$ of asymmetric disturbances to the cylindrical crystal-melt interface in the absence of fluid flow. For all wavenumbers ω the disturbances are damped out in time. This curve represents the n=1 version of the mode of interfacial deformation studied in classical morphological stability theory. The other curves show how this mode is destabilized by the presence of the gravity-induced flow parallel to the interface, with G=176 again corresponding to the critical Grashof number for which the interface is first unstable. In this figure the temperature difference between the interface and the outer cylinder is the same for all curves, and the variation in Grashof number may be considered to be caused by different values of the gravitational acceleration g. The point to be emphasized here is that it is the same eigenmode as is examined in morphological stability theory that is excited by the applied flow field. For this calculation $P=P_S=22.8$, $L_S=k_L/k_S=1.0$, and H=57.8.

The crystal-melt mode is thus due to the interaction of the non-rigid interface with the buoyant flow parallel to the interface. The dependence of this mode on the specific form of the flow field is considered next. For simplicity a planar geometry will be considered. The planar case also exhibits a crystal-melt mode, a buoyant mode, and a shear mode[15], with a critical Grashof number G=251, wavenumber $\omega=0.8$, and time constant $\sigma_i=-3.47(10^{-2})$ for $P=P_S=22.8$ and $\Lambda=1.017(10^4)$.

A natural question from the metallurgist's point of view is whether the interfacial instability depends only on the fluid flow in the immediate vicinity of the interface or whether it depends instead on details of the flow field farther out from the interface. For example, do similar instabilities occur when the cubic velocity profile of the buoyancy-driven flow is

replaced by simple Couette or Poiseuille flows having linear and quadratic velocity profiles, respectively? For H=16.95, P=22.8, P_S=0, and ω=0.7, in the absence of all fluid flow the growth rate of the morphological mode is σ_r=-7.44(10^{-2}). With buoyant flow the crystal-melt instability occurs for a critical Grashof number that produces a velocity shear dw/dr=20.17 at the interface. Setting G=0 and adding either enough Couette or enough Poiseuille flow to produce the same shear dw/dr=20.17 at the interface actually stabilizes this mode, with growth rates σ_r=-1.29(10^{-1}) and σ_r=-9.05(10^{-2}), respectively. The stabilizing effect is consistent with the results of Delves[5] showing that a forced flow has a stabilizing influence on a constitutionally supercooled, advancing interface. The matrix stability code was also employed to search for instabilities over some other parameter ranges, but no instances of interfacial instability were observed for either Couette or Poiseuille flow.

A related question is whether the purely hydrodynamic instability that is known to occur for planar Poiseuille flow[24] at a Reynolds number of 5772 is affected by the presence of a crystal-melt interface. This Reynolds number is based on the maximum flow velocity and the half-width of the liquid and corresponds to a much larger shear rate dw/dr=4.62(10^4) at the interface. The effect seems to be negligible: with H=16.95 and P=P_S=22.8, the critical Reynolds number is altered by only 0.003%. Figure 6 shows a plot of σ_r vs. ω for both the hydrodynamic mode (solid curve) and the morphological mode (dashed curve) for a Reynolds number R=5800. In contrast to the buoyant flow case (Figure 5) for which the shear mode coincides with the morphological mode, these two modes remain distinct, with the morphological mode stable and the hydrodynamic mode just unstable at this Reynolds number.

A more conservative approach to the question of the dependence of the crystal-melt mode on the velocity profile is taken in Figure 7, where a Couette flow is superposed on a buoyancy-driven flow with a Grashof number of G=600. The Couette flow is generated by moving the hot wall opposite the interface with a dimensionless velocity V (again based on ν/L). With no additional Couette flow the planar interface is unstable for $0.28<\omega<0.93$ at G=600, and this unstable range of wavenumbers corresponds to the interval inside the closed solid curve with V=0. The solid curve is the marginal stability curve with V and ω considered as parameters, and the planar interface is unstable outside the curve and is unstable inside it. The figure indicates that the interface becomes stable if enough Couette flow is present. For G=600 the net flow is nowhere downward for V>50 and is nowhere upward for V<-6.25, so that the figure indicates that the crystal-melt instability can occur even when the flow is unidirectional ($-11.23<V<-6.25$). The stabilization for large |V| is consistent with the argument that the existence of the crystal-melt instability hinges upon the presence of the shear instability, since in the limit of pure Couette motion it is known that the flow field is stable to all infinitesimal disturbances[24]. The exact details of the interaction are not straightforward, however, since, for example, as V decreases from zero the range of unstable values of ω decreases, then increases, and finally vanishes. Values for σ_i are included as the dashed curve in Figure 7. The Couette flow alters the wavespeed considerably; note, however, that σ_i remains negative, meaning that the travelling wave still moves upward.

It is perhaps worth emphasizing that the existence of the crystal-melt mode does not seem to be a simple consequence of the cubic velocity profile. The

instability exhibits a strong dependence on Prandtl number[15], whereas both the unperturbed velocity field and the unperturbed temperature field are independent of Prandtl number. For small Prandtl numbers, in which case the perturbed temperature becomes negigible, the crystal-melt mode is found to revert to the hydrodynamic shear instability that is present for rigid boundaries. For large Prandtl numbers the critical Grashof number of the crystal-melt mode is inversely proportional to the Prandtl number, so that the Rayleigh number given by the product PG approaches a constant for large P. Some simplification of the governing equations can be acheived for large Prandtl number, but the analysis of the resulting system still appears to be complicated.

SUMMARY

The observed helical instability results from a coupling between the hydrodynamic shear instability associated with the buoyant flow and the morphological mode of interface deformation that arises in ordinary morphological stability theory. The morphological mode apparently does not couple to the buoyant mode, which is actually less stable than is the shear mode for SCN, nor does it couple to the hydrodynamic instability associated with a Poiseuille flow. In one example, the addition of enough Couette flow stabilizes the crystal-melt interface, although it is possible to retain the helical instability while adding enough Couette flow to ensure that the flow is everywhere unidirectional. The observed tendency for left-handed helices to occur at small liquid gaps is not explained by the theory. A convincing physical argument that explains the coupling between the shear mode and the interface is also lacking.

ACKNOWLEDGEMENT

The authors gratefully acknowledge the support of the Microgravity Sciences Program, National Aeronautics and Space Administration. We also thank Drs. J. I. Mickalonis, S. Ostrach, R. G. Rehm, R. J. Schaefer, R. F. Sekerka, and J. A. Simmons for helpful discussions.

REFERENCES

[1]D. T. Hurle, in: Current Topics in Materials Science, 1977, vol 2, p. 549, ed. by E. Kaldis and H. J. Scheel, North-Holland, Amsterdam.

[2]J. R. Carruthers, in: Preparation and Properties of Solid State Materials, 1977, vol. 3, p. 1, ed. by W. R. Wilcox and R. A. Lefever, Dekker, New York.

[3]S. M. Pimputkar and S. Ostrach: J. Crystal Growth, 1981, vol. 55, p. 614.

[4]J. S. Langer: Rev. Mod. Phys., 1980, vol. 52, p. 1.

[5]R. T. Delves, in: Crystal Growth, 197 vol. 1, p. 40., ed. by B. R. Pamplin, Pergamon Press, Oxford.

[6]W. W. Mullins and R. F. Sekerka: J. Appl. Phys., 1964, vol. 35, p. 444.

[7]S. R. Coriell, M. R. Cordes, W. J. Boettinger, and R. F. Sekerka: J. Crystal Growth, 1980, vol. 49, p. 13.

[8]J. I. Mickalonis: M. S. Thesis,Materials Engineering Dept., Rensselaer Polytechnic Institute, 1982.

[9]M. E. Glicksman and J. I. Mickalonis: Proc. of the 16th Southestern Seminar on Thermal Sci., 1982, vol. 1, p. 505, Miami, FL.

[10]Q. T. Fang: M. S. Thesis,Materials Engineering Dept., Rensselaer Polytechnic Institute, 1983.

[11]S. R. Coriell, R. F. Boisvert, J. I. Mickalonis, and M. E. Glicksman: Advances in Space Research (Proc. of 24th COSPAR Meeting), 1983, vol. 3, no. 5, p. 95.

[12]I. G. Choi and S. A. Korpella: J. Fluid Mech., 1980, vol. 99, p. 725.

[13]A. H. Shaaban and M. N. Ozisik: 7th Intl. Conf. of Heat Transfer, 1982, Munich, Germany.

[14]Q. T. Fang, M. E. Glicksman, S. R. Coriell, G. B. McFadden, and R. F. Boisvert: submitted to J. Fluid Mech.

[15]S. R. Coriell, G. B. McFadden, R. F. Boisvert, M. E. Glicksman, and Q. T. Fang: to appear in J. Crystal Growth.

[16]S. Chandrasekhar: Hydrodynamic and Hydromagnetic Stability, Oxford University Press, London, 1961.

[17]M. R. Scott and H. A. Watts: SIAM J. Numerical Anal., 1977, vol. 14, p.40.

[18]SLATEC Common Math Library, National Energy Software Center, Argonne National Lab., Argonne, IL, written by K. L. Hiebert, based on Powell[10].

[19]M. J. D. Powell, in: Numerical Methods for Nonlinear Algebraic Equations, ed. P. Rabinowitz, Gordon and Breach, NY, 1970.

[20]H. B. Keller, Numerical Solution of Two Point Boundary Value Problems, Regional Conference Series in Applied Mathematics, 1976, vol. 24, SIAM, Philadelphi, PA.

[21]NAG Fortran Library Manual: Mark 9, vol. 4, Numerical Algorithms Group, Ltd., Oxford, 1982.

[22]C. B. Moler and G. W. Stewart: SIAM J. Numer. Anal., 1973, vol. 10, p. 241.

[23]G. B. McFadden, S. R. Coriell, R. F. Boisvert, and M. E. Glicksman, submitted to Phys. Fluids.

[24]P. G. Drazin and W. H. Reid: Hydrodynamic Stability, Cambridge University Press, Cambridge, 1981.

[25]W. W. Mullins and R. F. Sekerka: J. Appl. Phys., 1963, vol 34, p. 323.

TABLE I

G	ω	σ_i	n
175.72	1.35	$-9.7735(10^{-3})$	1
464.14	1.45	$-3.6457(10^{-2})$	0
2151.8	2.30	-43.729	0
13216.3	2.00	-69.049	1
60308.3	2.10	-708.84	0

Table I. Approximate minimum Grashof numbers G, axial wavenumbers ω, time constant σ_i, and azimuthal wave number n for the five neutral stability curves shown in Figure 2.

FIGURE CAPTIONS

Figure 1. Side view of the stable cylindrical mode (a), and helical mode (b). The black spot on the right hand side is the profile of a thermistor that detects temperature variations in the crystal.

Figure 2. The Grashof number at the onset of instability as a function of the axial wavenumber ω of a sinusoidal perturbation. The lowest two modes occur only for a crystal- melt interface, while the higher three modes occur for both a crystal-melt interface and a rigid interface. The curves are labelled with the azimuthal wavenumber n.

Figure 3. The Grashof number at the onset of instability as a function of the axial wavenumber ω of a sinusoidal perturbation for the n=1 buoyant mode with rigid boundaries. The solid curve corresponds to a radius ratio κ=0.325, and the dashed curve to κ=0.292.

Figure 4. The Grashof number G (top curves) and the time constant $-\sigma_i$ (bottom curves) at the onset of instability as a function of the axial wavenumber ω of a asymmetric perturbation for Prandtl number P=0.148, radius ratio κ=0.148. The solid curves correspond to crystal-melt boundary conditions, and the dashed curves to rigid wall boundary conditions.

Figure 5. The growth rate σ_r as a function of axial wavenumber ω for asymmetric perturbations for G=0, 90, 176, and 350. The lowest curve with G=0 corresponds to the morphological mode in the Mullins-Sekerka theory (in this case stable).

Figure 6. The growth rate σ_r as a function of the axial wavenumber ω for disturbances in a planar geometry with Reynolds number 5800. The unstable hydrodynamic mode (solid curve) is distinct from the stable morphological mode (dashed curve).

Figure 7. The Couette flow velocity V and the time constant $-\sigma_i$ as a function of the vertical wavenumber ω at the onset of instability in a planar geometry. The Grashof number G is fixed at G=600. The region inside the closed solid curve corresponds to unstable values, the region outside corresponds to stable values.

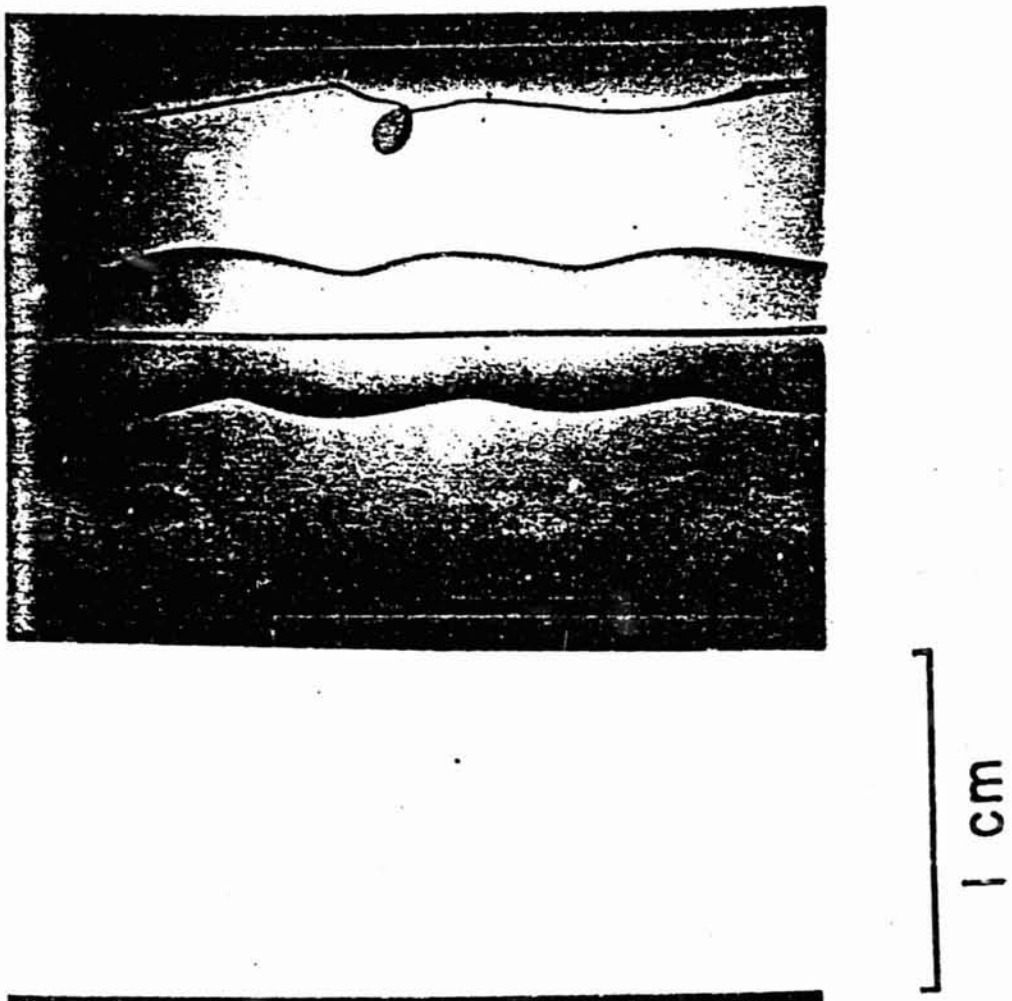

Figure 1

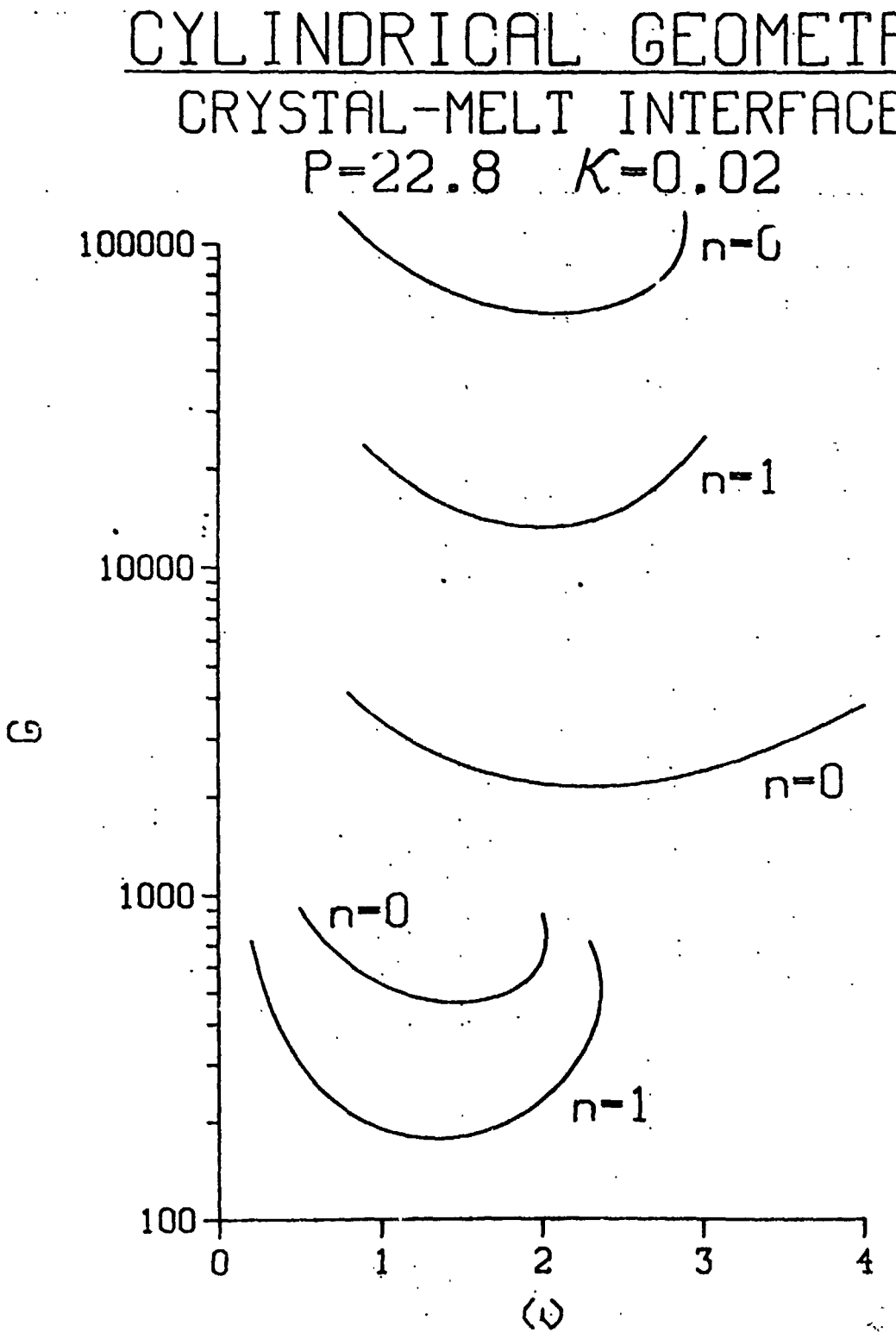
CYLINDRICAL GEOMETRY
CRYSTAL-MELT INTERFACE
P=22.8 K=0.02
100000
10000
1000
100
G
0
1
2
3
4
ω
n=0
n=1
n=0
n=0
n=1

Figure 2

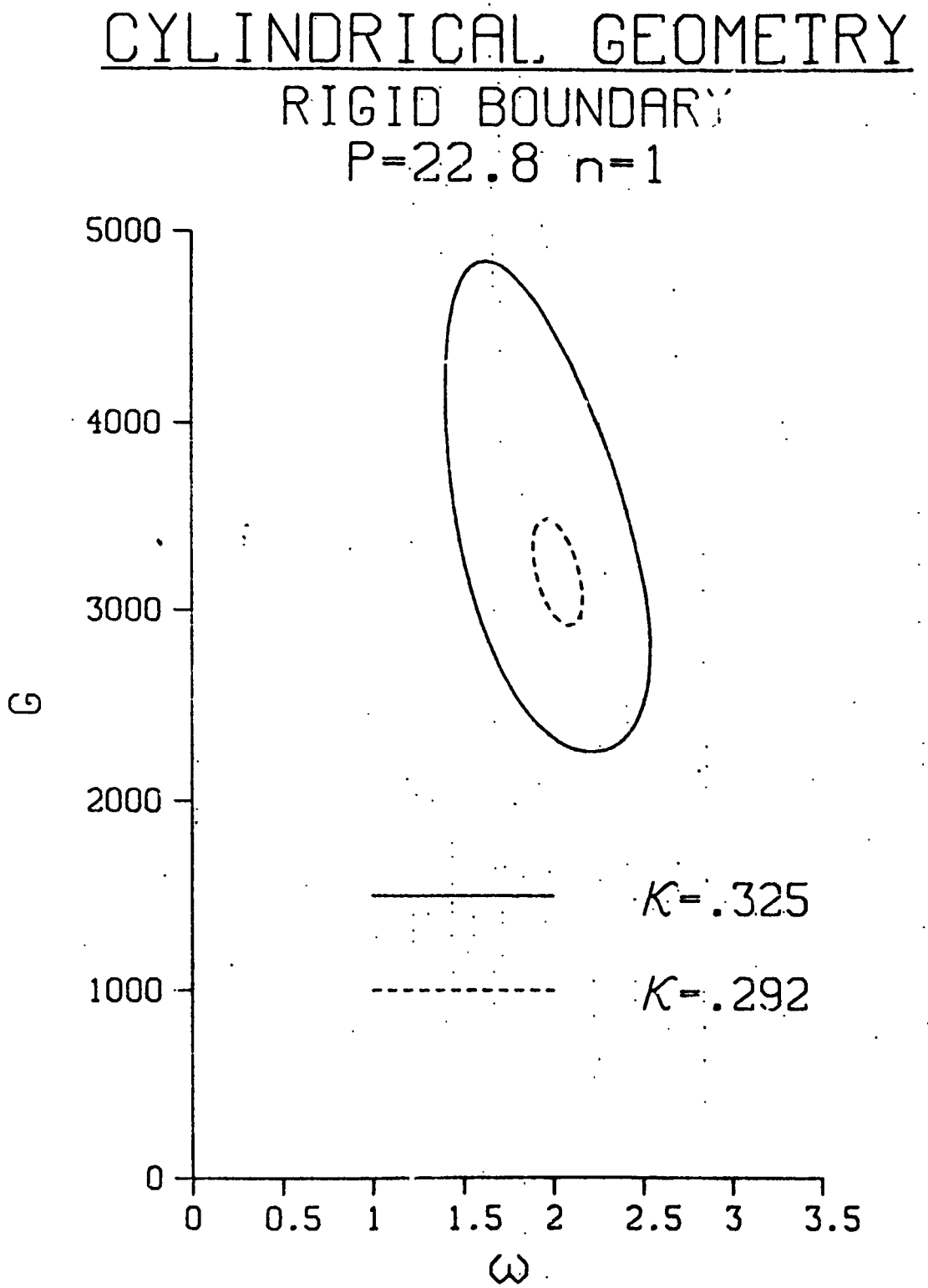
CYLINDRICAL GEOMETRY
RIGID BOUNDARY
P=22.8 n=1
5000
4000
3000
2000
1000
0
G
0
0.5
1
1.5
2
2.5
3
3.5
ω
K=.325
K=.292

Figure 3

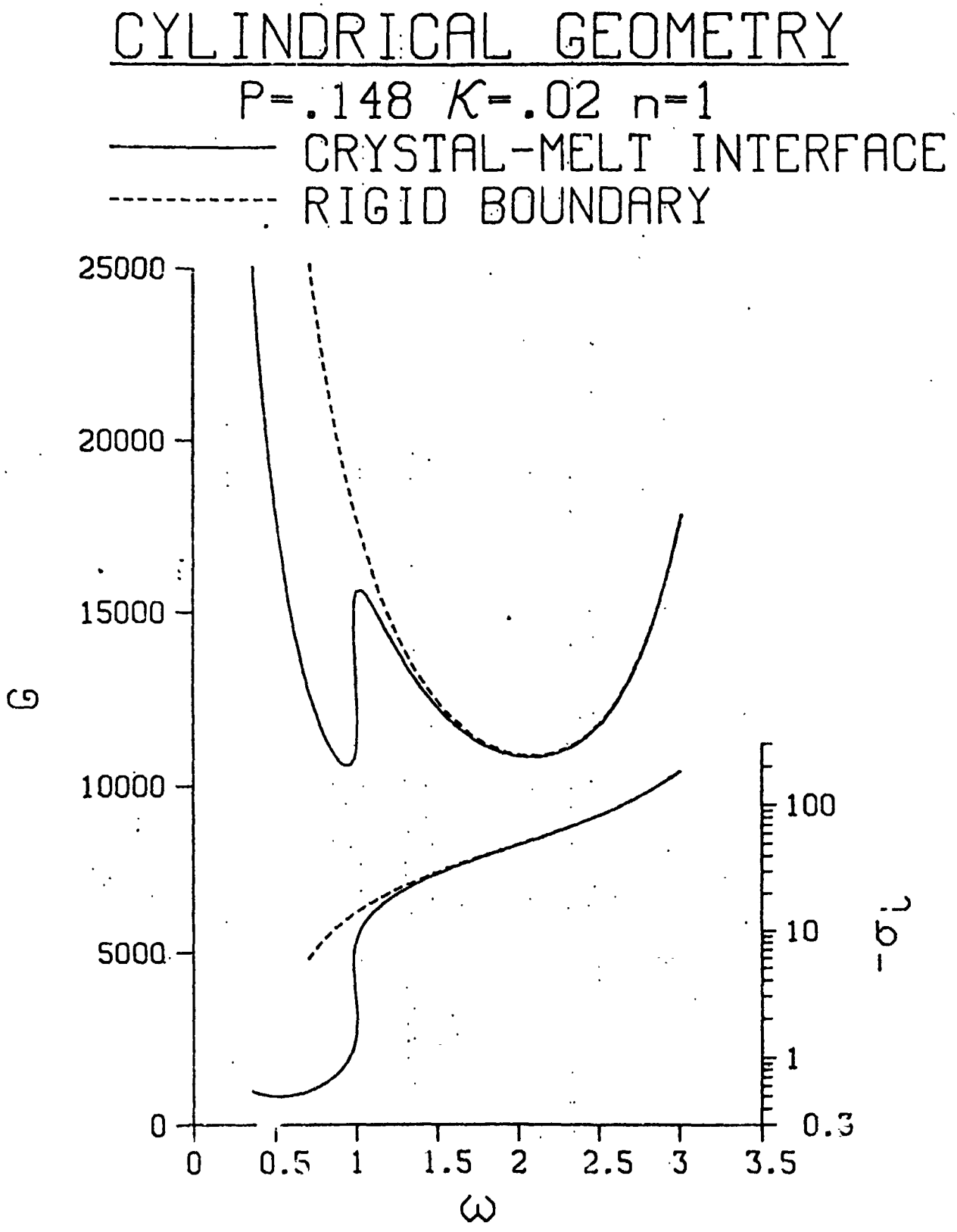
CYLINDRICAL GEOMETRY
P=.148 K=.02 n=1
CRYSTAL-MELT INTERFACE
RIGID BOUNDARY
25000
20000
15000
10000
5000
0
G
0
0.5
1
1.5
2
2.5
3
3.5
ω
100
10
1
0.3
-G'

Figure 4

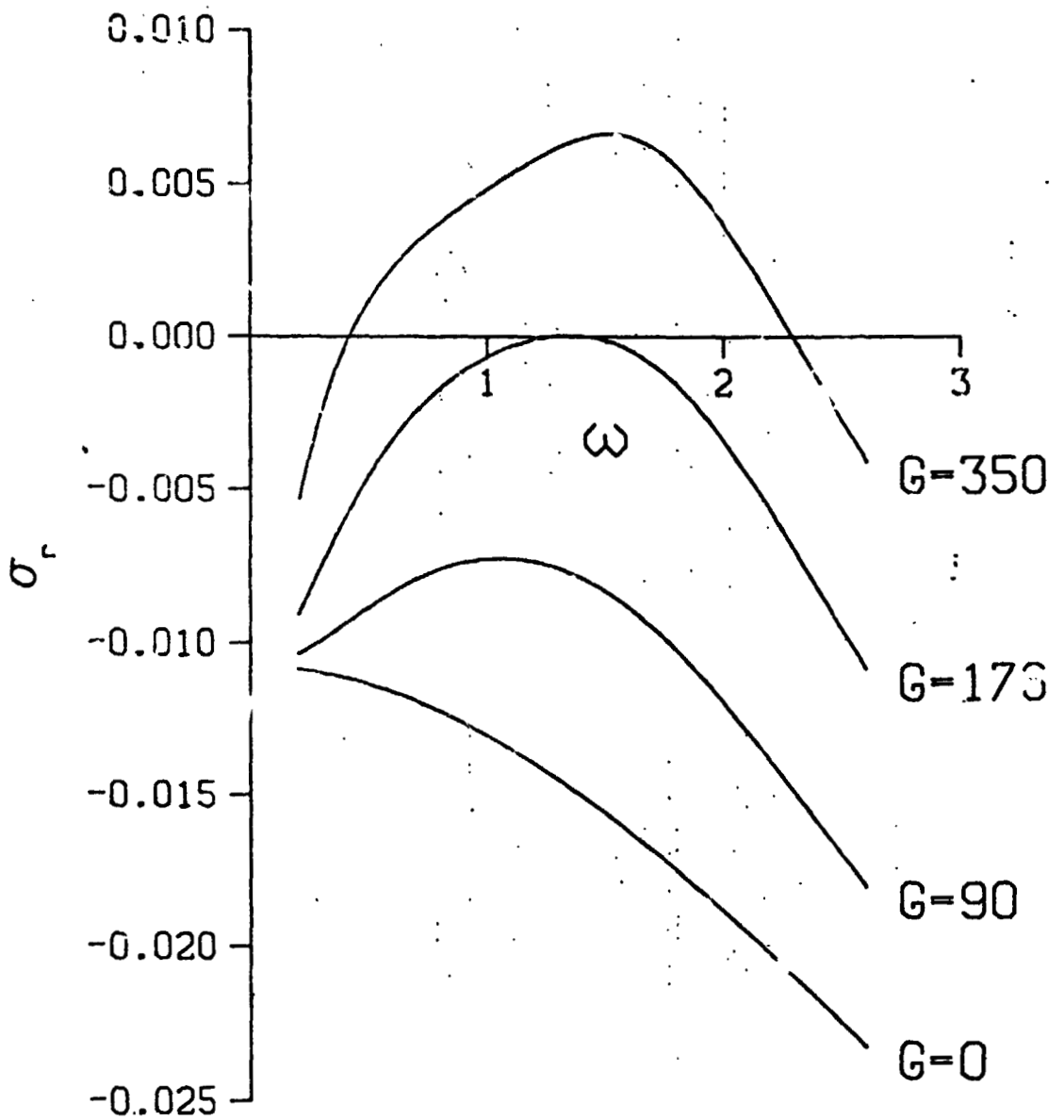
CYLINDRICAL GEOMETRY
CRYSTAL-MELT INTERFACE
P=22.8 K=0.02 n=1
0.010
0.005
0.000
-0.005
-0.010
-0.015
-0.020
-0.025
1
2
3
ω
σr
G=350
G=173
G=90
G=0

Figure 5

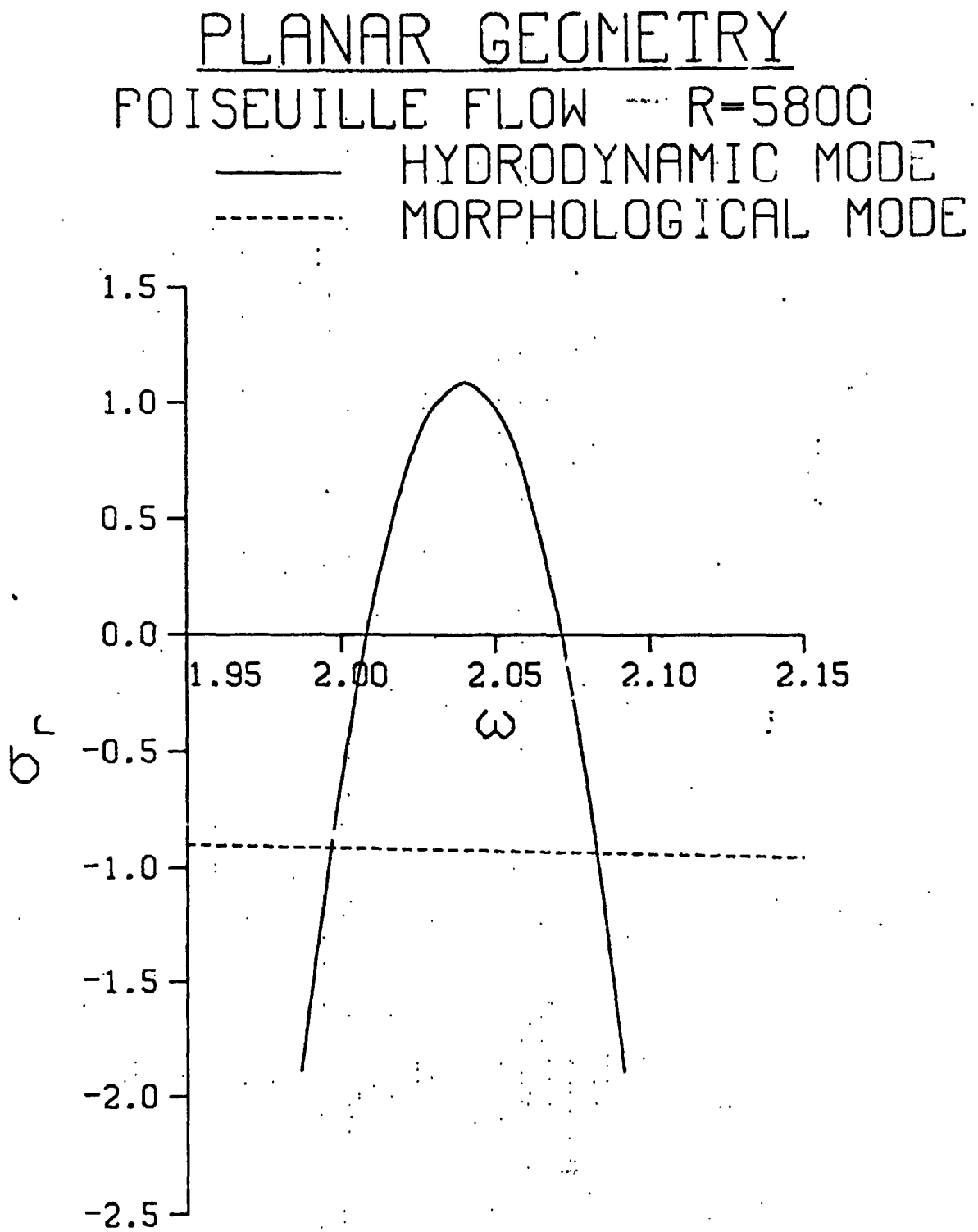
PLANAR GEOMETRY
POISEUILLE FLOW --- R=5800
HYDRODYNAMIC MODE
MORPHOLOGICAL MODE
1.5
1.0
0.5
0.0
-0.5
-1.0
-1.5
-2.0
-2.5
1.95
2.00
2.05
2.10
2.15
ω
σ^L

Figure 6

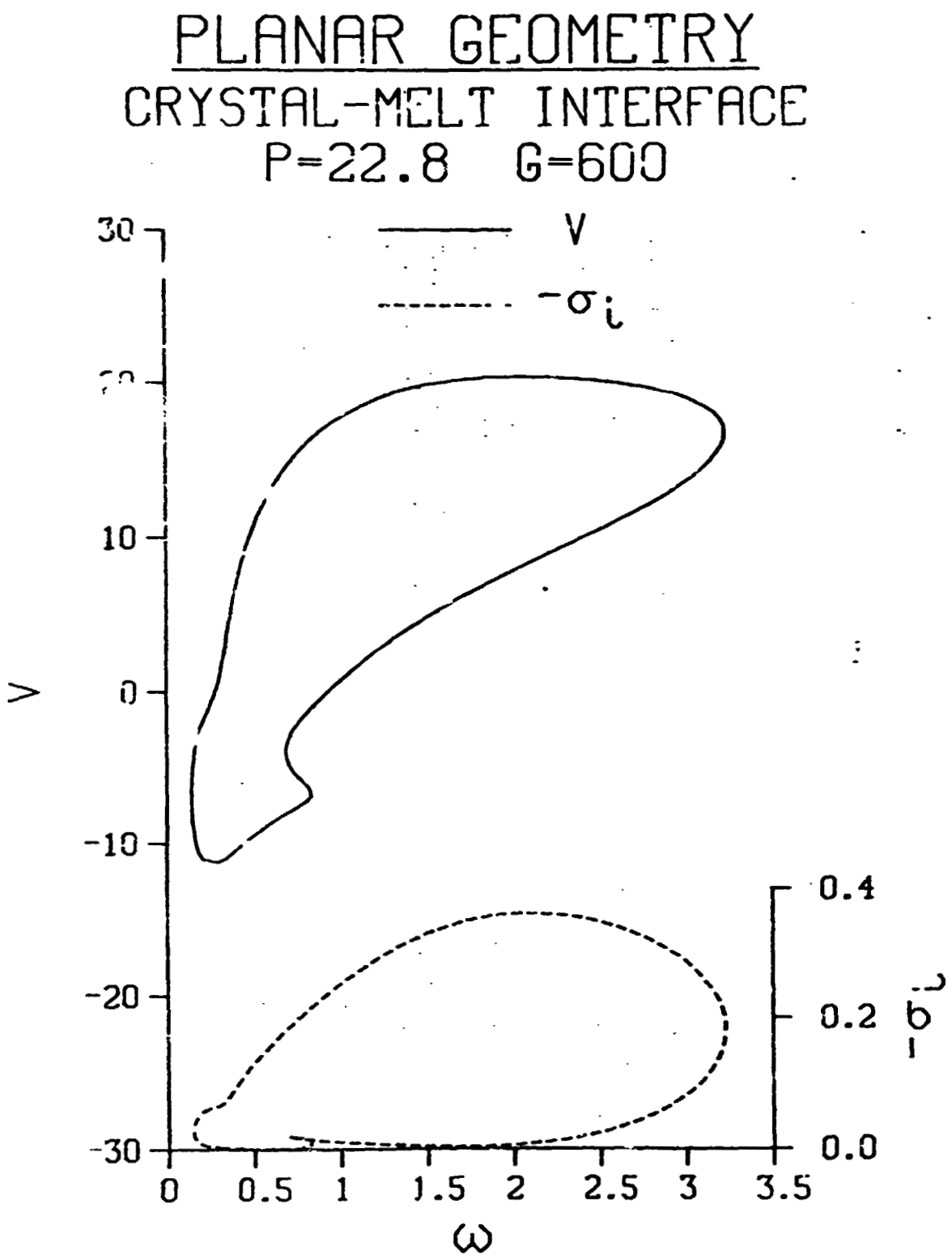
PLANAR GEOMETRY
CRYSTAL-MELT INTERFACE
P=22.8 G=600
V
$-\sigma_i$
30
10
0
-10
-20
-30
V
0.4
0.2
0.0
b_i
0
0.5
1
1.5
2
2.5
3
3.5
ω

Figure 7

APPENDIX C

Effect of a Forced Couette Flow on Coupled Convective and Morphological Instabilities During Unidirectional Solidification

S. R. Coriell, G. B. McFadden, R. F. Boisvert

National Bureau of Standards
Washington, D.C. 20234

and

R. F. Sekerka*

Carnegie-Mellon University
Pittsburgh, PA 15213

*Consultant, National Bureau of Standards

ABSTRACT

The effect of a forced Couette flow, parallel to a horizontal crystal-melt interface during directional solidification of an alloy of lead containing tin, on the onset of convective and morphological instabilities is calculated numerically via a linear stability analysis Such a flow does not affect perturbations with wave vectors perpendicular to the flow. The onset of morphological instability is somewhat suppressed and thermosolutal convection is greatly suppressed. When instabilities occur, they are oscillatory and correspond to travelling waves. For values of the crystal growth velocity for which mixed morphological and convective modes occur, the presence of a forced flow produces sufficient decoupling to allow formerly degenerate branches to be identified.

1. INTRODUCTION

The onset of natural convection and morphological instability during vertical directional solidification of a binary alloy has been calculated previously by linear stability analysis [1-6]. For given growth conditions, it is well known that the crystal-melt interface is morphologically unstable in the presence of sufficiently large solute concentrations [7]. For growth vertically upwards toward a hotter fluid whose density decreases with increasing temperature, and in the absence of horizontal gradients, the fluid is convectively unstable (thermosolutal convection) for solute concentrations above some critical value provided that a solute which is rejected at the crystal-melt interface is less dense than the bulk melt or a solute that is preferentially incorporated at the crystal-melt interface is more dense than the bulk melt. It is well known that such thermosolutal convection can occur even if the unperturbed fluid density decreases with height [8] because of the different rates at which heat and solute diffuse. For the solidification of lead containing tin with a temperature gradient in the melt of 200 K/cm, it was found [1] that the mode of instability at onset corresponds to thermosolutal convection for growth velocities less than about 40 μm/s and to morphological instability above this velocity. In the vicinity of this transition velocity, there are mixed modes that involve complex interaction between convective and morphological instabilities.

Delves [9-11] has calculated the effect on morphological stability of a forced flow parallel to the unperturbed crystal-melt interface. Such a flow has no effect on interface shape perturbations with wave vector perpendicular to the direction of the flow, but usually increases the

critical concentration for morphological instability, and gives rise to traveling waves, for perturbations with wave vector parallel to the direction of the flow. Similarly, it is known that a Couette shear flow stabilizes perturbations with wave vector parallel to the direction of flow for Rayleigh-Benard convection, i.e., a pure liquid heated from below [12-14] and for thermosolutal convection with linear solute and temperature fields [15].

In this article we report numerical results for the effect of a forced fluid velocity, parallel to the crystal-melt interface and varying linearly with distance from the interface (Couette flow), on the onset of convective and morphological instabilities during the directional solidification of lead containing tin. Since perturbations with wave vector perpendicular to the flow direction are unaffected by the flow, the results obtained here are for perturbations with wave vector parallel to the direction of flow. Our results extend those of Delves to include thermosolutal convection and extend our previous work on thermosolutal convection to include a forced flow. When a forced flow is included, the instability is oscillatory and corresponds to traveling waves. In general, we find that the forced flow stabilizes perturbations with wave vector parallel to the flow in the sense that the critical concentration for their instability is larger than in the absence of such flow. However, unless perturbations with wave vector perpendicular to the flow are absent or can be otherwise suppressed, the onset of instability will occur at the same concentration as in the absence of forced flow but will correspond to two-dimensional rolls with the axes of the rolls parallel to the flow direction.

2. THEORY

We consider unidirectional solidification at constant velocity V in the vertical direction of a binary alloy with an initially planar interface. We choose a moving coordinate system (x, y, z) attached to this planar crystal-melt interface located at z = 0 with the z-axis directed into the melt and antiparallel to the gravitational acceleration. The basic equations and boundary conditions governing the convective and morphological stability of this system have been derived previously [1,3] and will simply be stated here. The fluid velocity $\underset{\sim}{U}'$, the temperature T', the concentration C', and the crystal-melt interface shape z_{SL} may be expressed in the form

$$\underset{\sim}{U}' = \underset{\sim}{U}_0(z) + \underset{\sim}{U}(z)\, F(x, y, t),$$

$$T' = T_0(z) + T(z)\, F(x, y, t),$$

$$C' = C_0(z) + C(z)\, F(x, y, t),$$

$$z_{SL} = \delta\, F(x, y, t),$$

where the subscript o indicates the unperturbed fields which are functions of z alone, δ is the initial amplitude of the perturbed interface, $\underset{\sim}{U}$, T and C express the dependence of the perturbed fluid velocity, temperature, and concentration, on z and $F(x, y, t) = \exp[\sigma t + i(\omega_x x + \omega_y y)]$. The complex number σ governs the dependence on time t of the perturbed fields, and ω_x and ω_y are spatial frequencies. The system is unstable if the real part of σ is positive for any values of ω_x and ω_y. The unperturbed temperature and concentration fields depend exponentially on z. The unperturbed flow field is of the form $\underset{\sim}{U}_0(z) = \underset{\sim}{i}q(z) - \underset{\sim}{k}\varepsilon V$, with $\varepsilon = (\rho_S/\rho_L) - 1$, where ρ_S and ρ_L are densities of crystal and melt, respectively; we measure fluid velocities in the laboratory

frame. The function q represents a forced flow in the x-direction parallel to the unperturbed crystal-melt interface; we shall later take q to be linear in z in our calculations.

The linearized differential equations that govern stability are

$$\{L[\nu L + V^*(d/dz) - \sigma] - i\omega_x(qL - d^2q/dz^2)\}W = g\omega^2(\alpha T + \alpha_C C),$$

$$\{\kappa L + V^*(d/dz) - \sigma - i\omega_x q\}T = (dT_0/dz)W,$$

$$\{DL + V^*(d/dz) - \sigma - i\omega_x q\}C = (dC_0/dz)W, \qquad (2)$$

where W is the z-component of $\underset{\sim}{U}$, ν is the kinematic viscosity, $V^* = (1 + \varepsilon)V$, $L = (d^2/dz^2 - \omega^2)$, $\omega^2 = (\omega_x^2 + \omega_y^2)$, g is the magnitude of the gravitational acceleration, α and α_C are coefficients used to express the change in fluid density ρ from a reference density ρ_0, viz., $\rho = \rho_0[1 - \alpha T' - \alpha_C C']$, κ is the thermal diffusivity and D is the diffusion coefficient. The unperturbed temperature and concentration gradients are

$$(dT_0/dz) = G_L \exp(-V^*z/\kappa)$$

and

$$(dC_0/dz) = G_C \exp(-V^*z/D),$$

where G_L and G_C are the temperature and concentration gradients at the unperturbed crystal-melt interface $z = 0$.

The linearized boundary conditions at $z = 0$ are [1, 3]

$$W = -\varepsilon\sigma\delta,$$

$$(dW/dz) = [\varepsilon\omega^2 + i\omega_x(dq/dz)]\delta,$$

$$k_S\omega_S T - k_L(dT/dz) = \delta\{\sigma L_v - (V^*k_L G_L/\kappa) + (Vk_S G_S/\kappa_S) - k_S\omega_S(G_L - G_S)\},$$

$$VC + (D/[(1 + \varepsilon)(1 - k)])(dC/dz) = -\delta\{[VG_C k/(k - 1)] + c_\omega\sigma/k\},$$

$$mC - T = \delta\{G_L - mG_C + T_m\Gamma\omega^2\}, \qquad (3)$$

where k_L and k_S are the thermal conductivities of the melt and crystal, respectively, κ_S is the thermal diffusivity of the crystal,

$\omega_S = -(V/2\kappa_S) + [(V/2\kappa_S)^2 + \omega^2 + \sigma/\kappa_S]^{1/2}$, L_V is the latent heat per unit volume of the crystal, $G_S = (VL_V + k_L G_L)/k_S$, k is the distribution coefficient, c_∞ is the solute concentration far from the interface, $G_C = V^* c_\infty (k - 1)/(Dk)$, m is the liquidus slope, T_M is the melting point of the pure crystal with a planar interface, and Γ is a capillary constant, i.e., the ratio of the crystal-melt surface tension and L_V. The initial interface amplitude δ can be eliminated from eq. (3) to obtain four boundary conditions involving only W, T and C.

The boundary conditions far from the interface at $z = z_L$ are

$$W = (dW/dz) = (dT/dz) = C = 0. \tag{4}$$

As long as z_L is sufficiently large, the numerical results with (dq/dz) constant are independent of z_L and independent of whether Dirichlet or Neumann boundary conditions are specified for the perturbed temperature and concentration fields.

It is apparent from the differential equations and boundary conditions that q and its derivatives appear only when multiplied by ω_x. Therefore, defining θ such that $\omega_x = \omega \cos \theta$ and $\omega_y = \omega \sin \theta$, the solution depends only on ω and q cos θ. Without any loss of generality, we take $\theta = 0$ in our calculations since results for other values of θ can be obtained by replacing q by q cos θ. Clearly, if $\theta = \pi/2$, i.e., $\omega_x = 0$, the imposed flow field has no effect on the critical concentration for the onset of instability.

The numerical methods have been described previously [1]. The differential equations are rewritten as a set of 16 real first order equations. They are solved by using the software SUPORT [16] developed for linear boundary value problems. We set σ_r, the real

part of σ, equal to zero and iterate on c_∞ and σ_i, the imaginary part of σ, using the non-linear equation solver SNSQE [17-18], until we find a solution of the differential equations that satisfies the boundary conditions. In addition to the tests of the code described previously [1], we have reproduced results of Gersting and Jankowski [19] for the Orr-Sommerfeld equation and of Gallagher and Mercer [14] for Rayleigh-Benard convection with shear.

3. RESULTS

Numerical calculations have been carried out for lead containing tin for crystal growth velocities of 2, 40, and 200 μm/s with G_L = 200K/cm, $\omega_y = 0$, and $\varepsilon = 0$. The properties of the lead-tin system used in the calculations are given in Table 1 of reference 1. We take $q(z) = Sz$, where the constant S determines the amount of shear in the forced flow field.

We first give results for a relatively low growth velocity (V = 2 μm/s) for which the mode of instability at onset corresponds to thermosolutal convection [1]. Then we turn to a relatively high velocity (V = 200 μm/s) for which the mode is morphological. Finally, we consider an intermediate velocity at which mixed modes prevail.

For V = 2 μm/s, the mode of instability at onset is thermosolutal convection which occurs at a bulk concentration $c_\infty = 3.615(10^{-4})$ wt.% for S = 0, i.e., for the absence of forced convection. In the absence of all convection, morphological instability would not occur until $c_\infty = 3.899$ wt.%. We characterize the amount of shear, S, of the forced flow field by the effective velocity SD/V which is the value of q at a distance D/V into the liquid. The effects of shear on the critical concentration, wavelength, $2\pi/\omega$, and wave speed, $-\sigma_i/\omega$, at the onset of instability are

shown in Figures 1-3, respectively. The critical concentration and wave speed increase with increasing shear. The wavelength decreases, reaches a minimum, and then slowly increases as the shear increases. For SD/V = 0.087 cm/s, the critical concentration is about 100 times that for no forced flow. The wave speed is comparable to SD/V and is about 350 times the crystal growth velocity for SD/V = 0.087 cm/s.

For V = 200 μm/s, the mode of instability is morphological and occurs at a bulk concentration of 0.0554 wt.% for S = 0. For this case, an overstable convective mode [5] does not occur until $c_\infty \equiv 3.7$ wt.%. The critical concentration, wavelength, and wave speed as a function of SD/V are shown in Figures 4-6, respectively. As SD/V increases, the critical concentration and wave speed increase while the wavelength decreases. Extremely large shear is required to increase the critical concentration, e.g., S = 10^3 s^{-1} (which corresponds to SD/V = 1.5 cm/s) increases the critical concentration by about 50%. For SD/V = 1.5 cm/s, the wave speed of $6.5(10^{-3})$ cm/s is about one third the crystal growth velocity. The magnitude of the shear required to increase the critical concentration for morphological stability is in general agreement with the calculations of Delves [11] for gallium-doped germanium.

At a crystal growth velocity of 40 μm/s, the onset of convective and morphological instability occur at about the same concentration, and the mode of instability (see Fig. 1 of reference 1 and Figs. 2-4 of reference 3) is mixed. The effect of shear on this instability is shown in Figures 7-9 for S = 10^{-2}, 10^{-1}, and 1 s^{-1}, respectively. The critical concentration and σ_i are plotted as functions of the spatial frequency ω. The onset of instability occurs at the minimum value of

c_∞ as a function of ω. We identify the minimum at larger values of ω with morphological instability (dashed curves) and the minimum at smaller values of ω with convective instability (solid curves). For $S = 0.01\ s^{-1}$, the curves are similar to the $S = 0$ curves (Fig. 3 of reference 3). For finite S, σ_i is generally non-zero, while for $S = 0$, σ_i vanishes identically for a range of ω values. As S increases, the convective and morphological modes appear to decouple. For $S = 1\ s^{-1}$, the concentration curves appear to cross each other with little interaction; however, σ_i of the morphological mode changes sign near the crossing point. In Fig. 7, the minimum of the convective branch occurs at a smaller value of c_∞ than in Fig. 9; the minima in the morphological branches occur at essentially the same value of c_∞.

DISCUSSION

Extension of our previous work on coupled convective and morphological instabilities to include a forced flow parallel to the interface affects perturbations with wave vectors along the forced flow in the following ways: (1) the onset of morphological instability is somewhat suppressed and the onset of thermosolutal convection is greatly suppressed; (2) the resulting instabilities are oscillatory and correspond to travelling waves; (3) for values of the growth velocity for which mixed morphological and convective modes occur, the presence of a forced flow produces sufficient decoupling to allow formerly degenerate branches to be identified. Roughly speaking, a forced flow tends to smooth inhomogeneities in the temperature, concentration, and flow fields, along the direction of the flow, that would otherwise form spontaneously and lead to instabilities.

It should be emphasized that the above results were calculated for the case of a very simple flow velocity $q = Sz$ (Couette flow) which is known to be hydrodynamically stable to infinitesimal disturbances for all values of S [20]. Other flows that can be hydrodynamically unstable, such as those recently investigated [21], can lead to strong destabilizing interactions between convective and morphological modes, even though the flow field near the interface itself could be approximated by Couette flow. Flows with shear rates comparable to those found to be significant in the present paper have been produced during eutectic solidification by rotation of the crystal [22]. Other flows related to horizontal temperature gradients have been calculated by Chang and Brown [23] and shear rates at the interface can be calculated from such flows. These flows are, however, much more complex than the simple Couette flow treated here and great caution should be excercised in the application of our results to such situations.

Acknowledgements

This work was partially sponsored by the Microgravity Sciences Program of the National Aeronautics and Space Administration. One of us (R. F. Sekerka) received partial support from the National Science Foundation under grant DMR78-22462. We would like to thank R. A. Brown, R. G. Rehm and R. J. Schaefer for helpful discussions.

REFERENCES

1. S. R. Coriell, M. R. Cordes, W. J. Boettinger, and R. F. Sekerka, J. Crystal Growth 49 (1980) 13.

2. S. R. Coriell, M. R. Cordes, W. J. Boettinger, and R. F. Sekerka, Adv. Space Res 1 (1981) 5.

3. S. R. Coriell and R. F. Sekerka, PhysicoChemical Hydrodynamics 2 (1981) 281.

4. R. J. Schaefer and S. R. Coriell, in: Materials Processing in the Reduced Gravity Environment of Space, Ed. G. E. Rindone (North-Holland, Amsterdam, 1982) p. 479.

5. D. T. J. Hurle, E. Jakeman, and A. A. Wheeler, J. Crystal Growth 58 (1982) 163.

6. D. T. J. Hurle, E. Jakeman, and A. A. Wheeler, Phys. Fluids 26 (1983) 624.

7. W. W. Mullins and R. F. Sekerka, J. Appl. Phys 35 (1964) 444.

8. J. S. Turner, Buoyancy Effects in Fluids (Cambridge Univ. Press, London, 1973).

9. R. T. Delves, J. Crystal Growth 3/4 (1968) 562.

10. R. T. Delves, J. Crystal Growth 8 (1971) 13.

11. R. T. Delves, in: Crystal Growth, Vol. 1, Ed. B. R. Pamplin (Pergamon, Oxford 1974) p. 40.

12. G. Z. Gershuni and E. M. Zhukhovitskii, Convective Stability of Incompressible Fluids (Keter, Jerusalem, 1976).

13. J. W. Deardorff, Phys. Fluids 8 (1965) 1027.

14. A. P. Gallagher and A. McD. Mercer, Proc. Roy. Soc. A286 (1965) 117.

15. P. F. Linden, Geophys. Fluid Dyn. 6 (1974) 1.

16. M. R. Scott and H. A. Watts, SIAM J. Numerical Anal. 14 (1977) 40.

17. SLATEC Common Math Library, National Energy Software Center, Argonne National Lab., Argonne, IL. The program SNSQE was written by K. L. Hiebert and is based on an algorithm of Powell.

18. M. J. D. Powell, in: Numerical Methods for Nonlinear Algebraic Equations, Ed. P. Rabinowitz (Gordon and Breach, New York 1970) p. 87.

19. J. M. Gersting, Jr. and D. R. Jankowski, Int. J. Num. Methods Eng. 4 (1975) 195.

20. P. G. Drazin and W. H. Reid, Hydrodynamic Stability (Cambridge Univ. Press, London, 1981).

21. S. R. Coriell, R. F. Boisvert, J. I. Mickalonis, and M. E. Glicksman, Adv. Space Research 3, No. 5 (1983) 95.

22. J. M. Quenisset, R. Sokolowski, and M. E. Glicksman, J. Crystal Growth 63 (1983) 389.

23. C. J. Chang and R. A. Brown, J. Crystal Growth 63, (1983) 343.

FIGURE CAPTIONS

Fig. 1. The critical concentration c_∞ of tin in lead for the onset of thermosolutal convection as a function of SD/V for a growth velocity V of 2 μm/s and a temperature gradient G_L in the liquid of 200 K/cm.

Fig. 2. The wavelength $2\pi/\omega$ of sinusoidal perturbations at the onset of thermosolutal convection as a function of SD/V for conditions corresponding to those given in Fig. 1.

Fig. 3. The wave speed $(-\sigma_i/\omega)$ of sinusoidal perturbations at the onset of thermosolutal convection as a function of SD/V for conditions corresponding to those given in Fig. 1.

Fig. 4. The critical concentration c_∞ of tin in lead for the onset of morphological instability as a function of SD/V for a growth velocity V of 200 μm/s and a temperature gradient G_L in the liquid of 200 K/cm.

Fig. 5. The wavelength $2\pi/\omega$ of sinusoidal perturbations at the onset of morphological instability as a function of SD/V for conditions corresponding to those given in Fig. 4.

Fig. 6. The wave speed $(-\sigma_i/\omega)$ of sinusoidal perturbations at the onset of morphological instability as a function of SD/V for conditions correspond to those given in Fig. 4.

Fig. 7. The concentration c_∞ of tin in lead and σ_i at the onset of instability during directional solidification at V = 40 μm/s as a function of spatial frequency ω of a sinusoidal perturbation for a shear $S = 0.01\ s^{-1}$ and a temperature gradient G_L in the

liquid of 200 K/cm. The dashed curves correspond to morphological modes and the solid curves correspond to thermosolutal convection.

Fig. 8. The concentration c_∞ of tin in lead and σ_i at the onset of instability during directional solidification at V = 40 μm/s as a function of spatial frequency ω of a sinusoidal perturbation for a shear S = 0.1 s^{-1} and a temperature gradient G_L in the liquid of 200 K/cm. The dashed curves correspond to morphological modes and the solid curves correspond to thermosolutal convection.

Fig. 9. The concentration c_∞ of tin in lead and σ_i at the onset of instability during directional solidification at V = 40 μm/s as a function of spatial frequency ω of a sinusoidal perturbation for a shear S = 1.0 s^{-1} and a temperature gradient G_L in the liquid of 200 K/cm. The dashed curves correspond to morphological modes and the solid curves correspond to thermosolutal convection.

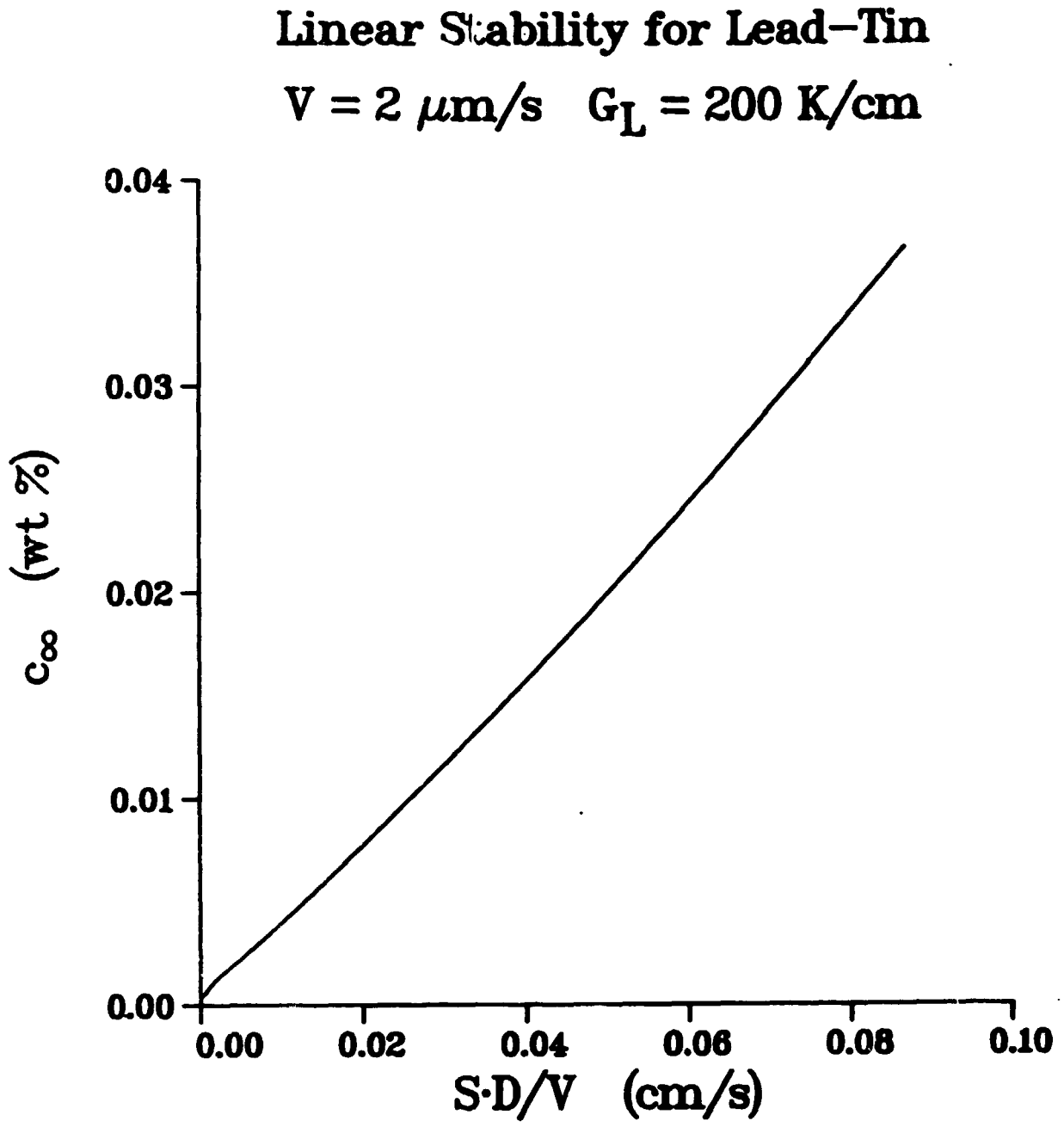
Linear Stability for Lead–Tin
V = 2 μm/s G_L = 200 K/cm
0.04
0.03
0.02
0.01
0.00
C∞ (wt %)
0.00
0.02
0.04
0.06
0.08
0.10
S·D/V (cm/s)

Linear Stability for Lead–Tin

$V = 2\ \mu m/s \quad G_L = 200\ K/cm$

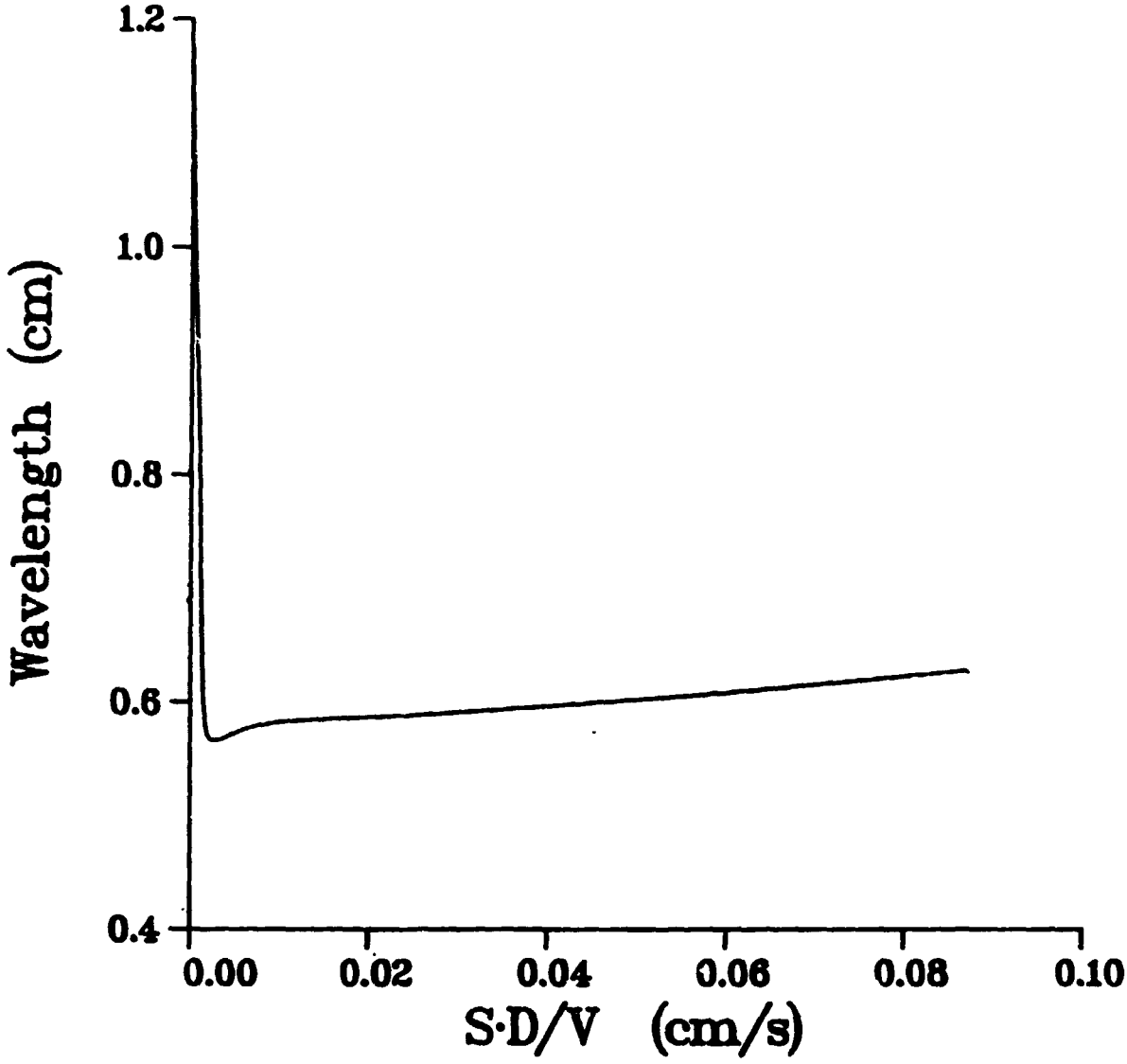

Linear Stability for Lead–Tin

$V = 2\ \mu m/s \quad G_L = 200\ K/cm$

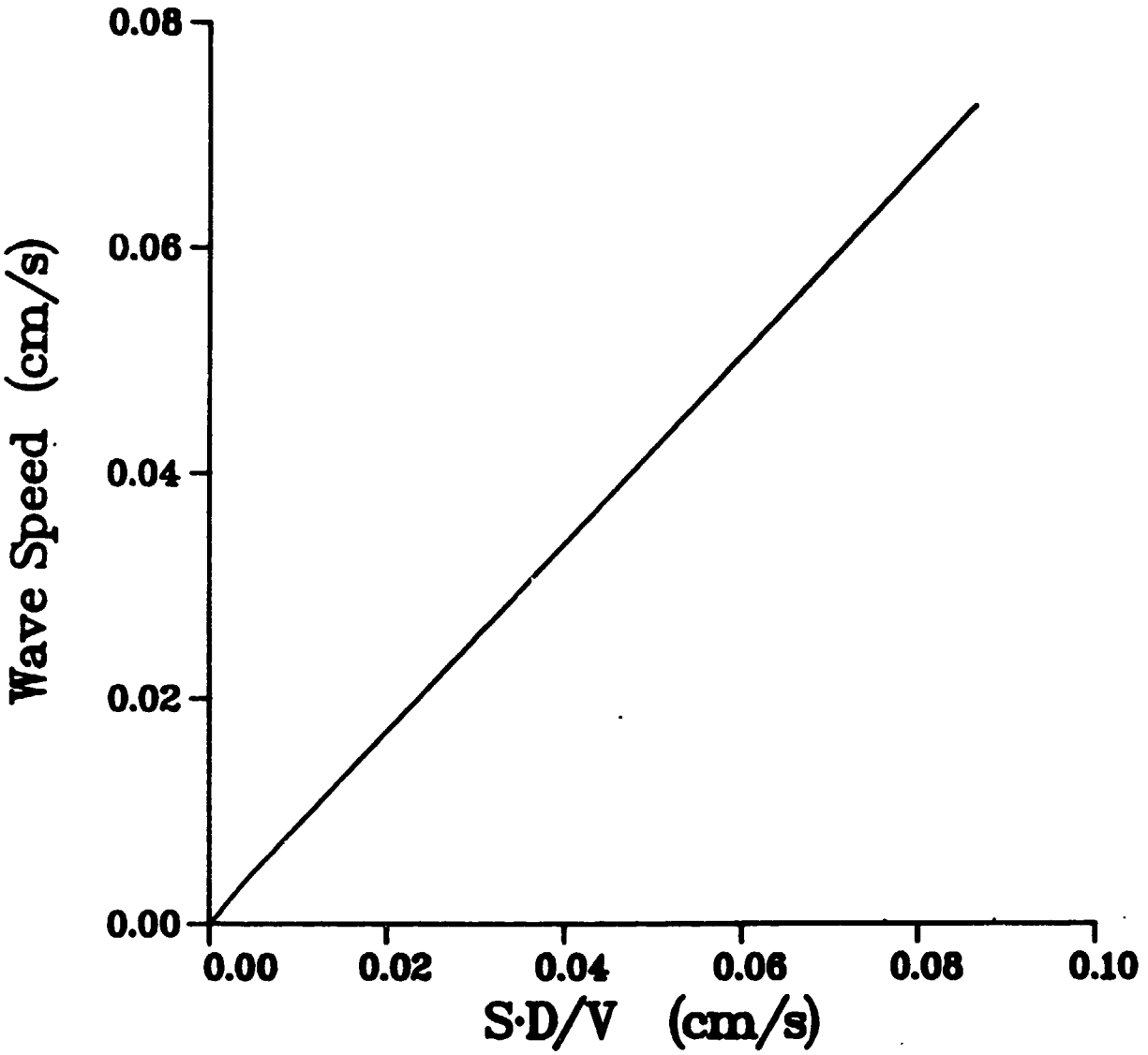

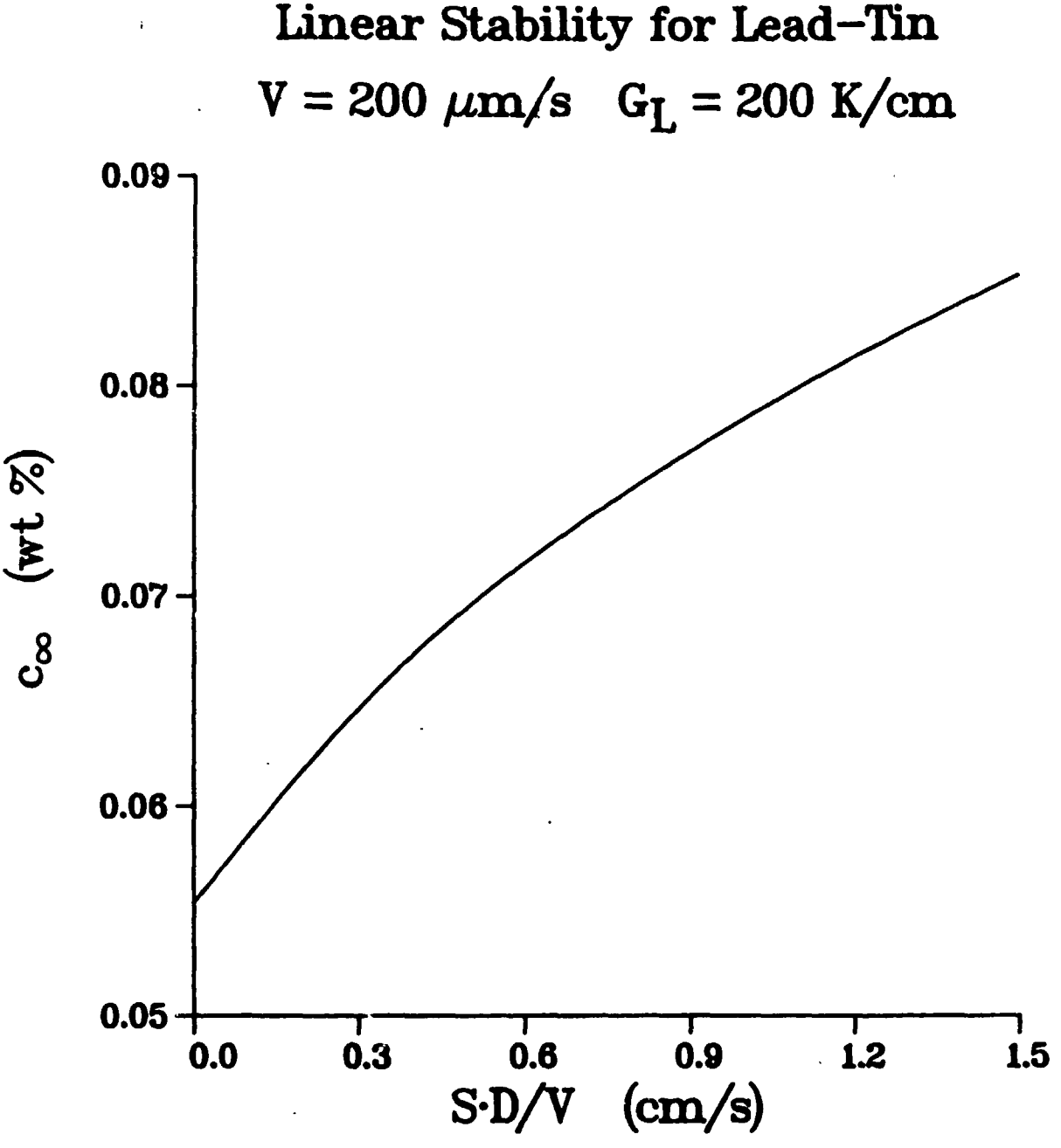
Linear Stability for Lead–Tin
V = 200 μm/s G_L = 200 K/cm
0.09
0.08
0.07
0.06
0.05
c∞ (wt %)
0.0
0.3
0.6
0.9
1.2
1.5
S·D/V (cm/s)

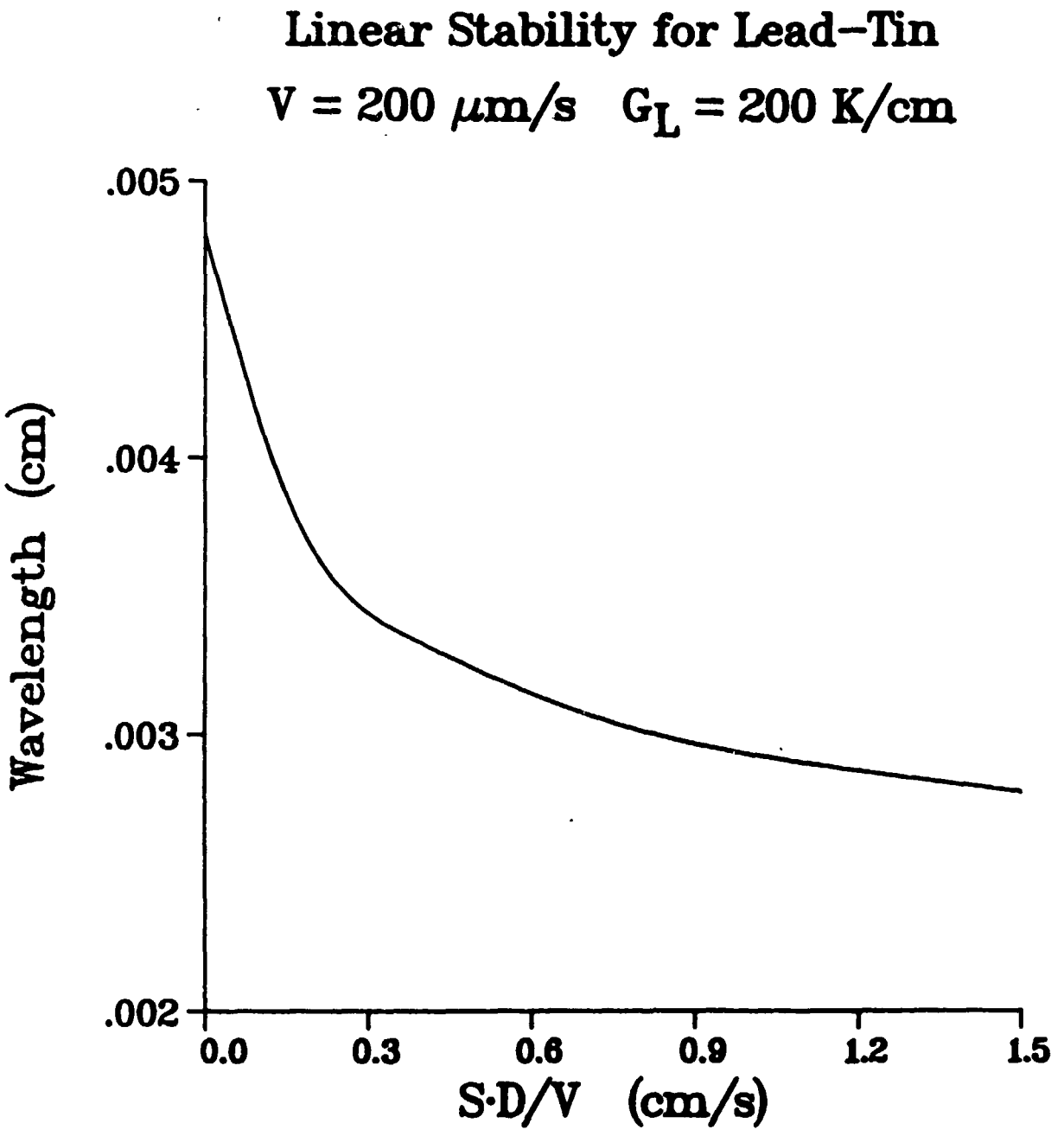
Linear Stability for Lead–Tin
V = 200 μm/s G_L = 200 K/cm
.005
.004
.003
.002
Wavelength (cm)
0.0
0.3
0.6
0.9
1.2
1.5
S·D/V (cm/s)

Linear Stability for Lead–Tin

$V = 200\ \mu m/s \quad G_L = 200\ K/cm$

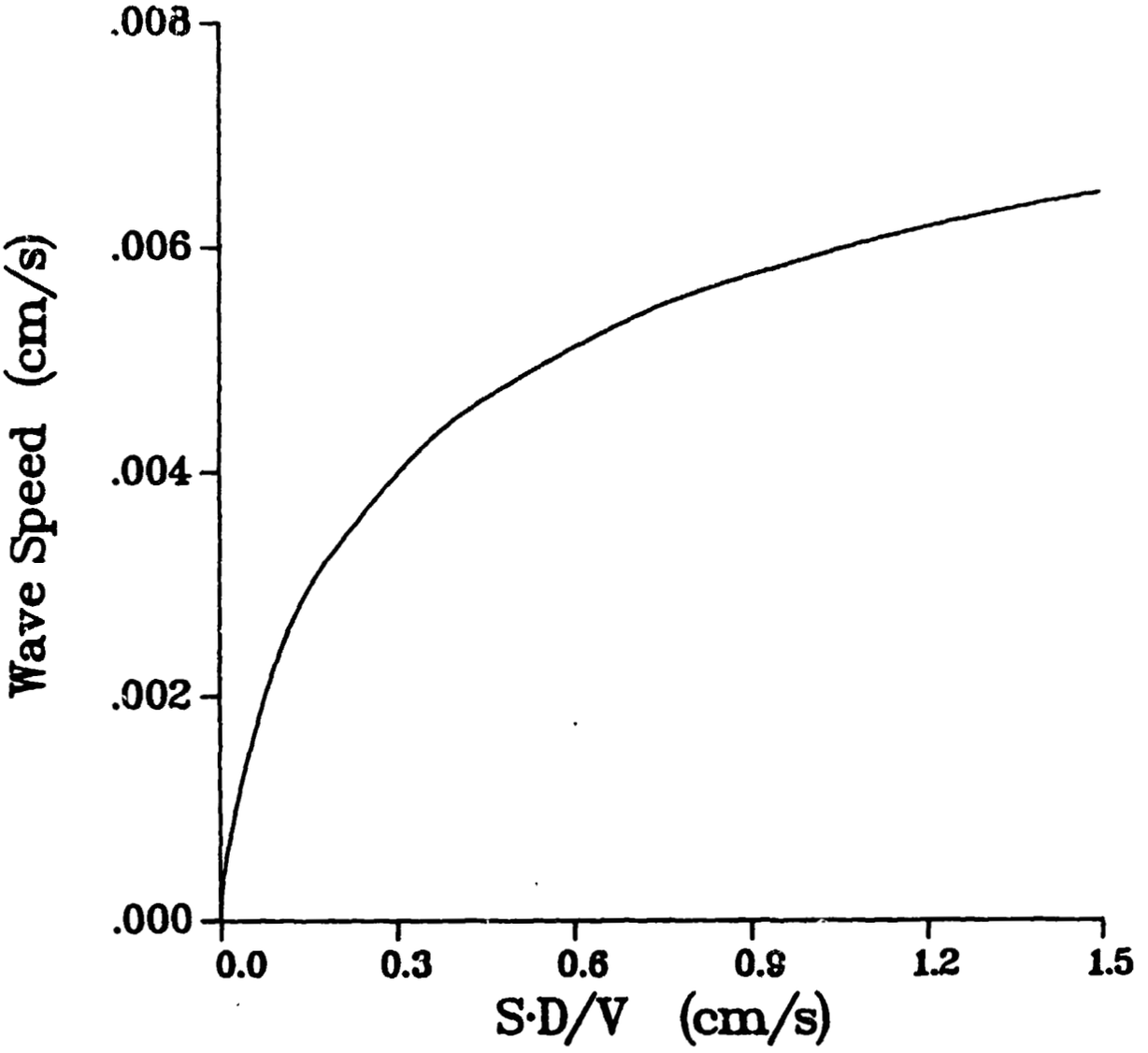

Linear Stability for Lead–Tin
V = 40 μm/s G_L = 200 K/cm
S = .01 s^{-1}

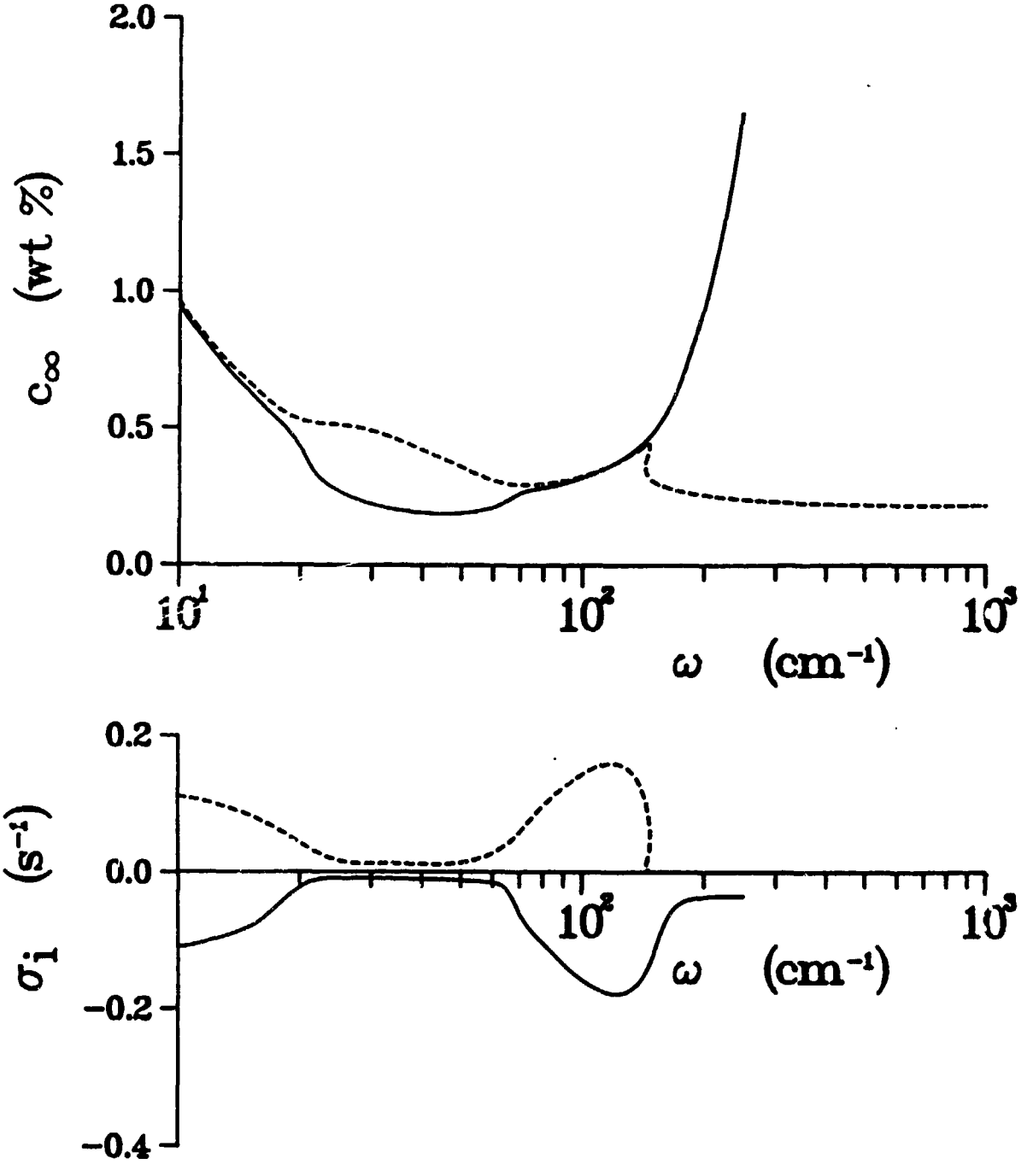

Linear Stability for Lead–Tin

$V = 40\ \mu m/s \quad G_L = 200\ K/cm$

$S = 0.1\ s^{-1}$

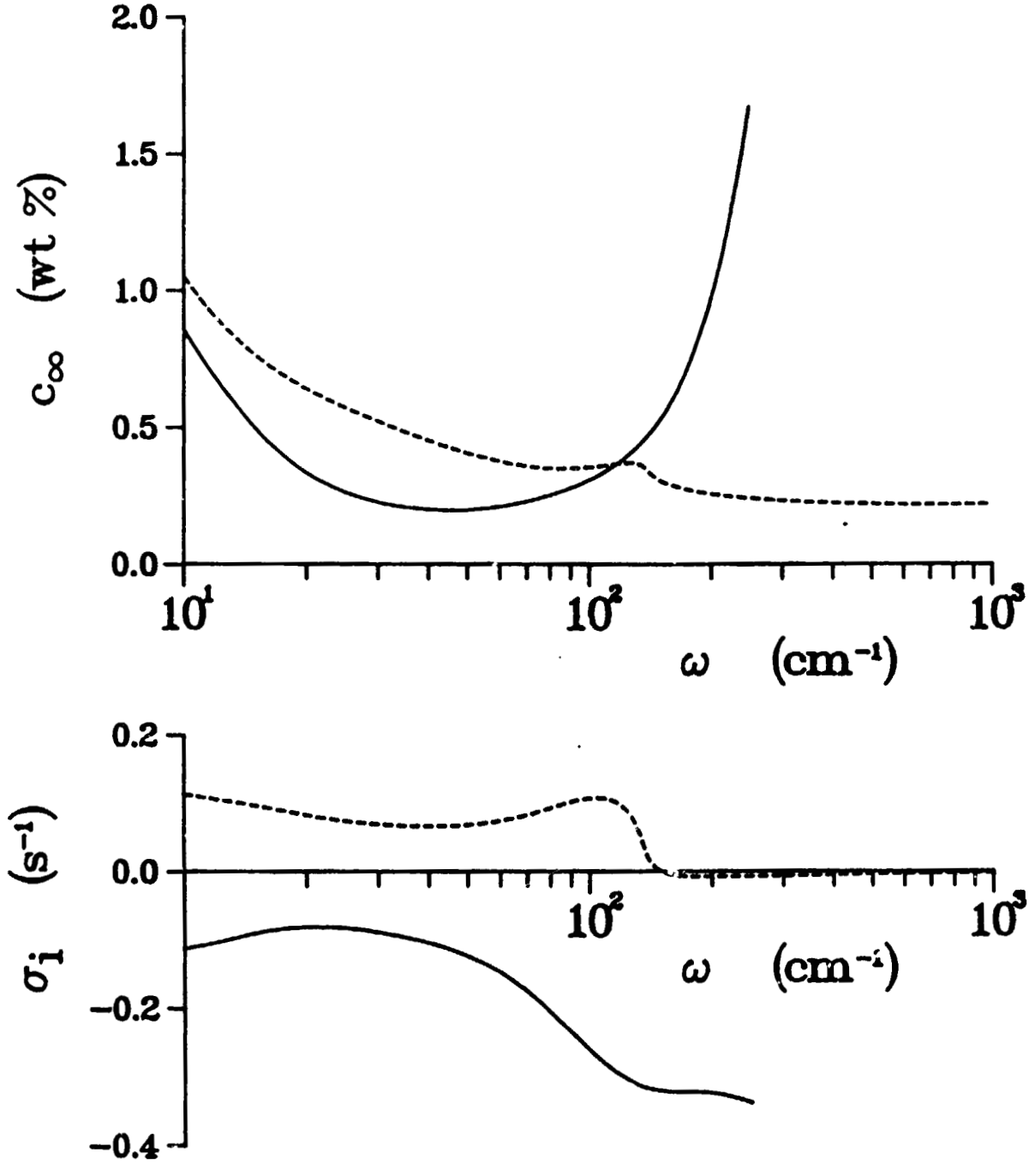

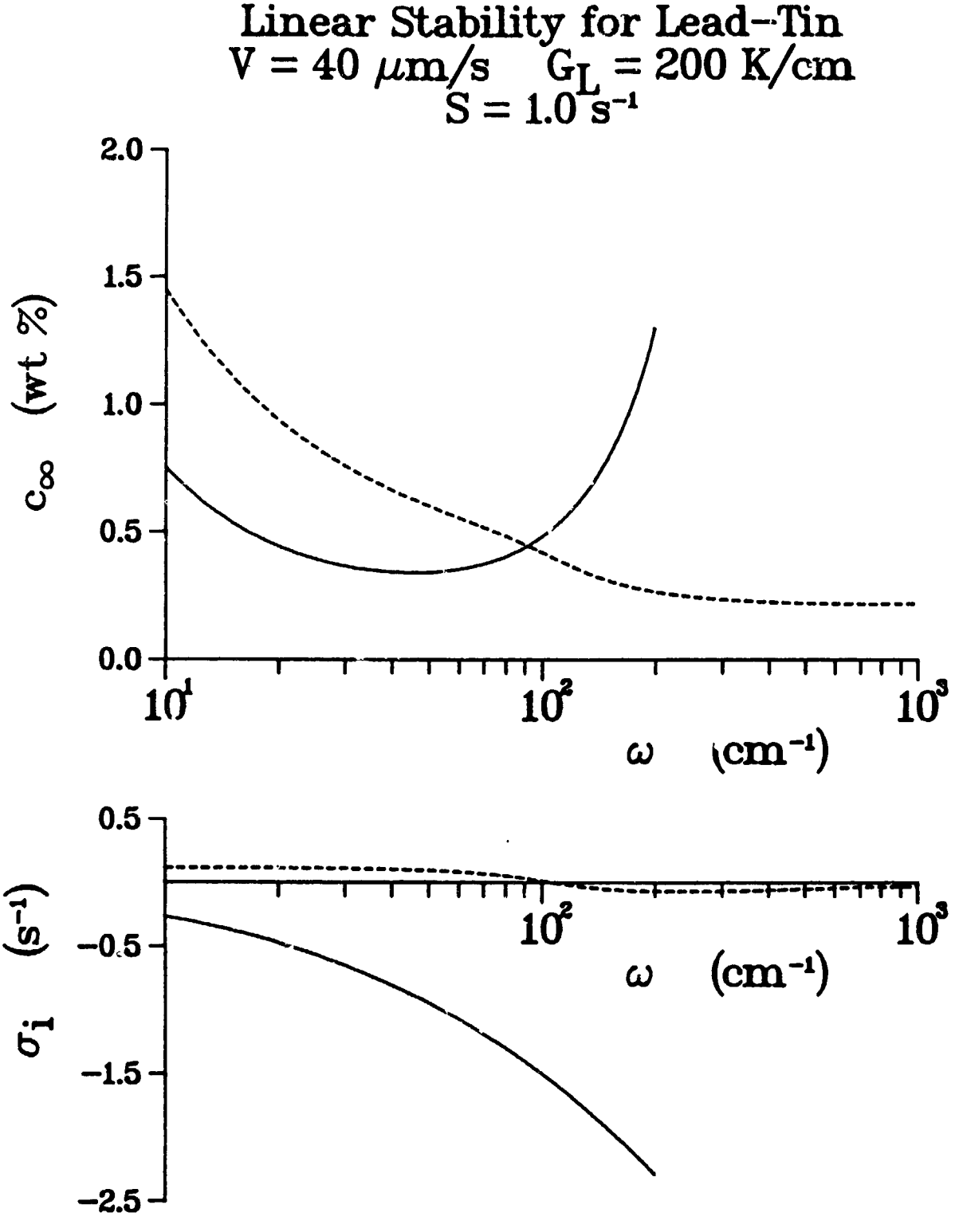
Linear Stability for Lead–Tin
V = 40 μm/s G_L = 200 K/cm
S = 1.0 s⁻¹
2.0
1.5
1.0
0.5
0.0
c∞ (wt %)
10¹
10²
10³
ω (cm⁻¹)
0.5
−0.5
−1.5
−2.5
σi (s⁻¹)
10²
10³
ω (cm⁻¹)

APPENDIX D

CONVECTION-INDUCED DISTORTION OF A SOLID-LIQUID INTERFACE

R. J. Schaefer and S. R. Coriell
Metallurgy Division
National Bureau of Standards
Washington, D.C. 20234

ABSTRACT

Measurements of convective flow fields and solid-liquid interface shapes during the solidification of a pure and a slightly alloyed transparent material reveal that the convective transport of solute can cause a macroscopic depression to develop in the solid-liquid interface. This effect occurs under conditions close to those which are predicted to produce morphological instability of a planar interface. A cellular or dendritic microstructure later develops within the interface depression. The convection is attributed to the effect of radial temperature gradients in the crystal growth apparatus.

I. INTRODUCTION

During unidirectional growth of a crystal by a Bridgeman or similar process, convection in the liquid phase can be driven be several forces. In the presence of gravitational forces, the most important source of convective flow is ordinarily the density differences due to temperature and composition differences within the sample. Additional flow can be driven by the volume change which accompanies the phase change, and if any free surfaces (liquid-vapor or liquid-liquid) are present, surface energy gradient (Marangoni) flows are possible. The latter two types of flow are present even in the absence of gravitational forces.

In the presence of gravitational forces, density-induced convective flow can be avoided during crystal growth if special conditions are met. In a pure material it is sufficient that the temperature increase with height (for a normal material which expands with increasing temperature) and that no gradients be present in the horizontal directions.

If a solute is present, the solidification process will lead to composition differences ahead of the solid-liquid interface. If the rejected solute is lower in density than the solvent, the composition differences can lead to a thermo-solutal convective instability. The conditions which lead to this instability are not simply that the density in some region increase with height: the conditions are determined by an analysis of the behavior of elements of the fluid which are displaced vertically [1, 2, 3].

When convective flow occurs, it redistributes both heat and solute in the liquid phase, and thus causes the temperature and concentration fields in this phase to differ from those which would be calculated on

the basis of diffusive transport alone. As a result, the composition of the crystal as it grows will be less homogeneous than would be possible in the absence of convection. A steady state flow pattern can result in lateral segregation while a non-steady flow pattern will produce additional longitudinal non-uniformity.

Because convective flow can modify the temperature and solute fields in the liquid adjacent to the solid-liquid interface, it can cause local variations in the conditions which determine the morphological stability [4] of the solid-liquid interface. Thus for example it can lead to the growth of crystals which contain localized regions of cellular microstructure within an otherwise cell-free matrix. When a highly uniform crystal is needed, it may thus be essential to keep these convective effects under control.

In this paper we present observations of convective phenomena during the solidification of a transparent "alloy" system, succinonitrile containing ethanol. The conditions which lead to the onset of thermo-solutal convective and interfacial (morphological) instabilities in this system are calculated, and other sources of convective flow are considered.

II. THEORY

The stability of the unidirectional upward solidification of succinonitrile containing ethanol, in the absence of horizontal temperature gradients, can be analyzed by the same methods previously used for the solidification of lead containing tin [1]. The material properties used in the calculations are listed in Table I: the measurement of some of these properties is described in the experimental section. The results of the calculations are qualitatively similar to those previously obtained

for the lead-tin system in that two types of instability are observed. Instabilities of short wavelength, which are associated with deviations of the solid-liquid interface from planarity, are termed interfacial instabilities. Instabilities of longer wavelength, which are associated with motion of the liquid above the interface, are termed convective instabilities. Figure 1 shows, as a function of the velocity of solidification, the concentration of ethanol in succinonitrile required to produce the two types of instability. The calculations apply to a system growing with a temperature gradient in the liquid of 10 K/cm, a typical value for this type of system.

The concentration of solute required to produce interfacial instabilities decreases with increasing velocity, as is the familiar situation described by the theory of morphological instability except at extremely high growth velocities. The convective instabilities show the opposite velocity dependence. Unidirectional upward solidification with a planar interface is stable at concentration-velocity combinations lying below both curves in Figure 1. At concentrations near 3×10^{-3} wt.% ethanol there exists a range of velocities in which the solidification is stable, above which interfacial instabilities are predicted and below which convective instabilities are predicted. At concentrations above 5.4×10^{-3} wt.% ethanol, growth is not stable at any velocity with this temperature gradient.

The dotted portion of the convective instability curve in Figure 1 represents an oscillatory convective instability which occurs in the region where the convective and interfacial instability curves cross. The onset of instability by an oscillatory mode is the most striking difference between the results for lead-tin and succinonitrile-ethanol.

Figure 2 shows the wavelength at the onset of instability relative to the diffusion boundary layer thickness D/V, for a temperature gradient in the liquid of 10 K/cm. Whereas the wavelength of the interfacial instabilities is approximately equal to the thickness of the diffusion layer, the wavelength of the convective instabilities is typically about an order of magnitude larger and at velocities of less than 1 μm/s the predicted wavelength of the convective instabilities are greater than 1 cm. Therefore one cannot expect to observe these instabilities in small containers.

Increasing the temperature gradient tends to stabilize the system with respect to both interfacial and convective instabilities. Figure 3 shows interfacial and convective stability curves for several values of the temperature gradient in the liquid. One of the samples used in this study contained 2.6×10^{-3} wt.% ethanol, as indicated in Figure 3, and it is seen that at this composition the gradient in the liquid has only a small effect on the velocity at which convective instability occurs, but has a strong effect on the velocity at which interfacial instability occurs.

In a real crystal growth process, horizontal temperature gradients are difficult to avoid. This is especially true for materials such as succinonitrile which have low thermal conductivities. In such cases the thermal conductivity of the container walls is comparable to that of the material under study, and the requirement of maintaining good visibility of the material in the solid-liquid interface region precludes the use of surrounding insulation.

Radial gradients resulting from lateral heat losses can be minimized

by careful design of the crystal growth system, but in the vicinity of the solid-liquid interface there is a thermal interaction with the chamber walls which cannot be completely eliminated. Conservation of heat at the interface leads to the relation

$$k_S G_S - k_l G_l = vL \qquad (1)$$

where k_S and k_l are the thermal conductivities of the solid and liquid, G_S and G_l are the temperature gradients in the solid and liquid, v is the growth velocity and L is the latent heat of fusion. In general there is therefore a velocity-dependent change of the temperature gradient across the interface. Because there is no corresponding change of gradient in the container walls, the isotherms in the vicinity of the container walls are distorted from the ideal horizontal planes which would be needed to avoid a driving force for convection.

In succinonitrile the thermal conductivity of the solid and liquid are almost identical, so that at zero growth velocity there is virtually no change in temperature gradient across the interface and it is possible to achieve almost planar interfaces. However, Eq. 1 indicates that there will be a gradient change of 2.1 K/cm at the interface for each 1 μm/s of growth velocity. As a result, at growth velocities of 1 μm/s or more there will be significant horizontal gradients near the container walls and thermally driven convective flow must be expected.

II. EXPERIMENT

Many of the properties of succinonitrile have been reported in the literature, as indicated in Table I. We have determined the relevant end of the succinonitrile-ethanol phase diagram (Figure 4) and find the liquidus and solidus slopes at low concentrations to be 3.6 K/wt.% and 81

K/wt.% respectively. In addition, we have measured the density of succinonitrile-rich liquids (Figure 4). The only property used in the calculations which has not actually been measured is the diffusion coefficient for ethanol in succinonitrile, for which an estimated value has been used.

Samples for crystal growth experiments were sealed under vacuum in borosilicate glass tubes, approximately 45 cm long and with 17 mm inside diameter. The compositior of the samples was evaluated from measurements of the solidus and liquidus temperatures. A high purity sample was found to have a melting range of 1.2×10^{-2} K, corresponding to the effect of 1.5×10^{-4} wt.% ethanol or equivalent impurity, while an ethanol-doped sample had a melting range of 0.215 K, corresponding to 2.6×10^{-3} wt.% ethanol.

For crystal growth the samples were drawn downwards by a tracking mechanism through a temperature gradient produced by a cooling water jacket and a small electric furnace. In the region between the water jacket and the furnace, the interface was surrounded by a transparent block with flat walls to reduce the optical distortion of the solid-liquid interface region (Figure 5). A flat auxiliary heater was embedded in this block to provide some control over the temperature gradients in the interface region.

Convection was measured from multiple-exposure photographs of latex microspheres floating in the liquid. The spheres were 10-20 μm in diameter and were close in density to the liquid succinonitrile so that they tended to settle out only at velocities much less than the convective flow velocities which were being measured. By using unequal intervals

between the multiple exposures, the direction of motion of individual particles could be determined. The particles were best seen in dark field illumination whereas bright field images showed the solid-liquid interface most clearly.

IV. RESULTS

When the sample is held stationary (zero growth velocity), any convection present in the liquid is attributable to the effect of radial heat losses. Stationary solid-liquid interfaces are observed to be slightly concave upwards, indicating that the temperature is higher in the center than around the edges. As expected under these circumstances, a convective flow pattern is present above the interface with flow downward near the walls, radially inward directly above the interface, and upwards in the center of the tube. The flow pattern above the interface can thus be described as a toroidal roll. Any thermal asymmetries of the system result in displacement of the node and axis of this torus from the central axis of the sample tube. If the asymmetry is sufficiently great, the torus pinches off to form a single transverse roll (Figure 6).

When the toroidal flow remains for several hours in a stationary sample, one frequently observes an accumulation of marker particles in the liquid just above the interface at the node where the radial inward flow converges and turns upward. A dense trail of particles streams upward with the liquid from this point and along the axis of the toroidal roll (Figure 7). The velocity of this upward flow near the center of the tube, at a distance 2.5 mm above the interface, is typically 10-15 μm/s. Smaller velocities could be attained when the interface region was well insulated but only at the cost of reduced visibility.

In a typical experiment the interface was equilibrated for several hours at zero growth velocity and the downward motion of the sample tube at constant velocity would then be started. The solidification velocity does not of course immediately attain the velocity at which the tube is withdrawn: instead, the interface starts to move downward with the tube and as the gradients change solidification commences and the solidification velocity accelerates toward the tube withdrawal velocity, which is reached when the interface reaches a steady state position. When crystal growth starts, the radial gradients increase both due to the effect of drawing the hotter material downward through the viewing block and due to the latent heat emitted from the solid-liquid interface. The convective flow pattern is correspondingly altered. In cases where the axis of the toroidal roll was initially displaced from the tube center (Figure 6b), the axis moves toward the center of the tube. In radially symmetric cases, the upward flow velocity near the center of the tube increases when crystal growth starts. The upward flow velocities at the tube center, 2.5 mm above the interface, were typically 20-40 μm/s for a sample growing at 2 μm/s.

Figure 8 shows examples of measured convective flow tracks in the sample containing 2.6×10^{-3} wt.% ethanol. Figure 8a shows the flow field before the start of crystal growth, and Figure 8b shows the flow field 19 minutes after the start of sample motion at 2 μm/s. It is seen that in Figure 8b the flow velocities have increased significantly compared to those in Figure 8a. Note that in Figure 8b the time is still small compared to the time (D/v^2k) required to establish the steady state solute distribution, which in this case is approximately 95 minutes.

the slowest velocities at which it was seen (about 2 μm/s) it attained its most dramatic appearance (Figure 10), becoming sharply pointed and about 1 mm deep before breaking down into a cellular structure. At a growth velocity of 3 μm/s, the pit was considerably wider and shallower when the cellular structure appeared (Figure 11) and at 4 μm/s the pit was hardly discernable from the overall concavity of the interface when the cellular structure appeared. The range of growth velocities over which this effect is seen is therefore very narrow, but it is a critical range in that it is near the limits of the concentration and velocity for which the growth of microsegregation-free crystals is possible.

The marker particles indicate low flow rates in the liquid within the pit, and in all cases show that the pit lies under the point at which the flow converges and turns upward.

The formation of such pits has not been observed in the pure sample, nor has it been observed under conditions where the flow forms a single roll (Figure 6c) instead of a toroidal roll (Figure 6a or 6b).

The auxiliary heater surrounding the sample could be used to alter the radial temperature gradients in the vicinity of the solid-liquid interface. Ideally it would act as a substitute source of latent heat, establishing a temperature gradient discontinuity within the transparent viewing block to match that created within the succinonitrile by the emission of latent heat (Eq. 1). In practice it was generally found that as the radial gradients were decreased by the use of the auxiliary heater, the toroidal flow field could be suppressed but there were always enough asymmetries in the system to yield a single roll flow pattern. By

Together with the change in the fluid flow, there is a change in the interface shape which develops when crystal growth starts. In the pure material the interface assumes the shape of a smooth upwardly concave bowl (Figure 9). This sample was sufficiently pure that no conditions (other than bulk supercooling of the liquid) were found which resulted in interfacial instabilities. Qualitatively, this is the interface shape change which would be expected even in the absence of fluid flow. It is not known how much additional interface shape change is produced by the fluid flow which does occur.

A much more complex shape change occurs during crystal growth in the ethanol-doped sample at velocities close to that which leads to the formation of interfacial instabilities. For growth at 1 μm/s, the interface develops a gentle bowl shape similar to the pure material, and remains featureless. For growth at 5 μm/s or more the interface rapidly develops an overall cellular structure. At intermediate velocities, however, the interface starts to develop a smooth bowl shape but after an incubation period which varies in length from a few minutes to as much as two hours, an additional macroscopic depression develops in the interface directly under the point where the radial inward flow above the interface converges and turns upward. Once the depression appears, it deepens rapidly until interfacial instabilities develop within it. These instabilities then develop into cells or dendrites which grow rapidly to fill the pit up to the level of the original bowl-shaped interface. This interface then advances with a localized cellular region in the area where the pit had been, surrounded by a featureless (cell-free) area.

The shape of the pit varied with the solidification velocity. At

activation of the auxiliary heater it was found that the formation of the interface pit could be suppressed during growth at 2 μm/s, but the effect may better be attributed to the change of the flow pattern rather than to an actual suppression of the flow.

An additional convective flow was occasionally observed in cases where a vapor bubble was trapped at the solid-liquid interface. This could occur when the sample was melted down into a region where an axial shrinkage pipe had been formed by a previous freezing operation. When the melt contacted the shrinkage pipe, the vapor bubble which formed would sometimes be held at the interface by surface tension forces before breaking away and rising to the top of the tube. The flow in the liquid near the bubble was often similar to that which occurred in its absence, but at other times a counter-rotating toroidal flow would be present in the liquid immediately above the bubble (Figure 12). The flow rates in the counter-rotating flow were at least an order or magnitude faster than those in the normal flow pattern, and immediately adjacent to the bubble surface they were so rapid that they were not recorded on the photographs. The counter-rotating flow was most vigorous shortly after slight changes in the position of the bubble.

V. DISCUSSION

The formation of a transient macroscopic pit in a solidifying sample surface, in the presence of both convection and solute, appears to be an important stage in the development of a localized cellular structure.

The convective flows observed in these experiments can be attributed to the effects of radial temperature gradients, which in the case of stationary samples are the result of heat losses to the environment and

in the case of growing samples have an additional contribution from the interaction of the latent heat with the chamber walls.

In stationary samples, the composition of the liquid is uniform and therefore is unaffected by the convective flow. In a solidifying sample with a solute concentration C_0 far from the interface, a solute-enriched layer is present in the liquid adjacent to the interface. At steady state and in the absence of convection, the solute concentration C_L in the liquid ahead of a planar interface would have a simple exponential form

$$C_L = C_0 \left[1 + \frac{1 - k}{k} e^{-Vx/D}\right] \qquad (2)$$

and the composition immediately adjacent to the interface would be C_0/k. Because of the low value of k for the succinonitrile-ethanol system (0.044), the concentration differences are large. Thus in the sample containing $C_0 = 2.6 \times 10^{-3}$ wt.% ethanol, the composition of the liquid adjacent to the interface would be 5.9×10^{-2} wt.% ethanol and the interface temperature would be depressed 0.2 K below the temperature for equilibrium of solid with liquid of composition C_0.

Convective flow will change the temperature and solute fields in the liquid ahead of the interface. However, because the thermal diffusivity is approximately 100 times as large as the solute diffusivity, the solute field can be much more severely distorted than is the temperature field. The distortion of the liquid temperature and composition fields will lead to changes of the interface shape.

In a crystal growth system such as that shown in Figure 5, in the absence of convection the solid-liquid interface of a growing crystal will not be planar but will be macroscopically concave due to the radial

heat losses and the interaction with the chamber walls. When solute is present, this concavity will cause the solute distribution in the liquid adjacent to the interface to be somewhat non-uniform even in the absence of interfacial instabilities [8].

If we add in the effect of convection, the interface shape will be modified in the pure material by the convective transport of heat. In a crystal growth apparatus such as ours, we can expect the convective flow to reduce the deviation of the interface from planarity because the downward flow on the cooler parts of the tube (near the walls) will bring warmer material from above to the interface region. The actual magnitude of the interface shape change due to the convective flow in the pure material is not known, although some indication of it could be obtained by comparing interface shapes in our experiments to shapes observed when the solid lies above the liquid, in which case the convection would increase the deviation from planarity. This type of geometry was approximated during the zone refining of the samples, and the deviation from planarity was much more pronounced.

During solidification of the sample containing ethanol, the convective flow can change the distribution of solute ahead of the solid-liquid interface. A simple uniform horizontal shear flow above the interface would not alter the exponential solute distribution, but substantial effects can be expected with the fluid flow patterns which prevail in a finite sized system. For the toroidal flow as illustrated in Figure 6a, the material flowing down near the walls will have composition close to that of the bulk liquid and the concentration of ethanol ahead of the interface near the walls will therefore be less than that predicted in

the absence of convection. As the liquid moves radially inward above the interface, it will accumulate the rejected solute. Because of the radial nature of the flow, solute will be relatively concentrated in the vicinity of the node where the flow converges and turns upward, in a manner somewhat analogous to the process by which the marker particles accumulate in this vicinity.

We feel that the interface pit which develops at certain growth velocities is the result of this localized concentration of solute by the thermally-induced convective flow field. The evidence supporting this hypothesis is that

1) The pit is seen only in the sample doped with ethanol; and

2) The pit occurs directly under the point where the flow field converges, even when this point is displaced from the tube center by asymmetries of the thermal field, and formation of the pit is not observed when the asymmetries are strong enough to cause the fluid flow to change from a toroidal (Figure 6a) to a single roll (Figure 6c) configuration.

Chang and Wilcox [8] have reported observations of solid-liquid interface shapes as affected by radial heat flow and convection during zone melting of napthalene. Their heat flow geometry, and hence their convective flow fields, were different from that which occurred in our experiments. They observed localized cellular break-down of the solidifying interface, which in some cases occurred within an indentation of the interface. They attribute the localization of interface break-down to the redistribution of heat and solute by convection currents, but do not report the effect which we find in which the convective redistribution of solute causes a macroscopic change of interface shape.

VI. CONCLUSIONS

A small concentration of ethanol in succinonitrile is sufficient to induce interfacial or thermosolutal convective instabilities during unidirectional upward solidification. Radial temperature gradients present during solidification in a cylindrical tube also induce convective flow, and when solute is present it is redistributed by the convective flow to produce changes in the shape and interfacial stability of the solid-liquid interface.

Acknowledgement

The authors acknowledge the support of NASA's Microgravity Science and Applications Division.

References

1. S. R. Coriell, M. R. Cordes, W. J. Boettinger, and R. F. Sekerka, J. Crystal Growth 49, 13 (1980).

2. S. R. Coriell, M. R. Cordes, W. J. Boettinger, and R. F. Sekerka, Adv. Space Res. 1, 5 (1981).

3. S. R. Coriell and R. F. Sekerka, PhysicoChemical Hydrodynamics 2, 281 (1981).

4. W. W. Mullins and R. F. Sekerka, J. Appl. Phys. 35, 444 (1964).

5. M. J. Timmermans and Mme. Hennaut-Roland, Journal de Chimie Physique 34, 693 (1937).

6. C. A. Wulff and E. F. Westrum, J. Phys. Chem. 67, 2375 (1963).

7. R. J. Schaefer, M. E. Glicksman and J. D. Ayers, Phil. Mag. 32, 725 (1975).

8. C. E. Chang and W. R. Wilcox, J. Crystal Growth 21, 182 (1974).

Figure Captions

Fig. 1. The concentration of ethanol in succinonitrile above which interfacial or convective instability occurs.

Fig. 2. The ratio of the instability wavelength, λ, to the diffusion boundary layer thickness, D/v, at the onset of instability.

Fig. 3. Effect of the temperature gradient in the liquid on the concentration of ethanol in succinonitrile required to induce instability.

Fig. 4. Succinonitrile-ethanol phase diagram, with lines of constant liquid density.

Fig. 5. Exploded view of crytal growth apparatus.

Fig. 6. Convective flow patterns above solid-liquid interface for (a) symmetrical, (b) slightly asymmetrical and (c) highly asymmetrical heat losses.

Fig. 7. Plume of particles marking the axis of a toroidal flow pattern.

Fig. 8. Measured flow velocities above the solid-liquid interface (a) before the start of growth and (b) 19 minutes after the start of growth.

Fig. 9. Concave interface resulting from growth in pure succinonitrile.

Fig. 10. Macroscopic depression in the solid-liquid interface of a sample containing 2.6×10^{-3} wt.% ethanol, growing at 2 μm/s.

Fig. 11. Macroscopic interface depression in sample growing at 3 μm/s.

Fig. 12. Vigorous counter-rotating toroidal flow above vapor bubble in sample containing 2.6×10^{-3} wt.% ethanol.

Table. I. Properties of Succinonitrile

Property	Symbol	Value	Reference
Density of Liquid	ρ_ℓ	988 kg/m^3**	[5]
Thermal Expansivity of Solid	α_s	-5.6×10^{-4}/K	[6]
Thermal Expansivity of Liquid	α_ℓ	-8.1×10^{-4}/K	[5*]
Shear Viscosity	η	2.6×10^{-3} Pa-s**	
Kinematic Viscosity	ν	$2.6 \times 10^{-6} m^2/s$**	[5]
Latent Heat of Fusion	L	4.70×10^4 J/kg	[6]
Thermal Conductivity of Solid	k_s	0.225 J/mKs**	[7]
Thermal Conductivity of Liquid	k_ℓ	0.223 J/mKs**	[7]
Thermal Diffusivity of Solid	κ_s	$1.16 \times 10^{-7} m^2/s$**	***
Thermal Diffusivity of Liquid	κ_ℓ	$1.12 \times 10^{-7} m^2/s$**	***
Distribution Coefficient for Ethanol in Succinonitrile	k_o	0.044	****
Liquidus slope for Ethanol in Succinonitrile	m_ℓ	3.6 K/wt.%	****
Solidus slope for Ethanol in Succinonitrile	m_s	81 K/wt.%	****

* Indicates value derived from properties given in cited reference.
** Indicates value of property at melting point, 331.23K.
*** Indicates property derived from other properties in the table.
**** Indicates properties measured in current work.

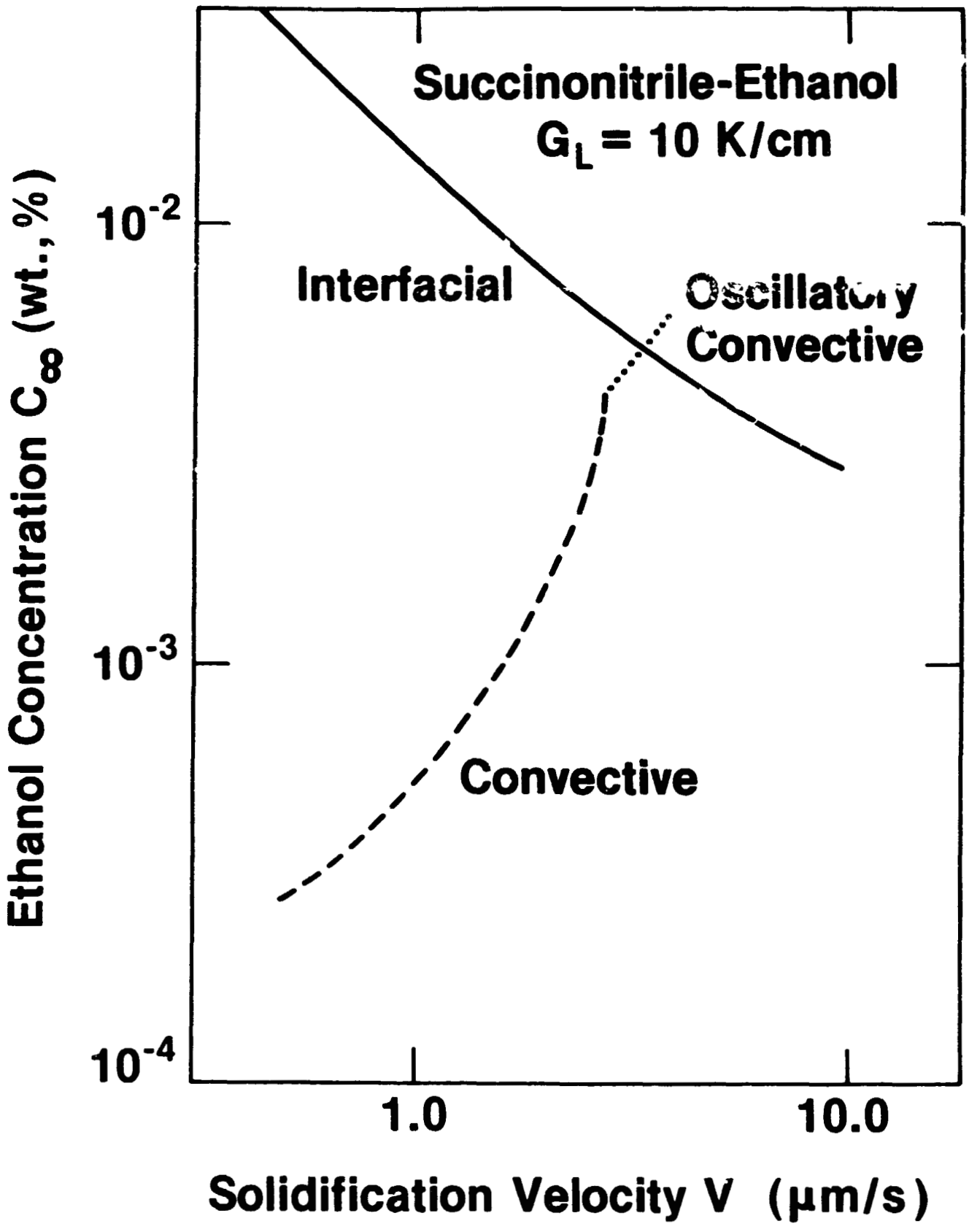
Succinonitrile-Ethanol
G_L = 10 K/cm
Interfacial
Oscillatory
Convective
Convective
10^{-2}
10^{-3}
10^{-4}
1.0
10.0
Ethanol Concentration C_∞ (wt., %)
Solidification Velocity V (μm/s)

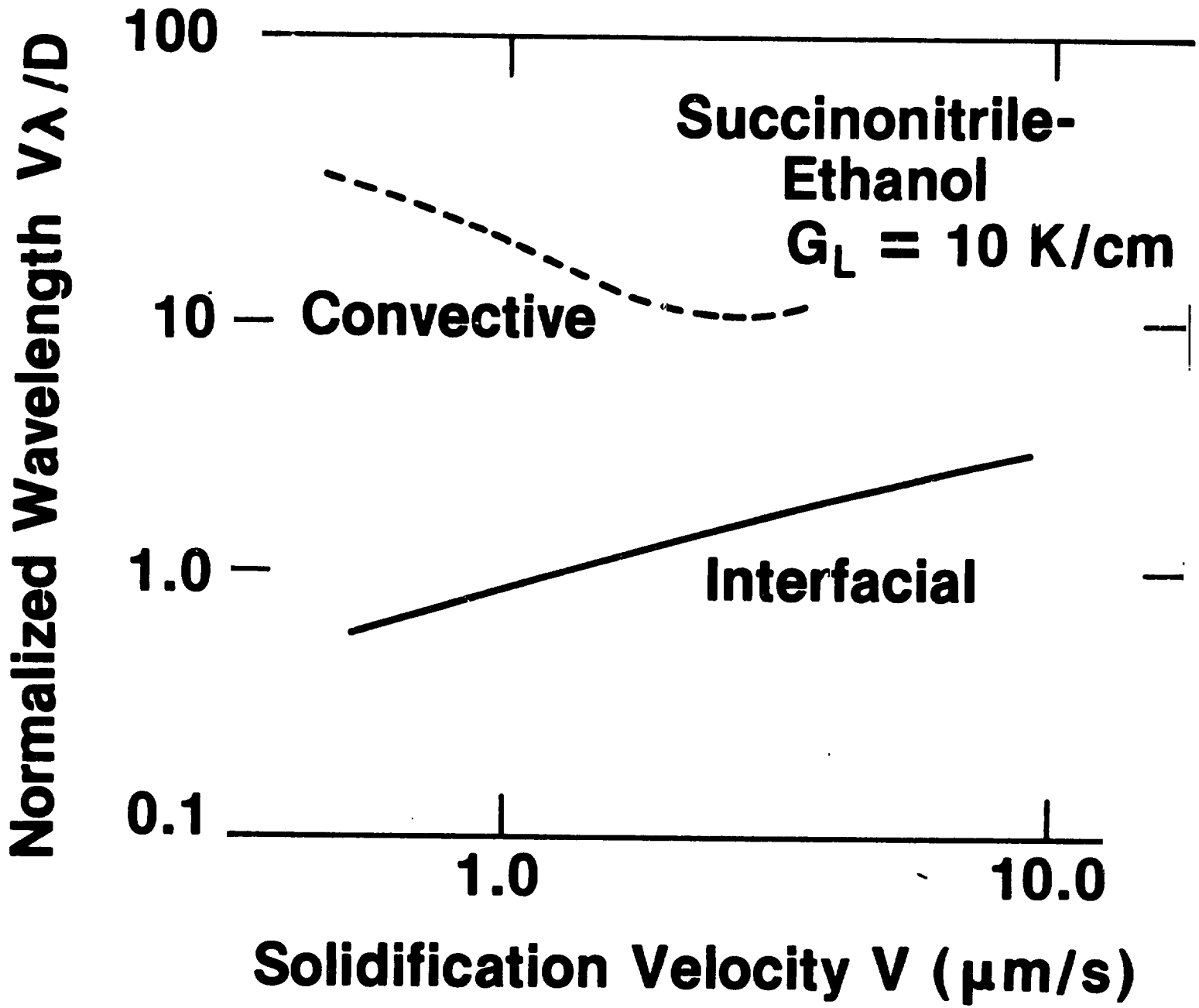
100
10
1.0
0.1
Normalized Wavelength VλD
Succinonitrile-
Ethanol
G_L = 10 K/cm
Convective
Interfacial
1.0
10.0
Solidification Velocity V (μm/s)

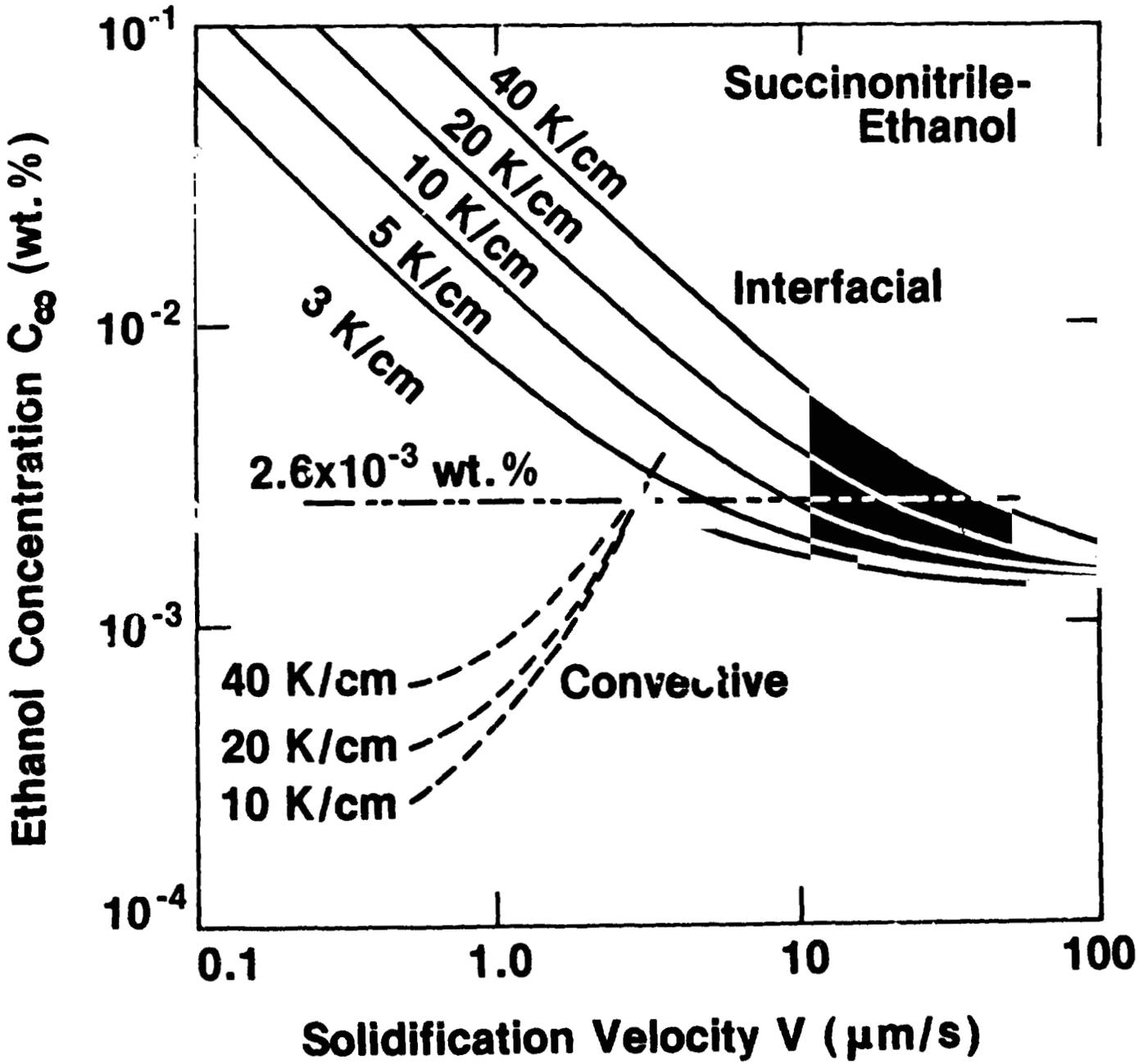
Succinonitrile-
Ethanol
40 K/cm
20 K/cm
10 K/cm
5 K/cm
3 K/cm
Interfacial
2.6x10-3 wt.%
40 K/cm
20 K/cm
10 K/cm
Convective
Ethanol Concentration C∞ (wt.%)
10-1
10-2
10-3
10-4
0.1
1.0
10
100
Solidification Velocity V (μm/s)

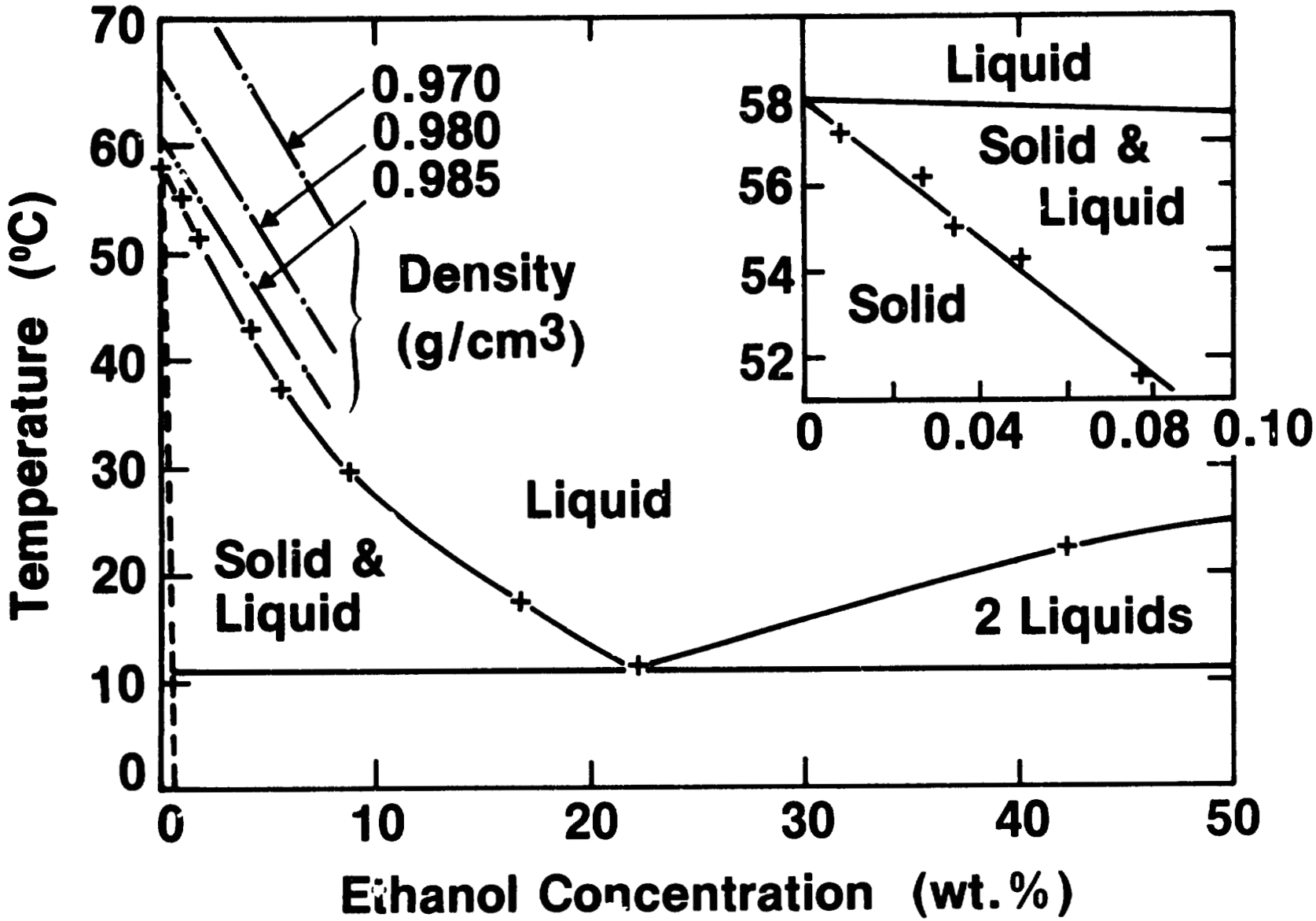
Temperature (°C)
70
60
50
40
30
20
10
0
0.970
0.980
0.985
Density
(g/cm3)
Liquid
Solid &
Liquid
2 Liquids
0
10
20
30
40
50
Ethanol Concentration (wt.%)
Liquid
Solid &
Liquid
Solid
58
56
54
52
0
0.04
0.08
0.10

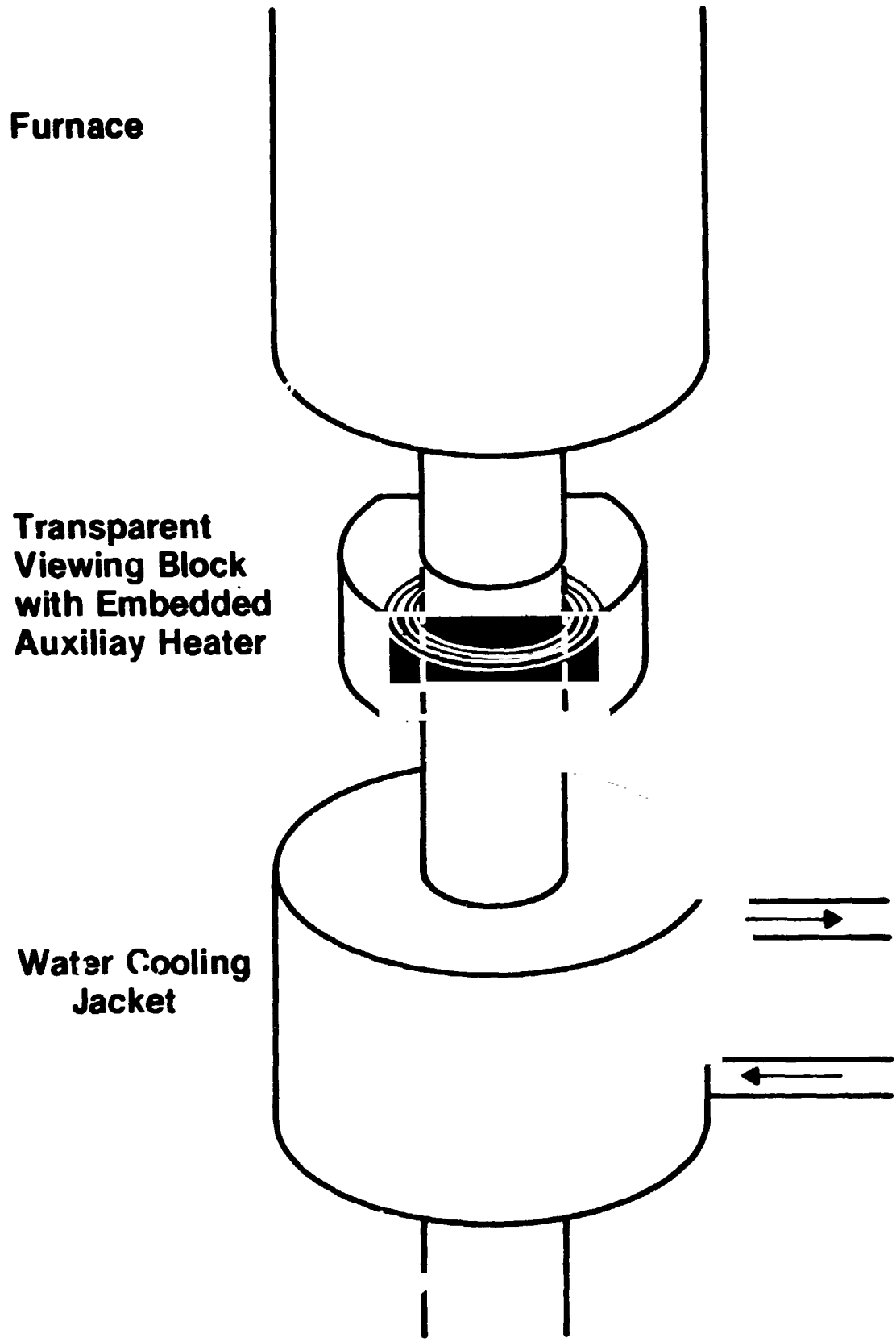
Furnace
Transparent
Viewing Block
with Embedded
Auxiliay Heater
Water Cooling
Jacket

(a)
Solid
Liquid
(b)
Solid
Liquid
(c)
Solid
Liquid

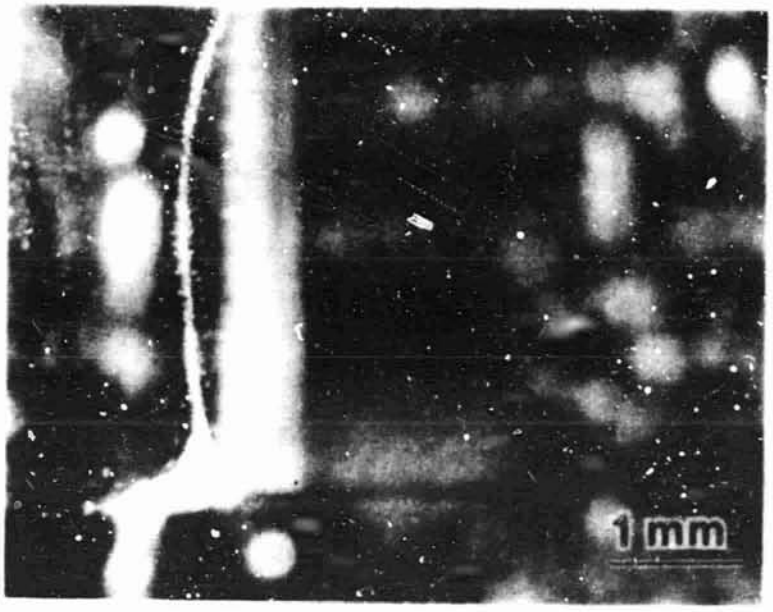

Fig. 7

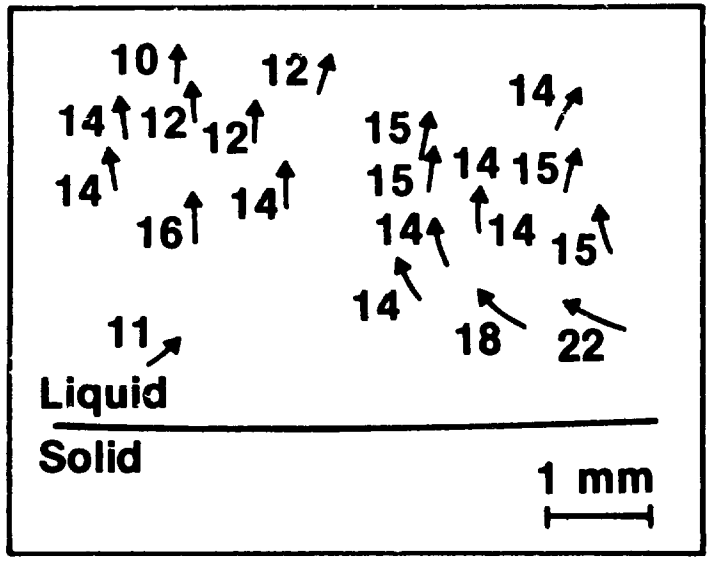
10
12
14
14
12
12
15
14
15
14
15
14
14
16
14
14
15
14
18
22
11
Liquid
Solid
1 mm

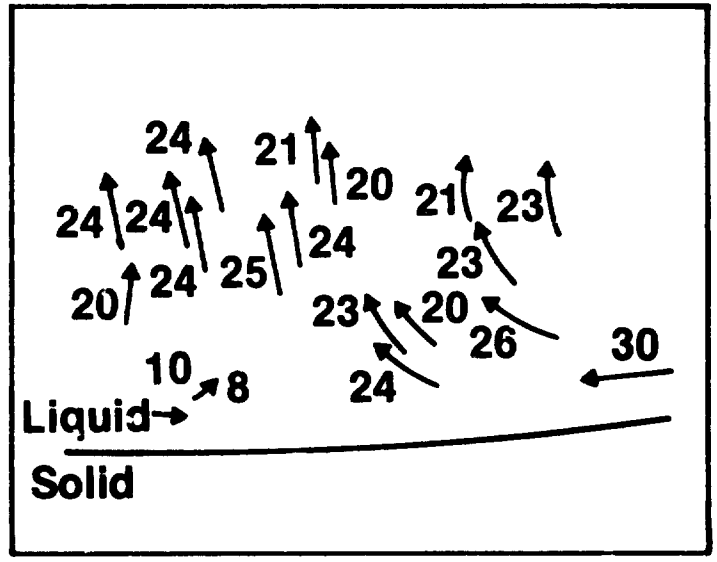
24
21
20
21
23
24
24
24
24
25
23
20
23
20
26
30
10
8
24
Liquid
Solid

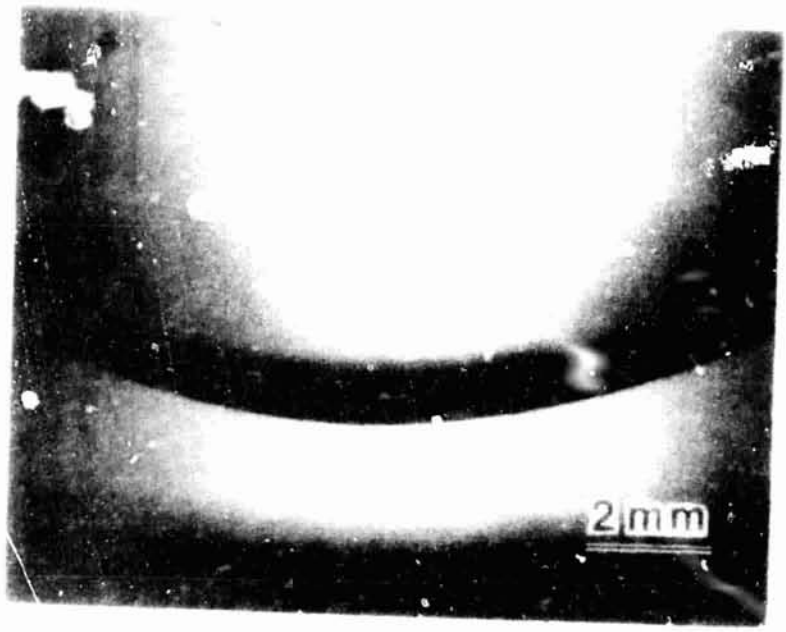

Fig. 9

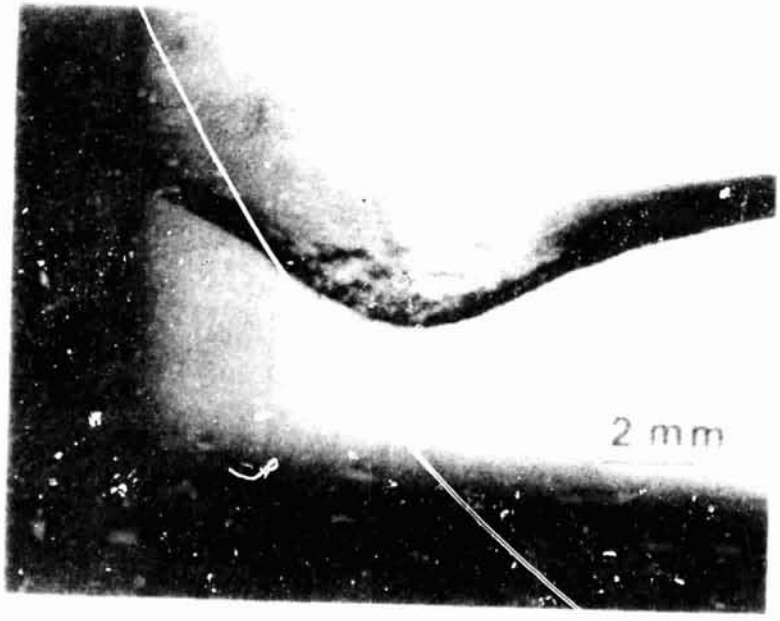

Fig. 10

Fig. 11

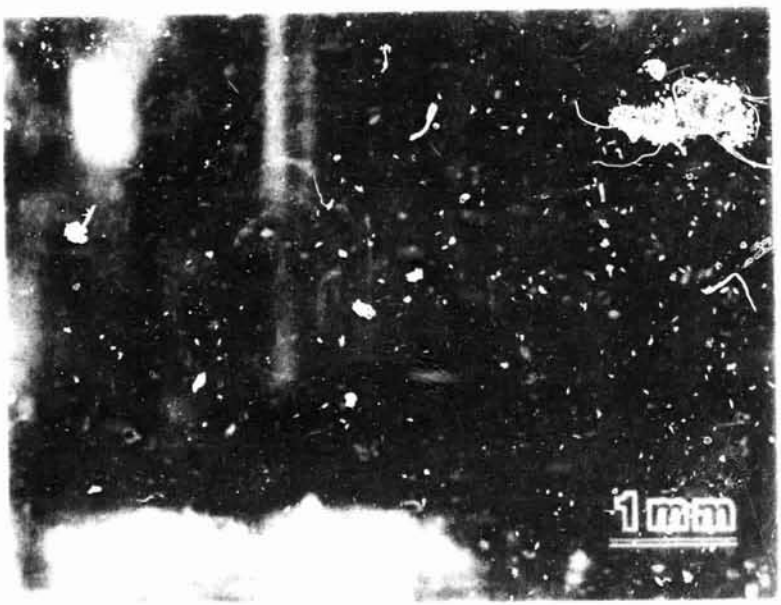

Fig. 12

Task 3
Measurement of High Temperature Thermodynamic Properties

D. W. Bonnell
Inorganic Materials Division
Center for Materials Science

SUMMARY

The newly developed General Electric Space Systems Division (GE) imaging optical pyrometer was completed, tested, and calibrated in in-service operating conditions. This pyrometer is designed to allow accurate temperature measurement of a levitated high temperature sample whose specific heat then can be determined by dropping it into a calorimeter, or in space flight by moving the calorimeter to enclose the sample. The pyrometer has the capability for two color operation, with the alternate colors sampled at several hertz. The unit proved to be stable in operation, and appears to be a reasonable prototype. Special techniques were developed to connect the temperature scale of the pyrometer to that of the standard lamp.

For the electromagnetic induction levitation system, a new, tighter coil design was tested with major improvement in holding ability and stable levitation for high melting point metals. Successful coupling of this levitation coil and the electron-beam heat source needed to melt the sample proved more difficult than anticipated, with the result that successful complete melting of tungsten has not yet been achieved.

An additional major effort of this reporting period is the preparation of a chapter on Levitation Calorimetry, which represents a comprehensive review of the subject of electromagnetic levitation and thermophysical property measurement, the first such effort since the early 1960's. Levitation activities at Rice University have resumed in full force, with complete reactivation of their facilities. A number of new materials (silver,

gallium, etc.) are being studied, and regular discussions indicate that publication quality results are now being obtained.

Introduction

The primary objective of this task has been to develop, in conjunction with General Electric Space Systems Division (GE), and Rice University (RICE), the techniques, methodology, and experimental apparatus for measuring thermophysical properties (e.g., heat of fusion, enthalpy increment, heat capacity, etc.) of materials at extremely high temperatures. A primary technique has been the development of a coupled electron-beam heating/electromagnetic levitation-calorimeter system. The e-beam heating/levitation apparatus is based on equipment developed originally by GE specifically for melting tungsten. As the heat of fusion and enthalpy increment functions for tungsten are known only through estimation and indirect measurements [Bonnell, 1983], and tungsten occupies a unique position as the most refractory element, adapting this apparatus to calorimetric measurements seemed a particularly significant opportunity to expand the limits of ground-based property measurements.

The technical difficulty of merging these two techniques has proved to be a measure of the dividing line between experiments which can be performed on the ground, and those which will require reduced gravity for accomplishment. The significance of these experiments lies in the observation that the temperatures require heater powers (10 to 100 kW) for reasonable sized samples, far in excess of that expected to be available in space in the near future. Thus, to obtain the scientific data, and to continue to develop methods for use in space, the clearest path which will allow development of hardware able to take advantage of the low-gravity environment of space has been to pursue limiting ground-based cases.

GE Pyrometry System

The new GE imaging pyrometer was optically similar to the previous system, and installed in the same manner. This arrangement and the techniques developed for calibration and operation are discussed in detail elsewhere [Bonnell, 1981]. The new GE imaging pyrometer system was designed around a commercially available photodiode array camera system. Custom circuitry to allow the gating of any individual pixel to two companion high quality sample-and-hold operators was included. This allowed dc sampling and display of the selected single pixel output for each of two colors passed by two narrow band filters. The filters were mounted in an arm which could be alternated between the two filters by a 180° stepper motor. The location of the arm in the two alternate positions was sensed by switch closures, and the camera image collection (pixel gating) restricted to frame times when the filters were stationary. The normal 30 hz framing rate was used, and the filters could be changed with the loss of only one frame time. The filter change frequency was limited by the motor to a few hertz.

Since the camera uses silicon diode based detection, and is thus sensitive to wavelengths beyond 1000 nm, it was practical to select filters straddling the sensitivity peak by choosing one of the band-pass wavelengths in the infrared. The selected filters were 850 and 656 nm center frequency, 10 nm Full-Width-at-Half-Maximum band pass, approximately 13 mm diameter dichroics. The extreme narrow band pass choice was based on GE's expectation of radiance at the melting point, and the available maximum aperture, approximately 10 mm. The choice was correct and at melting, output from the pyrometer for both wavelengths was about mid-scale. However, there was no direct way to obtain significant output from the system at

standard lamp temperatures which did not jeopardize the stability of the standard lamp (about 1600°C for vcauum [ASTM, 1975]). This determination is essential to calibrate the unit to the brightness temperature scale, to obtain scale intercomparisons among the various aperture/filter combinations, and to perform running checks on outgas/vaporization coating of the vacuum system windows and mirrors.

One way to deal with this problem would be to use wider band-width filters, and insert neutral density filters for coarse scale control. This alternative is still possible, but was not available at test time.

A modification of the camera control circuitry so that image collection could be spread over multiples of the frame time allowed the camera to be used as an integrator. Since calibration is a static process, this was a reasonable alternative, although it made alignment of the camera somewhat more awkward. Even though digital multiples of the frame time were used (typically 10 frame times), the actual integration ratio had to be determined empirically, as two frame times includes the retrace time, for example, which is not part of one frame time. Also, there is the possibility that the sensor array may not store the image without losses. The empirical determination yielded a gain value for ten frame integration of 10.47 ± 0.3. The error was estimated based on the digital granularity of the smallest signal.

A disk with a series of apertures was located behind the filter arm to provide known aperture limiting, and wavelength independent gain. The apertures were measured with a reticule comparator. Even using the integration technique, it was not possible to get enough signal to intercompare the smaller aperatures with the standard lamp. If the current filters are

to remain as is, it would be wise to dismount the apertures and measure their areas photometrically. Table 1 lists the aperture plate dimensions. The lineal measurement pair represent the largest and the smallest cross sections. The holes were not visibly oval so the aperture area ratios were based on the average of the extrema measurements. For the temperatures observed (maximum ~3800 K), it was never necessary to use other than the A and B apertures.

Table 1

Pyrometer Apertures

Aperature	Diameter in.[a]	Area[a] Sq. in.	Ratio
A	0.239 0.243	0.04562	> 2.13
B	0.162 0.168	0.02138	> 1.96
C	0.117 0.119	0.01094	> 2.00
D	0.082 0.085	0.00548	

[a] in. = 2.54 cm.

Calibration of the pyrometer was carried out in the manner outlined before [Bonnell, 1981]. Briefly, the pyrometer output was compared to a calibrated micro-optical pyrometer reading the temperature of a miniature strip lamp inside the vacuum system. The levitaton coil system flange was

replaced for this purpose by a pyrex plate to allow direct viewing of the filament. The pyrex plate absorbance was measured separately by measuring the brightness temperature of an external lamp with and without the plate in the optical path.

The current (measured by the voltage drop across a quality 0.0100 ohm shunt) applied to the lamp during the process of calibrating the pyrometer served to calibrate the standard lamp for later use in determining vacuum window and mirror absorption changes. It is to be noted that the strip lamp was used at brightness temperatures much higher than the long term limits recommended for pyrometers [ASTM, 1975]. The stability of the lamp was checked by reproducing temperatures below the safe limit after use at the higher values.

The observed output of the pyrometer (V, in volts) is related to the brightness temperature by the expression,

$$\frac{1}{T_B^*} = \frac{\lambda}{C_2} \ln V - k \frac{\lambda}{C_2}$$

derived from the familiar Wein approximation to the Planck radiation law. This form indicates that the best fit to experimental T versus photometer output is a one parameter fit to determine k. Two parameter fits, in which the leading term (λ/C_2) is a parameter, produced fits in which the leading term was within statistically estimated error limits of the theoretical slope, but such fits actually represent the data more poorly, as they do not have correct extrapolation behavior in the original data space. The one parameter fit for the 656 nm filter is

$$10000/T_B^* = 3.759 \pm 0.02 - 0.4561 \ln V'$$

as shown in Figure 1. For the 850 nm filter, the result is

$$10000/T_B^* = 3.362 \pm 0.02 - 0.5908 \ln V'$$

Note that the functions are for V' measured in the x10 integrate mode. Since the true gain, g, due to integration was measured (g = 10.47), the relationship for the single frame high temperature operation mode is obtained by substituting V' = V*g in the above. This gives the working expression for brightness temperature as,

$$10000/T_B^* = 2.688 \pm 0.03 - 0.4561 \ln V \qquad \text{(656 nm filter)}$$

and

$$1000/T_B^* = 1.975 \pm 0.03 - 0.5908 \ln V \qquad \text{(850 nm filter)}$$

Corrections for aperture are gain corrections, and made in the same manner. Ln(E), the emissivity, and window obscuration corrections are also treated as gain terms, and the corrections made accordingly.

In operation, the pyrometer system showed a slight but disconcerting image shift with the changes of the two filters. The shift was never large enough to significantly affect normal temperature measurements, but as the standard filament image is only about twice the width of a measurement pixel, calibrations were made with the automatic filter switching off.

The system was free of the interference and much of the noise of the previous system. The window obscuration problem, due to vapor deposition at high temperature, is still a major correction, and changes rapidly during an experiment. This makes it virtually impossible to determine temperature even approximately during an experiment and remains a significant problem. A method for dealing with this problem in real time has been suggested [Bonnell, 1981], but not yet prototyped.

Levitation Calorimetry

An extensive effort to obtain more data on liquid tungsten was made during this reporting period. The changes suggested from the last effort

[Bonnell, 1983] were made, with mixed results. A newly designed coil was installed (see Fig. 2). This coil provided improved sample stability, with little tendency to lose the samples due to inadvertant contact with the coil, or due to sample ejection during excessive oscillations, once the upper to lower coil gap was decreased. The upper turn was deliberately left larger than optimum to minimize effects of the RF field on electron beam focus, and to insure that it could be protected by the molybdenum shade ring. This coil was nearly optimum for the samples. Although liquefying tungsten is a serious problem, and has become increasingly difficult as the apparatus ages, in two cases where other system failures prevented capture, samples which were apparently completely molten were contained by the coil.

The primary problem with this coil system was that it intercepts more radiant energy from the levitated sample because its turns are much closer to the sample. Perhaps even more importantly, beam electrons, forward-scattered from the sample, are scattered onto the lower turns of the coil more effectively. The combination of these two effects caused a series of coil failures, and subsequent severe contamination of the aluminum walled vacuum system with water. Although the system has excellent safety interlocks, the rupture of a coil turn under 50 to 60 psig water pressure results in ounces of water inside the vacuum system. When the problem was finally correctly diagnosed, higher pressure water pumps were not available. We were able to divert the water supply for another GE experiment to the task. That water system was designed to deliver about 50 gallons to a linear levitation system over the period of minutes. It consisted of a large 125 psig rated pressure vessel filled with water and pressurized to 120 psig with nitrogen gas. At this

pressure, the levitation coil used about 4 liters of water per minute, an approximately 1.5 improvement in water flow. This allowed 35 minutes operation time with margin for orderly shutdown. This rate of water flow was adequate for the increased heat dissipation requirements. It would be desirable in the future to have a pump to supply 125 psig water, although no problem ensued from the pressurized system. Higher pressure would also be recommended, up to the working limit of the reinforced hose, as it is still not certain how much safety margin remains.

Two additional problems accompanied the coil failures. The first was repeated failure of the automatic gate system to function. This trouble was finally identified as being caused by insufficient clearance for the radiation gate hub, brought about by repeated minor splatters of molten tungsten, aluminum (from the upper gate housing and vacuum system walls) and tantalum (from the gate system heat shields). Curiously, the system would work on the bench, but jam erratically under vacuum. The problem was rectified only by a complete overhaul of the entire system. The other problem was a return of the sample contamination problem. The problem was not immediately identifiable due to difficulty with electron beam melting. When finally correctly diagnosed (as due again to soft solder vapor contamination) it was found that a small run of soft solder from a feedthrough cooling tube was in line of sight to the coil from below. The problem was rectified by removing all excess soft solder. However, extreme care will be necessary in the future as critical joints in the coil flange are held together with soft solder, which cannot be removed.

Scanning Electron Micrographs (SEM) examination of a sectioned contaminated specimen with x-ray fluorescence showed of the order of 1/2 percent zinc present. Quantitation was difficult, as 30 KeV excitation had to be used, which produces

some spurious peaks from the steen vacuum chamber. It was not possible to tell if there was significant concentration along grain boundaries. The sample showed large grains, indicative of near melting. Except for the oblate shape change without surface melting, it would be difficult to differentiate this specimen from a good run. These results are tentative at present, with more work planned.

The electron beam continued to be the limiting part of the system. A molybdenum shade ring was reinstalled to protect the top turns of the coil. This ring was in place during the coil failures, implying that the direct electron beam melting of the coil was not a likely cause of coil failure. Extensive tests of the interaction of the beam and coil were carried out at all power levels of beam and levitation field. Tests involved samples mounted on the previously developed "sting," [Bonnell, 1983] as well as freely levitated specimens. No discernable defocusing of the beam by the RF coil occurred under any operating conditions. The electron beam image consisted of two similar oval shaped spots separated by approximately 1 cm. It was not possible to merge the spots without defocusing the beam. Any focus degradation made it impossible to melt the sample, even with 100 mA, 30,000 V beam currents. In addition, when placing one spot on the sample, the other spot could not be seen, and presumably impinged the side of the sample, or the coil. This uncertainty makes analysis of the problem more difficult. Another difficulty appears to be related to the need for a precisely shaped electron beam spot. If the spot is too small, drilling of the specimen occurs [Bonnell, 1983]; if too large, the sample will not melt. Considerable more effort is required here by GE.

The new coil provides good holding for the current 0.9 cm diameter samples. A possible improvement in melting ability should be attainable

by using even smaller samples. Samples 0.65 cm in diameter are recommended.

The main requirement seems to be to improve the electron beam image shape, and to eliminate the extra spot. This will probably require dismounting the beam source and adjusting it in successive tries.

Tungsten Heat of Fusion

A selection of recovered samples were sectioned and examined metallographically. All the sectioned samples showed interior voids, suggesting that significant liquefication had occurred. However, no sample showed clear regions with no grain boundaries. It is apparent that during long heating in the levitation coil, grain growth occurs. Figure 3 shows the original grain structure, both of the original rod stock and a ground sphere. Figure 4 shows micrographs of a typical run, labeled A [see Bonnell, 1983]. There appear to be two distinct regions. The smaller region with finer grain structure is in contact with the central void, and the region (upper right in figure) where the electron beam impinged. The difference in grain structure between this region and the rest, which shows major grain growth, may be evidence for separation of melted versus not melted tungsten. However, a more reasonable explanation is the grain growth occurs throughout the heating process, and much of the grain structure could be due to multiple nucleation sites upon resolidification. The sectioned samples also suggest that different parts of the sample could have been molten at different times. This is consistent with the difficulty in melting noted above.

The sectioned samples do support the previously assigned extent of melting, but are not conclusive enough to improve those assignments.

Figure 5 shows a plot of the available melting tungsten data, fitted

without constraint. The agreement with JANAF [1971] at the solidus is excellent. The disagreement at the liquidus simply represents the previous poor state of data for liquid tungsten, as has been previously discussed [Bonnell, 1983].

Although the present data are a major improvement over previously available data, measurements of the completely molten material are still needed, both for the heat of fusion and to obtain the liquid heat capacity.

Levitation of Tantalum

During the latest tungsten series, a series of tantalum samples were levitated. Tantalum proved easy to melt with the electron beam, requiring less than 60 percent (of 100 mA available) beam current. The liquid could not be held in the coil as was anticipated. The automatic gate and capture system functioned perfectly, and two molten runs were captured. Post run analysis, assuming the observed thermal arrest was the melting temperature, yielded a heat of fusion, relative to the JANAF evaluated solid, of less than 1 kJ/mol. Even correcting to the reported melting temperature with generous error estimates, the observed heat of fusion was less than 8 to 10 kJ/mol, in serious disagreement with 36.6 kJ/mol heat of fusion value from the exploding wire measurements of Lebedev et al., [1971]. Our measurements yield an unrealistically low value for $\Delta S(fus)$. Other tantalum samples in the same series showed the shape deformation characteristic of vaporized soft solder contamination. A number of tungsten samples previous to the tantalum runs were also suspected of being contaminated. However, GE assured us that no soft solder had been used in the coil region, and sample preparation was suspected. With the evidence of bad tantalum runs as well, a very careful examination revealed a tiny smear of soft solder on

the underside of a coolant line in line of sight to the coil, a flow which had occurred in installing a new coil.

All available tantalum samples had been exposed to the soft solder, so no more runs were attempted. Tantalum does appear a good candidate for further study with this system.

Acknowledgements

Mr. C. Brady of the NBS Metallurgy Division prepared the metal sections, and Dr. D. Butrymowicz and Mr. C. Olsen of that Division helped with the SEM examinations.

References

1. ASTM Subcommittee E 20.02 on Optical Pyrometers, G. D. Nutter, Chairman, "Recommended Practice in Optical Pyrometry" (1975).

2. D. W. Bonnell, in "NBS: Materials Measurements," ed. J. R. Manning, NBSIR 81-2295 (1981).

3. D. W. Bonnell, in "NBS Materials Measurements," ed. J. R. Manning, NBSIR 82-2560 (1982).

4. D. W. Bonnell, in "NBS: Materials Measurements," ed. J. R. Manning, NBSIR 83-2772 (1983).

5. D. W. Bonnell, R. L. Montgomery, B. Stephenson, P. C. Sundareswarean, and J. L. Margrave, "Levitation Calorimetry" in Specific Heat of Solids, ed. A. Cezairliyan, in press, (1984).

6. A. Cezairliyan, NBS Report 10326, July 1970, Chs. 7 and 8.

7. JANAF Thermochemical Tables, NSRDS-NBS 37 (1972) and updates through 1983.

8. S. V. Lebedev, A. I. Savvatimskii, and Yu. B. Smirnov, High Temperature USSR 9, 635 (1971).

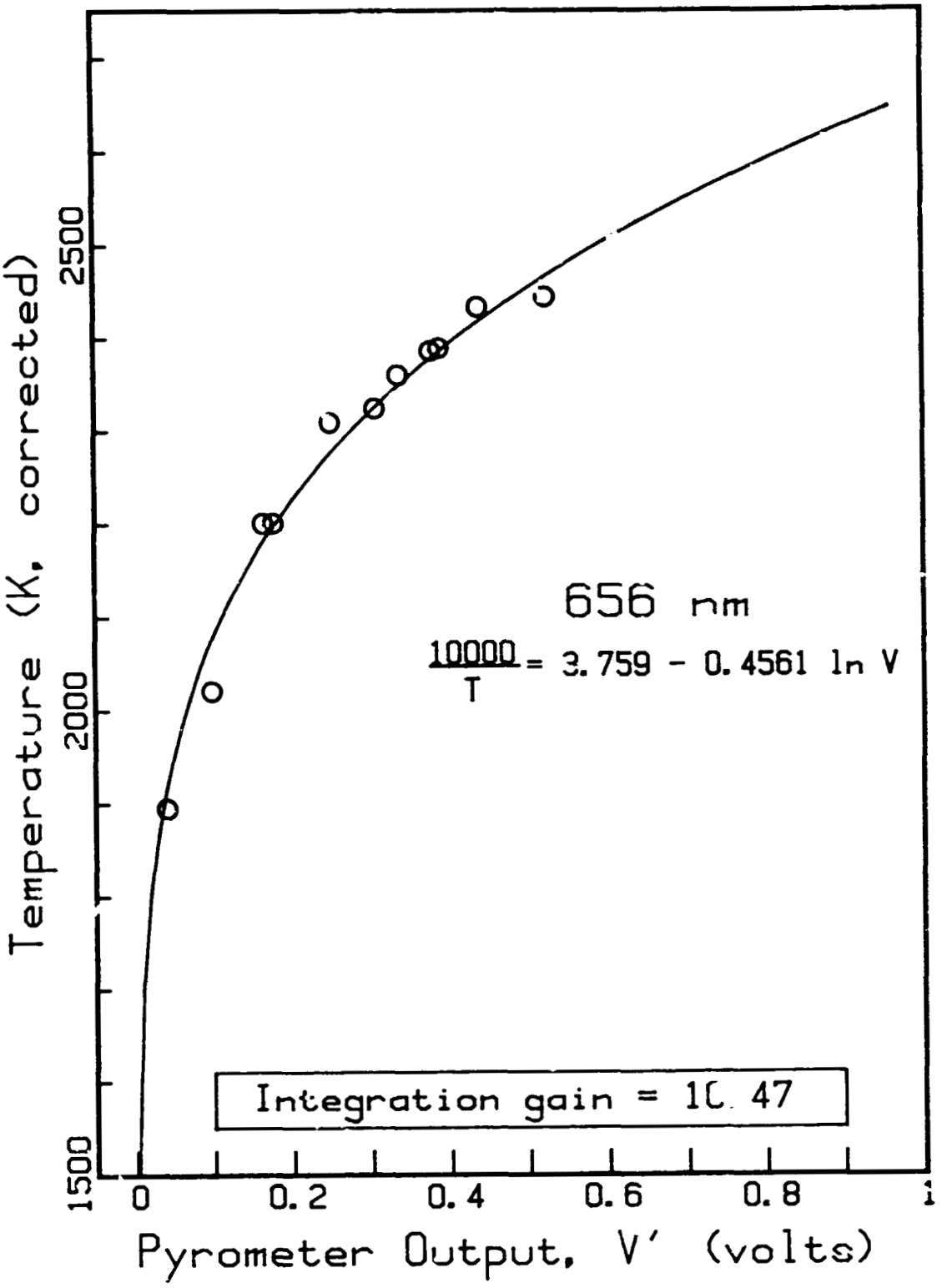

Fig. 1. Graph of 1 parameter fit to pyrometer calibration data with 656 nm filter. V' is observed voltage for integration over ten frame times.

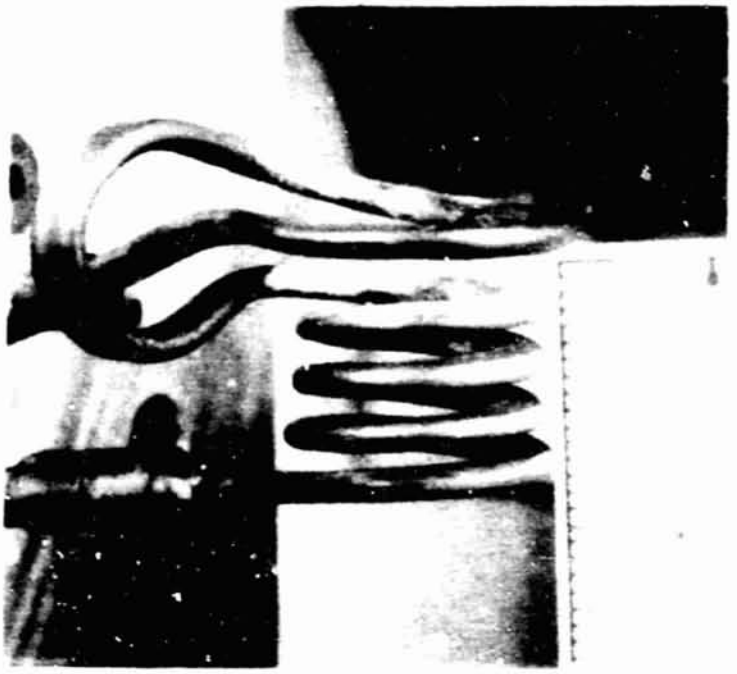

Fig. 2.a. Side view of coil, with inch scale. Note that the shape is nearly solenoidal, and that the top reverse turn is closely spaced.

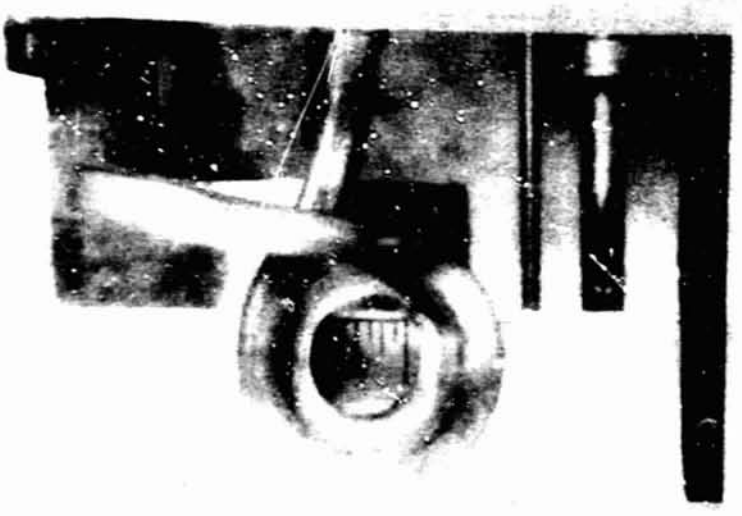

Fig. 2.b. Top view, showing throat diameter, and large upper reverse turn. Scale tic marks are 1/16th inch.

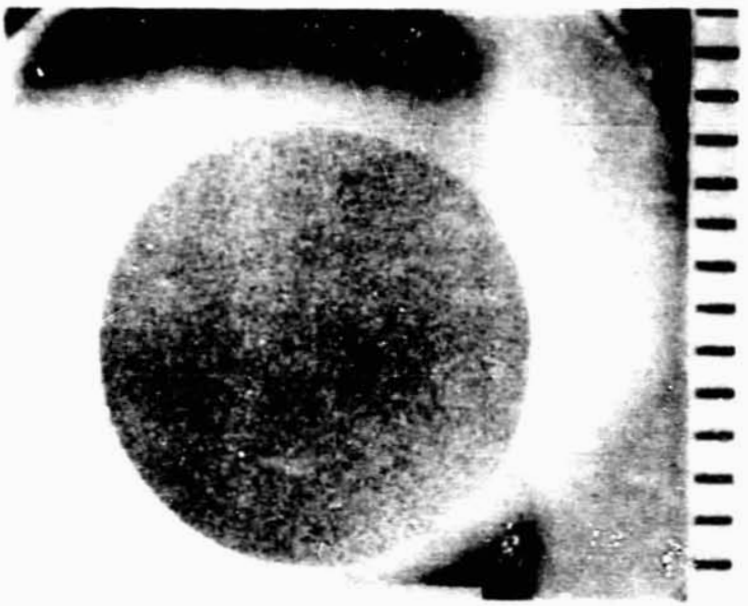

Fig. 3.a. Original grain structure of tungsten rod. Scale tic marks are millimeters.

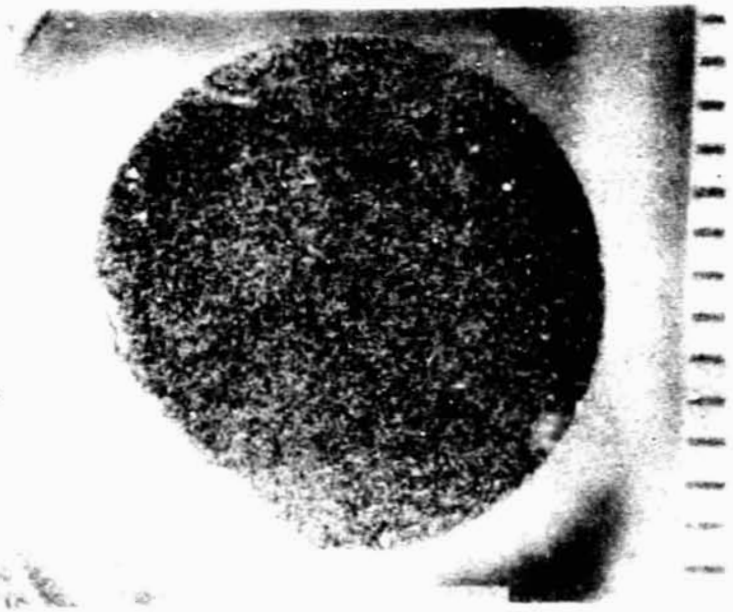

Fig. 3.b. Somewhat enlarged grain structure of large sphere after heating. Maximum temperature less than 3000 K. The flattened area at lower left is where this sphere melted into the aluminum vacuum wall on impact.

Fig. 4. Grain pattern for typical drop (run "A"). The electron beam impinged along the long axis of the sample from upper right. Note void, (tear drop shaped region). This sample is estimated to have been 75 percent molten at impact in the calorimeter. Scale tics are mm.

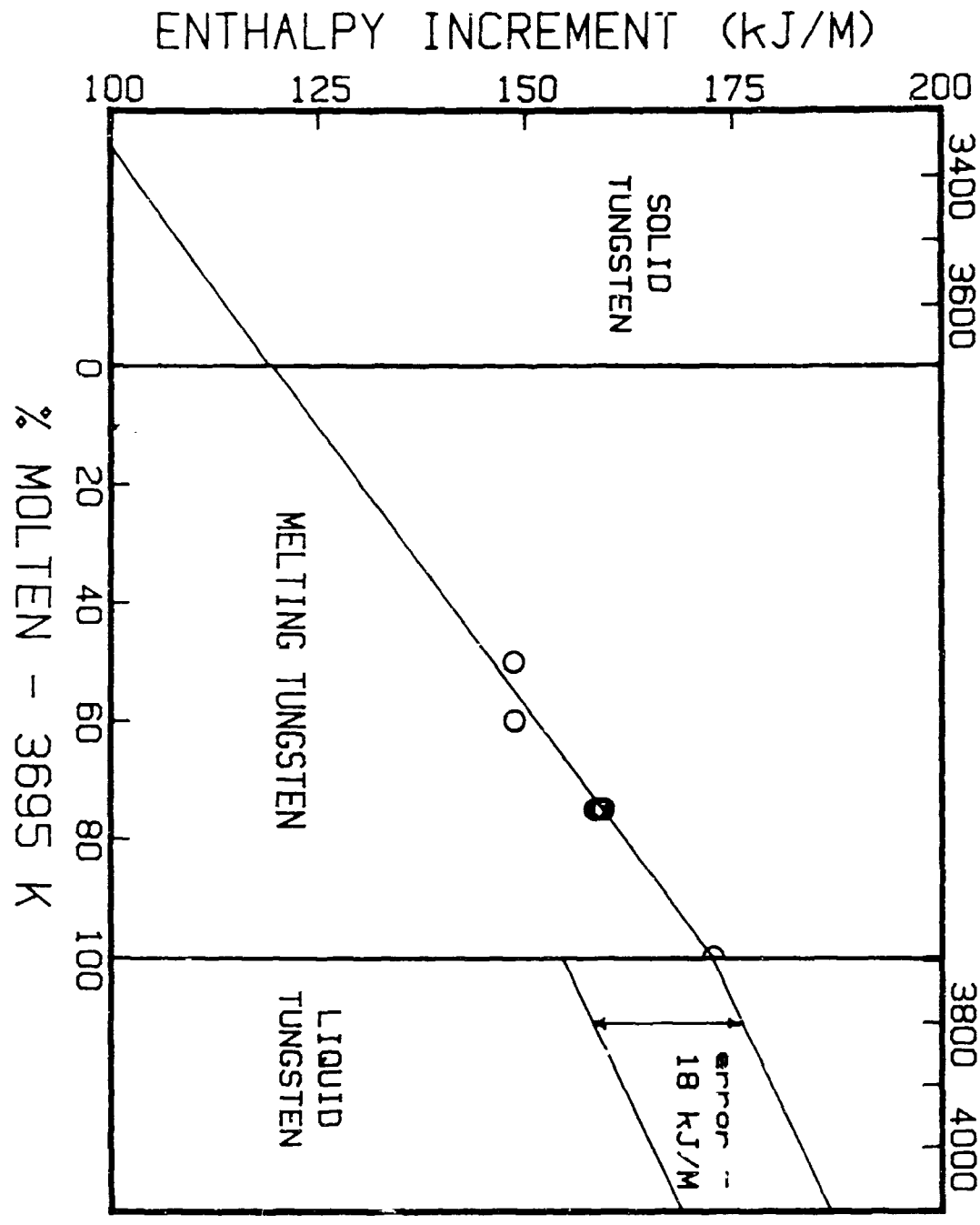

Fig. 5. Plot of fit to tungsten drops, showing the agreement with the JANAF [1972] selection. In the liquid regior, the JANAF curve has been raised 18 kJ from its estimated value. H(fus) determined here is 53.0 ± 2.3 kJ/mol.